Analysis of Droplet-target interactions in electrostatically charged spraying systems

---

A thesis submitted in partial fulfilment
of the requirements for the degree of

Master of Engineering, in
Electrical and Electronic Engineering

at the university of Canterbury

---

by E. J. McNearney, B.E. Hons

University of Canterbury,
Christchurch, New Zealand

December 2020.

Abstract

Increasing demands for food production and other agricultural products push demands for improved crop yields. Chemical pest management in the form of pesticides is a widely used method of increasing crop yields, over 90% of which is applied as liquid sprays. Poor application efficacy of these pesticides onto the target plant introduce concerns for both the environment and human health for those that come into contact.

Traditional spraying techniques result in up to 70% off target losses, with less than 1% of the active chemical reaching the target pest. These losses are highly configuration dependent needing to be selected for the target plant and environmental conditions. One method to improve spray efficacy, electrostatically charging the liquid spray, has been previously introduced to market. This thesis has investigated factors influencing the liquid spray deposition onto the target, looking into plant impedances and using computer vision to quantify depositions with the ESS electrostatic nozzle. A high voltage power supply has also been developed to allow control of nozzle voltage.

Leaf to ground impedances of potted grapevines were investigated as well as potential sources for the found values. It was found that the frequency and impedance relationship appears to follow dispersions found in other living tissues. It was also found that physical junctions in the plant where plant fibres intersect provided the largest impedance contributions with apparent linear regions in between.

A high voltage power supply was designed and fabricated, allowing for variable output voltage for use in testing of the ESS electrostatic nozzle, consisting of a boost converter and full-bridge converter.

Tests were designed using high speed imaging to capture droplet movements, and interactions with the target. Firsty a long distance microscope was tested, but ultimately proved to be insufficient for imaging droplets with the desired outcomes. The test configuration was then changed to use a laser diode as the light source, for used in diffractive imaging.

From there droplet path data was extracted from the captured images. Using kernels developed with Fresnel diffraction approximations for correlation to detect the centres of the diffractions caused by the droplets passing through the coherent light. A Kalman filter was implemented to estimate positions and the Hungarian method used to assign detections based on the estimate.

Analysis of the data showed that overall the interactions observed were as expected, showing increased attraction to the target when the spray is charged. Test 1 showed that at normal plant impedances for a single target, charge retention may is no issue. However, floating or larger impedance network as presented in a real plant, charge retention may present issues at longer spray periods. The results from test 2 indicate that while spraying at increasing voltages had the similar average accelerations, the behavior of the spray changed. At higher nozzle voltages, larger accelerations are seen, however occurring less consistently than at the lower nozzle voltages. This could be due to space charge and mutual repulsion effects causing droplets of higher charge-to-mass ratio to be dispersed before reaching the target. This is suggestive of an upper voltage limit before spray deposition efficacy decreases. Test 3 shows that Coulombic forces are greater than gravity forces for charged droplets, and an inverse relationship between nozzle distance from target and magnitude of attractive forces.

The research covered in this project highlighted areas where continuing research can be conducted. Plant tissue impedance could be further characterised to investigate the similarities seen with other living tissues. This would require a broader frequency range with higher resolution between frequency steps. In addition, the impedance network within a living plant could be investigated for possible charge retention issues for a more complex network as would be found in a larger plant.

An h-bridge was constructed to allow for bipolar switching of the voltage supplied to the nozzle, but this was never implemented in this project. Space charge within the spray cloud has been identified as a potential restricting factor deposition efficiacy, with bipolar charging presenting a potential solution. Measurement of current paths out of the plant would allow for verification of this, with increased current indicating improved deposition.

Also considered but never tested is the application of charged deflection plates to alter the shape of the spray cone independently of the nozzle geometry. This may provide some benefit in deposition when used in conjunction with charged sprays to better optimise the spray cone for a given target plant and spray environment.

The lack of depth perception in the test configuration used is a factor limiting the analysis of droplet interactions. Droplets could be moving in the depth direction without any indication. However as noted in Chapter 5 correlation strength was dependent on the depth of the simulated kernel potentially allowing for depth information reconstuction.

The motion model implemented in this project was simple and improvement on what was implemented here would allow for improved particle tracking with applications in other fields. Statistical analysis considering droplet size distribution, spary cone charge distribution and turbulence characterization would allow for much more complete analysis of the data gathered.

Acknowledgements

First and foremost, I would like to thank my supervisor Paul Gaynor. His guidance in undertaking the project has been immense, providing a lot of help understanding concepts that I initially considered quite abstract. Also his efforts in reviewing my thesis at the last minutes before submission need to be recognised. Without his help this project would not have been completed.

Additionally, I would like to thank my secondary supervisor, Scott Post for his knowledge and contribution to the project. Mark Jermy for his work designing the modular test platform and helping me with access the high-speed camera and Infinity Model K2 long-range microscope. Edsel Villa, for his insight and oversight when I was designing the high voltage dc-dc converter, and all around jolly demeanour. Byron Engler for his help finding the diffraction imaging solution to the lens problem. Also for pointing me in the right direction when I did not understand the optical phenomena I was seeing. Ben Mitchell for his guidance with programming in python. A great many hours were saved by his knowledge of python and the many available libraries

I would also like to acknowledge the funding provided by SfTI MBIE to initiate this project. Without that funding, I would not have undertaken this project.

Table of Contents

List of Figures

List of Tables

Introduction

As demands for production of food and other agricultural products increase, the demand for improved yields has also increased. Pest management is an integral part of yield optimisation, pesticides being one such way of chemically managing pests [1].

More than 90% the pesticides are applied as liquid sprays [2]. Sprays provide more accurate metering and on-site particle size control but are highly drift prone. Spraying is mostly performed by using hydraulic and conventional spray nozzle systems, pedestal-mounted sprayers, high pressure spray guns, hand pressure swirl nozzles, and consecutive high volume sprayers [2]. Current spraying methodologies call for spraying to "point of runoff" for best deposition onto the target plant [3], using large volumes of carrier fluid to achieve. Considerable inefficiency exists in depositing pesticides onto target-plant surfaces, often resulting in up to 70% off-target losses [4-6] and at times less than 1% of the of the active chemical reaching the target pest [7]. Spray deposition and hence losses, are highly dependent on optimal sprayer configuration for the given target crop and environmental conditions [8].

These off target losses present themselves as spray drift, surface runoff, and field drainage in the short and medium term, and through groundwater runoff in the longer term [9]. Through these means, in some situations significant levels of pesticides can be found in surface waters [10], a significant risk to the equilibrium of these ecosystems [11-13]. Non-agricultural use of pesticides has resulted in urban wastewater treatment plants becoming a significant route of pesticide contamination into the environment [14] as well as an additional pathway into water [15] for human consumption. Human exposure to pesticides is known to have significant negative effects in both acute [16, 17] and chronic [18, 19] cases.

In addressing the risks associated with pesticide spraying, there is great incentive to improve the application techniques: Providing solutions that increase deposition onto the target plant and reduce environmental losses. Current methods of reducing environmental impacts focus on reducing the susceptibility of the surrounding environments to runoff events via reducing potential pathways [20].

Another solution and the focus of this thesis, targets the reduction of mass with the applications of electrostatics to spraying. By charging spray particles, Coulombic forces are introduced, causing attraction between spray droplet and target, and aiding in overcoming forces present in the spraying environment. Previous studies have shown that electrostatic spraying can result in deposition improvements between 1.8 to 7 fold [7, 21] in idealistic scenarios, dependent on the morphology of the target, with some incidences using 40 times less water [7].

The aim of this project is to identify and investigate factors effecting the deposition of electrostatically charged sprays onto a target. This thesis describes the investigation into how electrostatically charged spraying can improve the outcomes of pesticide application, specifically with the ESS air-atomising induction-charging nozzle, and characterisation of its charge spray properties. Furthermore, additional research topics covered include measurement of plant impedance and the utilisation of computer vision to analyse videos captured with high-speed imaging.

Chapter 2 covers background knowledge for the reader to understand the applied concepts. Existing spraying technologies, voltage level converters, laser diodes, and image processing are covered in the depth relevant to this project.

Chapter 3 investigates the leaf to ground imedance path of a grapevine .Charge retention was considered as a factor affecting the deposition rates of charged sprays to the target plant so measurements were taken for the overall leaf to ground path for reference in later testing. Additionally the sources of impendances within the leaf to ground path were investigated as an initial look into the impedance network presented by the plant.

Chapter 4 discusses the design and fabrication of a variable output high voltage dc-dc converter for electrostatic spray charging.

Chapter 5 discusses the method of high speed imaging to capture the motion of droplets as a means of measuring droplet interactions with the target. Firstly a long-distance microscope was used then diffractive imaging with a laser light source.

Chapter 6 covers the extraction of droplet paths from the captured images. Computer vision and path prediction are used to ensure correct assignment of detected positions to the droplet path they belong to.

Chapter 7 then covers analysis and results of the droplet path data, finding trends in the droplet-target interactions.

Background

1 Current Spraying Technologies

Spray liquids makes up over 90% of pesticide application [2]. As would be expected, spraying technology exists to cover a wide range of use cases, both in electrostatically charged, and more traditionally uncharged application methods. These are described in detail below.

1.1 Traditional Agricultural Spraying

An aerosol spray is a collection of atomised (or aerosolised) droplets of liquid moving through the air. Aerosolisation of a liquid requires the application of an external force to overcome the surface tension of the liquid and subsequent breaking up into droplets. Traditionally, in an agricultural setting, the external force is applied with centripetal force, hydraulic-based force, or pneumatic force [22]. Spinning disc sprayers contain a nozzle that spin at high-speed and breaks up the liquid into uniformly sized droplets using centripetal force. Droplet size can be adjusted with variation of disc rotation speed with typically a narrow range of droplet sizes [22]. The working principal of such an atomiser is shown in Figure 1 [23].

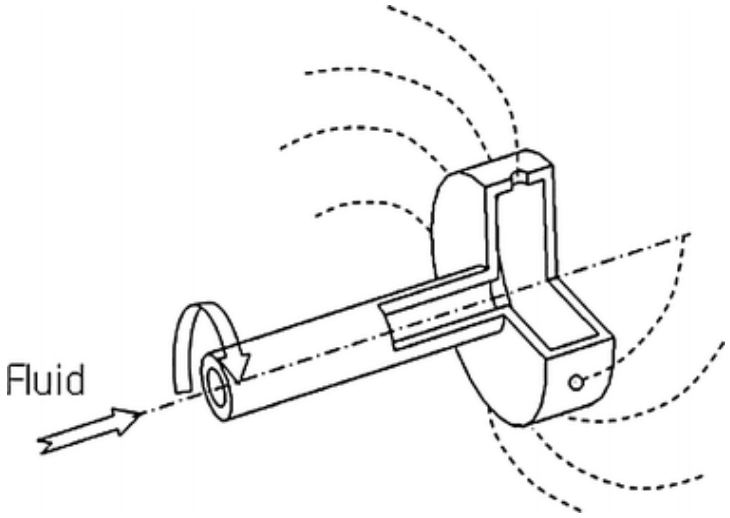

Figure 1: Operational principal of a spinning disk atomizer.

Single fluid hydraulic pressure systems force liquid through an orifice breaking the spray into small droplets. The nozzle design dictates the spatial and size distribution of droplets. Nozzle geometry selection and hydraulic pressure are the only controllable variables to influence droplet size and spatial distribution. A representative cross-sectional diagram is shown in Figure 2 [24].

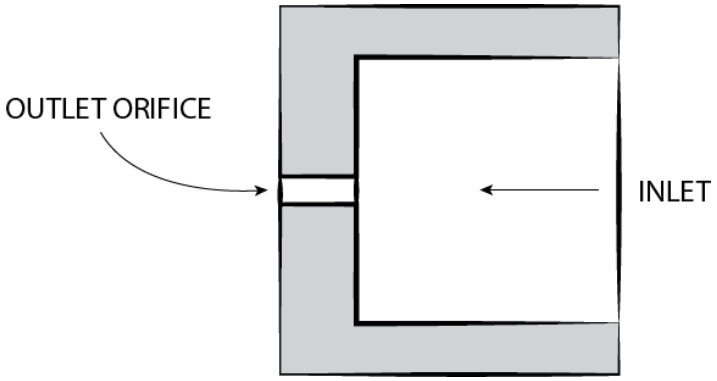

Figure 2: Single fluid type nozzle.

Pneumatic aerosolisers come in two differing designs; twin-fluid nozzles shear the liquid by impinging with a high velocity air stream, or air blast aerosolisers, which use high velocity and high volume air usually supplied by a large fan to aerosolise the liquid after leaving the nozzle. Both liquid flow rate and air pressure/flow rate will alter droplet size for a given nozzle geometry. A representative cross-sectional diagram showing both internallying missing and externally mixing nozzles are shown in Figure 3 [25].

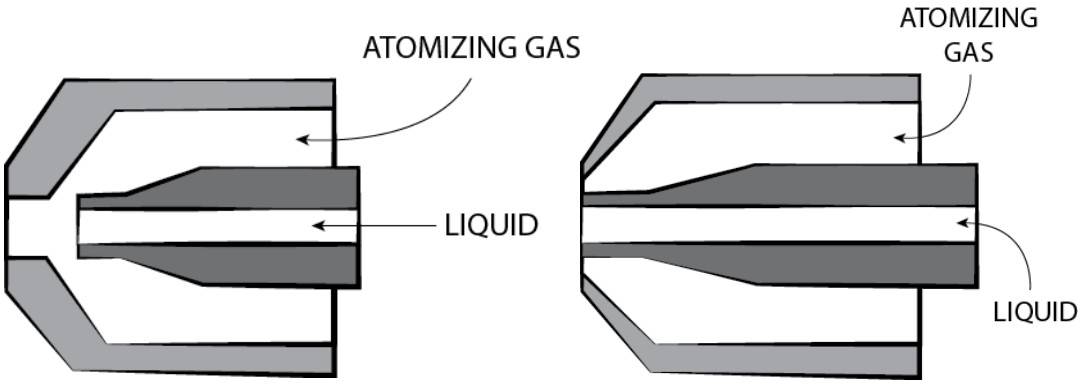

Figure 3: Twin fluid type nozzles. Internal mixing type nozzle on the left and external mixing type on the right.

These methods have an obvious drawback in that the motive energy of the droplets is a product of liquid flow and aerosolising force. In the case of spinning disc and hydraulic aerosolisers, droplet kinetic energy is the only motive factor, which favour larger diameter droplets [26]. Pneumatic aerosolisers have an extra control variable allowing for slightly more control. This has implications on the droplet penetration into foliage and tendency to drift. Recognising these drawbacks, air assisted spraying has seen use as a means to improve droplet distribution [27] and deposition [28, 29] in applications that require additional spray distribution control. This air assistance is provided as a high velocity air curtain[29] or sleeve[30] to direct the droplets. The latter can have impacts on spray drift while seeing better foliage penetration.

Spray deposition onto the target plant is highly variable and strongly influenced by a number of dependent factors. The sprayer configuration should be optimal for a given spraying situation [8]. Contributing factors include the geometry and density of the target plant [31-35], as well as environmental factors such as relative humidity, temperature, and wind speed and direction [36, 37] which are liable to be substantially variable. The configuration of the sprayer system, such as nozzle selection, boom height, and properties of the spray liquid also interact with the other spraying factors [31, 38, 39].

1.2 Electrostatically Charged Spraying

A method to reduce losses from pesticide spraying is the use of electrostatically charged spraying systems. Electrostatics, the study of charges at rest, explains the forces exerted between particles with a charge. This force, described by Coulombs Law[40], is given as:

$$F = k_e \frac{Q_1 Q_2}{d^2} \tag{1}$$

Where Q_1 and Q_2 are the magnitudes of charges (coulombs), k_e is the Coulomb constant, and d is the distance between charges (m). The force between two point-charges due to electrostatics is proportional to the product of the magnitude of those charges and inversely proportional to the square of distance between them. The force is attractive or repulsive depending on the charges being either opposite or the same polarity respectively.

This charge-distance relationship can be used in the spraying process to create an attractive force between a charged spray and earthed target, mitigating the effects of external influences such as forces from wind and gravity.

Deposition rates on plants can be improved by up to 1.8 to 7 fold [21] in idealistic scenarios, dependent on the morphology of the target. Electrostatic charge on the spray droplets can also increase adhesive forces[41]. One of the key driving factors of this improved deposition with electrostatic spraying is the ability for droplets to 'wrap around' the target. With sufficient charge on the droplet, the droplet can overcome aerodynamic drag[42], gravity[43] and the kinetic energy of the droplet [44, 45]. The result of this is that droplets can impact the target on the underside of the target, travelling upward from the ground, or on the side opposite from the spray source, 'wrapping around'. This benefit further improves spraying outcomes, coating an area of the plant which would otherwise be untreated.

To achieve these desired outcomes, a high charged to mass ratio is desirable to increase the ability of the droplet to overcome external forces. Charges starting at several mC/kg have shown to be beneficial, increasing deposition by two-fold and upwards [42].

2.1.2.1 Rayleigh Limit

The maximum charge that can be imparted onto a spray droplet is defined by the Rayleigh limit [46]. In a droplet, liquid surface tension is responsible for the spherical shape. When charge is accumulated in the droplet, internal Coulombic repulsion force occurs, opposing the surface tension force holding the droplet together. Given this, there is a critical value of charge for any droplet where Coulombic repulsion overcomes the surface tension holding the droplet together, causing droplet fission (the spontaneous separation of a droplet) [47].This value of charge within a given droplet is called the Rayleigh limit. This limit describes the maximum charge value a given droplet can hold. In mathematical terms for a given droplet, this is [48]:

$$q_{max} = \frac{\sqrt{2} \times 12\sqrt{\varepsilon_O \sigma}}{\rho d^{3/2}} \tag{2}$$

Where ε_O is the permittivity of free space, and σ is the surface tension (N/m), ρ is the density of the spray liquid (kg/m^3), d is the diameter of the droplet (m). Equation (2) shows the maximum charge increases as droplet diameter decreases.

2.1.2.2 Spray Charging

Three common methods exist for the charging of sprays: induction, conduction and ionised field charging. Each of these methods are very different in theory and have their own benefits and drawbacks.

Induction charging

Electrostatic induction causes a redistribution of electric charge within an object. A neutrally charged object contains equal amounts of positive and negative charge closely and evenly distributed. In a conductor, such as the sphere illustrated in Figure 4, these charges are free to move. Charge carriers are dependent on the material. In an electrolytic solution such as a spray liquid with dissolved compounds, charge is carried by free ions, in comparison to metals where free electrons carry charge [49]. The net result is the same resulting in a charged object, irrespective of the charge carrier. When this neutral conducting sphere is brought within the influence of a charged object (the rod), the sphere will have a positive charge induced on one side and a negative charge induced on the other. The charge will distribute such that the side nearest the charged object (rod in this case) will have the opposite charge to the object. This separation of internal charges is a result of Coulomb's Law. Grounding the sphere, while inducing a charge via the rod, allows the positive charge carriers to leave the sphere. If the sphere is then ungrounded whilst the induced charge is held, the sphere will then have a net negative charge. The rod can be removed and the charge remains [50].

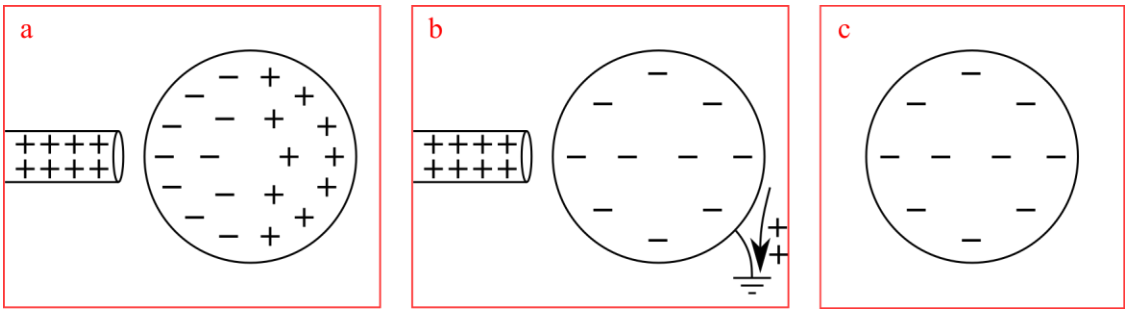

Figure 4: Illustration of induction charging. ***(a)*** *A conducting neutrally charged sphere is brought close to positively charged rod.* ***(b)*** *Sphere, under influence of charged rod, is earthed and positive charges allowed to escape.* ***(c)*** *Earth removed from sphere before rod and sphere remains negatively charged.*

In a liquid spray situation, utilising an electrode in the nozzle and earthing the body of the liquid can generate the type of charge redistribution mentioned. As the liquid passes the nozzle electrode, a charge distribution is introduced. The liquid is then aerosolised into spray and separated from the earth connection, remaining charged. This does require an adequately conductive liquid, to ensure that charge redistribution can occur as the liquid passes the electrode and is aerosolised as it leaves the nozzle.

The amount of charge that can be imparted on a droplet depends on the charge time constant τ of the droplet and the time for droplet formation t_f (s) to occur in the nozzle. In terms of the liquid resistivity ρ (Ωm) and dielectric constant *K* (Farad/m) [51]:

$$\tau = K\rho\varepsilon_0 \tag{3}$$

Law et al. [51] identified the constraint $\tau < t_f/5$. With water based sprays ($K \sim 80$) fluids must have resistivity $\rho < 4.5 \times 10^5 \Omega \cdot m$ for predicted compatibility. As long as operating within the operational limits of a given nozzle geometry and liquid flow rate, the droplet charge typically increases linearly with the voltage on the induction electrode [52]. Given that the charge induced on the spray is opposite to the electrode, the spray leaving the nozzle will be attracted to the electrode. However, use of an air shear nozzle helps deflect droplets away from the nozzle [52].

Conduction Charging

This method requires that a conductive liquid be in direct contact with a high voltage electrode (relative to earth potential), bringing the body of liquid to the same potential. Again a conductive liquid is required but not to the same degree as with induction charging. Conduction charging has previously been achieved in two manners:

The 'Electrodyn[53]' nozzle utilises a purely electrostatic approach. The body of liquid is in contact with and pushed past a high potential metal electrode. Electrically generated mechanical forces are used to generate droplets, which shear from the body of the liquid as the charge exceeds the Rayleigh limit and spontaneous fission occurs from induced electrostatic forces. Liquid flow rate and voltage dictate the droplet size. Droplet size decreases with a higher electrode voltage or decreased flow rate. The viscosity and conductivity will also adversely affect the droplet mass and charge.

The other method of conductive charge transfer utilises a conventional hydraulic or air-shear nozzle. The charged high voltage electrode is placed directly in the spray path. In the case of Marchant and Green [54], the nozzle is held at high voltages of up to 10kV with a nearby field-intensifying earth electrode. This has obvious downsides in that much more of the equipment and liquid is held at this high potential.

Ionised Field Charging

When an electric field exists of greater strength than the dielectric strength of a nuetral fluid, usually air, the fluid will start to ionise, resulting in plasma formation. The plasma conducts charge to regions of lower potential within the air. This is how corona discharge occurs around a conductor that has a concentrated high electric field strength and gradient. A finer point electrode lowers the required voltage [55] for corona onset as the finer point presents a higher field gradient. Within this corona discharge, ions of the same charge as the electrode are repelled and ions of the opposite charge attracted. Particles passing through this field will capture and carry away a portion of these ions, gaining a net charge. Liquids of a wide range of conductivies can be charged with this process [56]. The level of charge imparted on the spray is dependent upon the dieletric constant of the spray particle, its surface area, the electric characterisitcs of the corona discharge and the time within the ionised fluid [57]. Consideration for the protection of the charging electrode must be taken as these are usually fragile and needle-like.

2.1.2.3 Space Charge Effect

While charging droplets causes attraction to the target as described by Coulombs law (equation 1), the droplets are also influenced by the charges of the droplets around them. This charge within a spray cloud has been shown to negatively affect spray efficacy [51, 58]. The droplets, being of the same charge, will undergo mutual repulsion, becoming a more dominant force as droplet velocities decrease[41]. This repulsion can lead to dispersion of the spray cloud and generate drift. Drift is dependent on whether the droplets dispersing from the spray cloud are deposited onto the target before being allowed to escape [42].

It was also found this space charge effect increased the electric field around leaf tip, which with high levels of charge can result in corona forming around the sharp points on the leaf tip, limiting deposition onto the target plant [59]. Bipolar charging was tested in this study, but was found to offer no improvement in deposition over unipolar charging.

Specifically with induction charging the ‘space charge suppression’ effect poses a limitation on spray charge. Law et al. [51] found that for their embedded electrode, induction-charging nozzle, the spray cloud current linearly decreased by 41% between the nozzle plane and a 50cm axial distance from the nozzle. This was attributed to the reduction of field strength at the nozzle from the space charge of the droplets. Zhao et al. [58] showed that while nozzle current stayed the same, ‘leakage current’ due to the losses associated with charged droplets impacting the nozzle dielectric reduced charge transfer efficiency to the target. Both found that reducing the distance from nozzle to earth target improved efficacy of the charged spraying. While not found in literature, it is possible that bipolar voltages will reduce the effects of space charge suppression, however higher frequency voltage polarity transitions pose the risk of introducing mutual attraction of spray droplets at the time of voltage transition.

2.1.2.4 Commercial Development of Electrostatic Sprayers

A number of electrostatic spraying systems are, or have been, commercially available. The “Electrodyn” sprayer saw use in Africa [60] and South America [61] within commercial cotton farms but issues with foliage penetration limited by the charging at aerosolisation method saw it fall out of use.

Currently, electrostatic sprayers are available through four main suppliers:

- Martignani Electrostatic Sprayer [62]
- Spectrum Electrostatic Sprayers [63]
- Electrostatic Spraying Systems (ESS) [64]
- On Target Spray Systems [65]

These all promise improved spray deposition and reduced drift without specific supporting research with the exception of ESS. This system is based on Edward Law’s extensive research [52, 66], utilising a twin-fluid, embedded electrode, induction charging nozzle. For these reasons, the ESS BP1 sprayer nozzle was the nozzle used

for research described in this document. Diagrams illustrating the components and cross section of the nozzle are shown in Figure 5 [64] and Figure 6 [67].

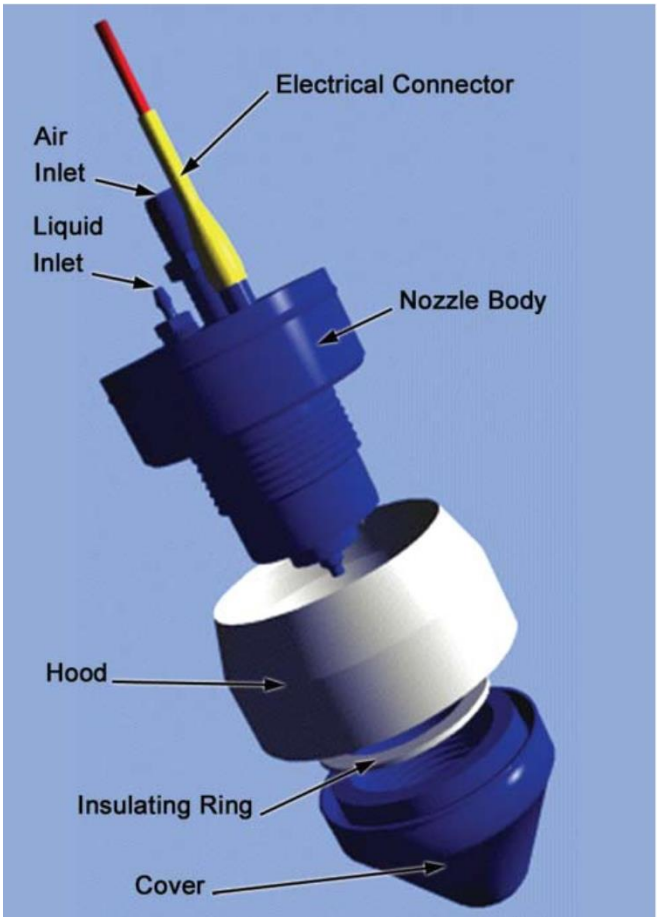

Figure 5: ESS nozzle component diagram.

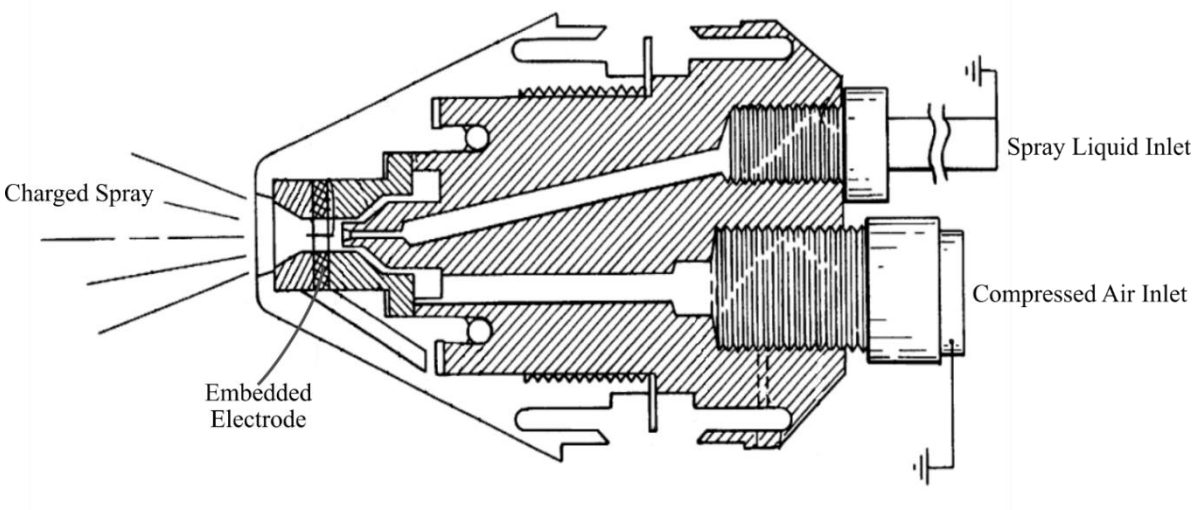

Figure 6: Cross section of ESS Electrostatic Spray Nozzle. This design utilizes internal mixing, with an embedded induction-charging electrode.

2 Voltage level power converters

Imparting a charge onto the spray droplets and seeing the benefits of electrostatic spraying requires bringing the charge electrode up to a large electric potential. Charging the droplets requires the use of a power converter to step up low voltages to a high dc voltage in the range of kilovolts [42]. For testing, preferably with adjustable output voltage.

Though the voltage requirements are high, the required currents for electrostatic charging are very low, giving a low power input requirement. No off-the-shelf solution was found within the range of required voltages, with safe low power outputs. The low power requirements makes it practical to have the low voltage source in the form of a small battery pack (low voltage dc). Having a high voltage requirement does introduce additional PCB layout and safety constraints to the design.

A common and efficient method of changing voltage levels is to us a switch mode converter. Switch mode power supplies (SMPS) are a class of converters characterised by semiconductor switches operating at high frequencies and energy storage devices such as inductors and capacitors. SMPS topologies exist that allow for a voltage step down or step up. In this electrostatics application case, the voltage needs increasing. A few of the suitable topologies are discussed below.

2.1 Boost Converter

A boost converter is a simple non-isolated SMPS step up dc-dc converter. Operation relies on the property of inductors to store and release energy in a magnetic field to resist changes in current flow, given by the equation [49]:

$$v = L\frac{di}{dt} + i_0 \tag{4}$$

Where v is voltage, i is current, i_0 is inductor minimum current, L is inductance, and t is time.

As long as the ripple current in the inductor stays above zero, the converter can be said to run in continuous mode. If the current is allowed to drop to zero, then the converter is operating in discontinuous mode. The description here will focus on continuous mode operation, as this is what is used throughout this project.

In steady state operation, average current through the inductor must be zero. As the voltage across the inductor is proportional to current, as shown in equation 4, average voltage across the inductor must also be zero. Energy is stored in the inductor as a magnetic field when current flows into it, and released as the current through it drops. This occurs during two distinct states, shown below in Figure 7.

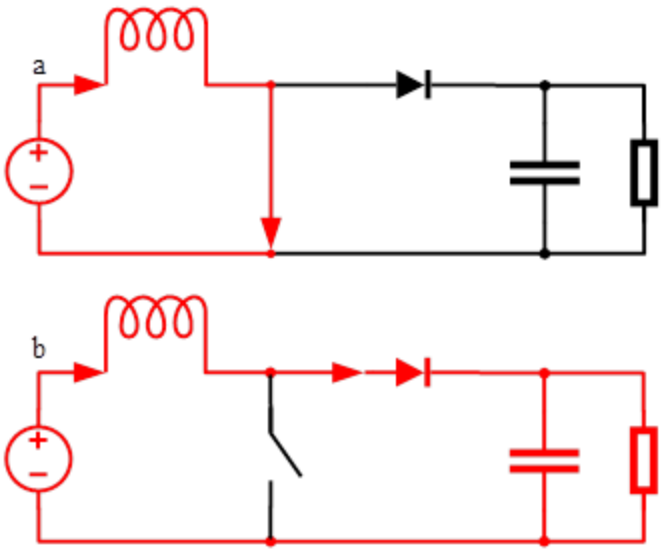

Figure 7: Two states of a boost converter with current paths highlighted in red. (a) On: switch closed and inductor energising (b) Off: switch open and inductor magnetic field collapsing.

Depending on the state of the switch, the current follows one of two paths. Derived by the following equations [68]. During the on stage (Figure 7a) of the boost converter, the inductor is isolated from the output, and supplied a constant voltage, generating a linearly increasing current and hence increasing magnetic field. From equation(4, given by:

$$\frac{\Delta I_L}{\Delta T} = \frac{V_i}{L} \text{ or } \Delta I_L = \frac{V_L}{L} \times \Delta T \tag{5}$$

Where I_L is inductor current, T is switch time, V_i is input voltage, L is inductance. The inductor current increase during the time the switch is closed is proportional to the voltage the voltage across the inductor:

$$\Delta I_L(+) = \frac{V_i - (V_{DS} + I_L \times R_L)}{L} \times T_{on} \tag{6}$$

Where V_{DS} is voltage drop across the MOSFET (switch), $I_L \times R_L$ are inductor current and resistance representing voltage drop across the inductor due to dc resistance. When the switch is opened (Figure 7b), the output is connected to both the voltage source and inductor in series. The magnetic field inside the inductor starts to collapse, pushing current into the output. The inductor current will drop as energy is released from it. This decrease in inductor current is given by:

$$\Delta I_L(-) = \frac{(V_o + V_d + I_L \times R_L) - V_i}{L} \times T_{off} \tag{7}$$

Where V_o is output voltage, and V_d is flyback diode forward drop voltage. Equating equation 6 and 7 gives:

$$V_o = \frac{V_i - I_L \times R_L}{1 - D} - V_D - V_{DS} \times \frac{D}{1 - D} \tag{8}$$

Using $D = T_{on}/T_S$ and $(1 - D) = T_{off}/T_S$. This is often simplified with the assumption that R_L, V_D and V_{DS} are small enough to be ignored, giving by the equation [69].

$$\frac{V_o}{V_{in}} = \frac{1}{1 - D} = \frac{I_{in}}{I_o} \tag{9}$$

2.2 Full-Bridge Converter

A full-bridge converter is a very simple switch mode converter in terms of operation, consisting of a full-bridge (often called an h-bridge) for switching dc to ac, and a transformer to step the voltage. The ratio of primary to secondary windings describes the step up or step down conversion ratio of the transformer. A simplified schematic diagram of this topology is shown below in Figure 8.

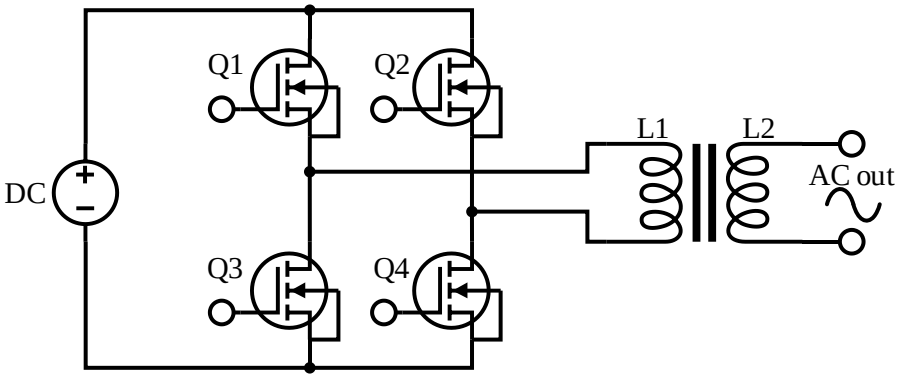

Figure 8: Full-bridge converter

For applications that require a dc output voltage a rectification stage may be added to the output of the transformer, as well as capacitors for output ripple smoothing.

2.3 Voltage Multiplier

While a voltage multiplier is not a dc-dc converter or SMPS circuit, it can be added to an ac output power source to create multiple cascaded voltage steps where low currents are required. A voltage multiplier is an uncontrolled diode rectifier circuit, acting on an ac input and providing a dc output.

The Villard circuit [70], is a simple diode clamp circuit, offsetting the ac voltage with a dc bias such that $V_{OUT} = V_{IN} + V_{INpeak}$ [71] and the voltage no longer passes through zero. Its ripple however is large going from zero to V_{OUT} every cycle.

The Greinacher circuit [72] (or half wave voltage doubler – shown in Figure 3) improves on the Villard circuit by adding a peak detector circuit to the output of Villard's diode clamp. The peak detector smooths the ripple while preserving the voltage peaks of the diode clamp.

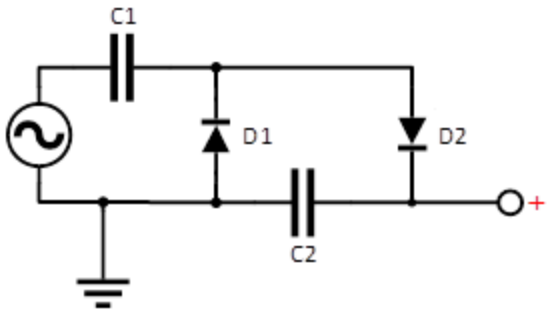

Figure 9: Greinacher circuit or half wave voltage doubler.

A Delon [73] circuit (or full-wave voltage doubler – shown in Figure 4) uses two half-wave peak detectors with outputs in series to double the input voltage. The bridge topology of this circuit forward biases one diode on each wave-half of the ac signal. When D1 is conducting C1 is charging, when D2 is conducting D2 is charging. Because of the capacitors are in series, the output capacitance is half of each half wave input capacitance but at double the voltage.

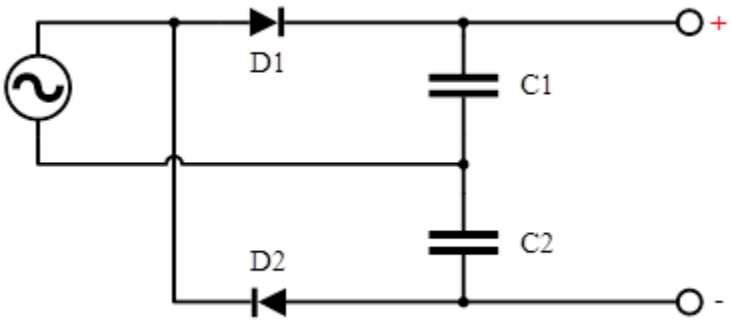

Figure 10. Delon circuit or full wave voltage doubler.

Current output from these circuits is limited by the capacitance required for the desired smoothing as well as heat caused by diode conduction losses. If greater efficiency is required, there are topologies that multiply the voltage with active switching.

In addition to the numerous dc-dc converter topologies, it is possible to cascade any number of voltage level converters to meet necessary output requirements. Stability and controllability does become a consideration when cascading active circuits.

In the application of electrostatics in spraying with induction charging, current transfer into the spray cloud typically fall below 10 µA [21, 74]. Any addition current requirements will come from circuitry to monitor output voltages. With this in mind, the topologies implemented in this project do not require high output current or efficiency.

3 Laser Diodes

Laser (light amplification by stimulated emission of radiation[75]) diodes are a semiconductor device that use electrical pumping to generate lasing conditions. A forward-biased voltage applied across the diode causes the movement of charge carriers (in semiconductors holes and electrons), which when combining, generate spontaneous emission of a photon. Electrons and holes can exist in close proximity to one another briefly until a nearby photon with the same energy as the recombination energy causes recombination by stimulated emission [76]. This stimulated emission is the hallmark of a laser, the creation of a lasing condition, separating laser sources from conventional sources that generate light via spontaneous emission. Generating a photon by stimulated emission, results in the photon having the same frequency, phase and polarisation as the first photon. The result being that the emitted photons are of very narrow wavelength band (temporally coherent) and are of the same phase (spatially coherent) [77]. A result of the extremely narrow wavelength band is when focussing laser light, the beam can be focussed with very little divergence.

When this spatially coherent wavefront reaches an imperfect non-flat surface, a speckle pattern is observed. This speckle pattern is a result of constructive and destructive interference with the planar wavefront and reflections from the imperfect surface. The reflections interfere with the wavefront in the space in front of the surface [78]. This granular effect is objective (called “objective” speckle) and the same pattern is visible from differing viewing angles and distances. When directly observing the laser within the beam (as with a camera), speckling also occurs. However this is due to a different cause, introduced by Airy [79] disc diffractions as a result of the lens aperture. These discs form on various scattering regions of the lens interfering and causing the “subjective” speckle.

Often, the output from a laser diode is not of uniform spatial intensity across the beam profile as is required for imaging[80]. Any dust in the system can also introduce additional noise in the form of diffraction patterns, leaving rings in the beam profile[81]. Spatial filters are designed to remove unwanted multiple-order energy peaks and pass only the central maximum of the diffraction pattern. A spatial filter consists of a microscope objective with a positioning system and a pinhole aperture. The pinhole is placed at the focal point of the microscope objective so that the converging beam passes through the pinhole. A representative image of this configuration is shown below in Figure 11 [80].

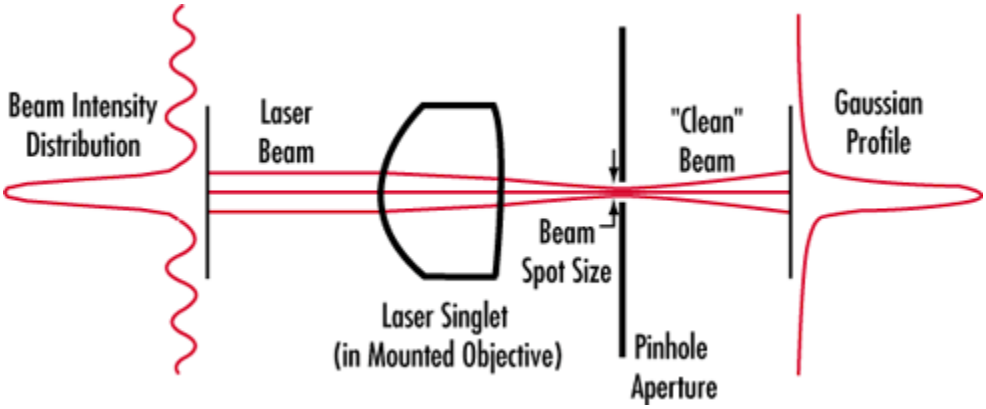

Figure 11: Representative configuration of a spatial filter with input on the left and output on the right.

4 Digital Image Processing for Tracking of Moving Particles

Most raw data needs to be processed in some way in order to extract the information in a format compatible with any specific analysis method. Data obtained in the format of images are not excluded from this requirement and as such must undergo some signal processing. Digital image processing utilises digital computation methods to manipulate images in order to extract useful information [82].

4.1 OpenCV

OpenCV is an open source computer vision and machine learning software library. This library provides the infrastructure for computer vision and image processing applications with more than 2,500 algorithms [83]. This software library is supported in C++, Python and MATLAB programming languages.

4.2 Computer Vision Methods

A digital image, represented as a matrix, can be considered as a two-dimensional function, $f(x, y)$ of a spatial system (x, y) in an image plane. The function describes the intensity of the image in space. Each x and y coordinate within this matrix is a discrete valued pixel. Manipulation of an image therefore becomes a mathematical problem, with mathematical solutions.

4.3 Background Subtraction

Separation of background and foreground is a widely used method in image processing when detecting time-variant objects in a sequence of images [84]. Background subtraction is a common approach to this problem when the images are taken from a static camera. The approach is to detect the moving objects as the difference between the current frame and a reference "background" frame. The background must represent the scene with no moving objects, it must be updated to reflect any changing conditions [84]. Processing many individual images such as with video, removal of background can be hugely beneficial in reducing the amount of information that has to be parsed.

4.4 Spatial Filtering

Extracting or emphasising certain features of an image can be a beneficial step in image processing. Often these features are in the relations between a pixel and pixels surrounding. Spatial filtering is a computational method of finding these relationships[85, 86]. Spatial filtering relies on convolution (related to mathematical convolution), combining a kernel (also called a mask) and input image to output a third image. Using different kernels, different effects can be achieved in the output image. Among the possible kernel functions are edge detection, sharpening, and blurring.

The mathematical operation of spatial filtering is a multiplication in the frequency space [87]. Computationally, the operation consists of multiply and shift operations. The kernel elements are multiplied with the elements of the input image and summed. The resulting value represents the value of the output image at the position of the kernel centre over the input image. The kernel is then shifted to centre over the adjacent pixel in the input image. In the case shown in Figure 12 [87], where the kernel centre of position of the input image is (4,4), the corresponding value of the output image *P* is equal to the summation of the multiples of the kernel values and the corresponding values they "mask".

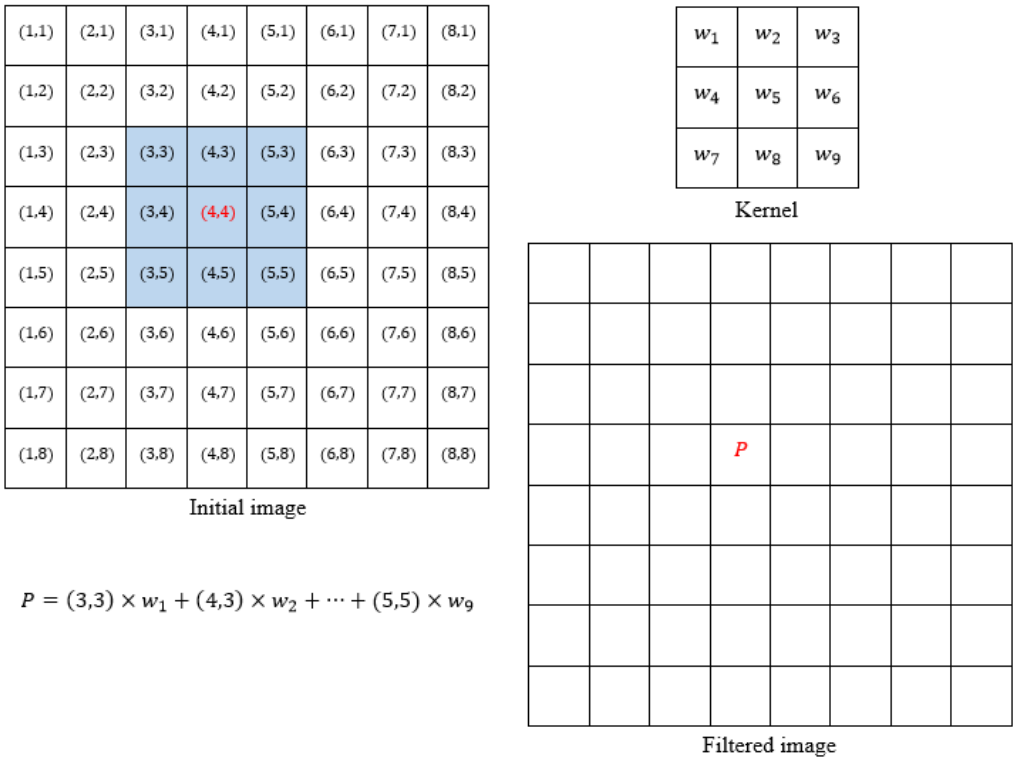

Figure 12: The value P of the convolution output of an image and kernel.

There is a limitation here in that the output image must then be smaller than the input matrix by the dimensions of the kernel less one. Also, of note, the kernel must be odd in both dimensions in order to have a centre position. In the case of Figure 12, the (1,1) position of the output image would have the kernel centre over the (2,2) position of the input image. One method of overcoming this is to zero pad the input image before the operation to centre the kernel over the (originally) (1,1) position of the input image, resulting in an equal size output image.

4.5 Gaussian Blur/Smoothing

Smoothing or blurring is often used in image processing to remove high frequency noise: It acts as a 2-dimensional low pass filter [88]. This is done by using a 2D convolution with a low pass filter kernel to average the signal over the kernel sized area. A Gaussian blur is an averaging kernel with a (normalised) Gaussian distribution of values. This is given by the equation [89]:

$$G_i = \alpha * e^{-(i-\frac{(n-1)2)^2}{2*\sigma^2})} \tag{10}$$

Where n is kernel size, $i = 0\ to\ n-1$ and α is the scaling factor such that $\sum_i G_i = 1$

The formula given is single dimensional but by taking the dot product with its transpose, a two dimensional kernel can be made. For a 3x3 kernel with a sigma of one, this yields:

$$\begin{bmatrix} 0.077847 & 0.123317 & 0.077847 \\ 0.123317 & 0.195346 & 0.123317 \\ 0.077847 & 0.123317 & 0.077847 \end{bmatrix}$$

A larger standard deviation results in a much stronger blur. These smoothing filters are best used in situations where the image has a low signal to noise ratio (SNR)[90] as filter response is dependent on the Gaussian distribution as opposed to the SNR of the source image. In cases with less noise, other filters could be more efficient [90].

4.6 Blob Detection

A 2D blob, under a number of definitions [91-94], is generally described a homogenous region that is distinguishable from its surrounding space as a local extrema. Detecting these regions (and their size, location, and count) is often an important task in computer vision. These blobs could represent points of interest in an image, such as tumours in an MRI [95], galaxies in a Hubble telescope image [96], or spray droplets moving through the air.

Blob detectors are a group of methods used to identify regions that differ from their surroundings. There are several methods that achieve this goal, all with their own set of advantages and disadvantages. These methods fall broadly into two categories, differential detectors based on derivative expressions, and local extrema in the intensity landscape called watershed detection [97].

Of the differential detectors commonly used, the Laplacian of Gaussian [98] is most common. This method convolves the input image with a Gaussian kernel. A Laplacian operator is applied to find the local maxima/minima representing the blobs. Another method, the difference of Gaussians [91], is similar in operation to the Laplacian of Gaussian method, with some minor changes to operations allowing for separate and different Gaussians to be used.

Watershed detection methods are generally simpler and have a lower computational demand. Described by Vincent and Soille [99] a greyscale image is considered like a topographical map containing bodies of water. Water catchment basins represent minima, and watersheds the maxima. Incrementally increasing the water level (thresholding) reveals the location of watersheds. These watersheds show the location of bright blobs. Dark blobs are found by taking the gradient of the image and applying the same raising water level method. This method has the tendency to over segment densely blobbed images.

The method used in OpenCV implements the watershed method, creating a series of thresholded binary images of the frame. Then a border following algorithm [100] is applied to the edges of distinct blobs. The watershed approach is convenient in the implementation of OpenCV as it allows for additional filtering such as with shape and size.

4.7 Kalman Filter

While not specifically a computer vision method, a Kalman filter [101] or linear quadratic estimator is a computationally efficient method for predicting the future value of a discrete variable. The filter consists of a set of mathematical equations implementing a predictor-corrector type estimator that minimises estimated error covariance [102].

To estimate the next value of a variable, the filter uses:

1. knowledge of the system and measurement device dynamics,
2. the statistical description of the system noises, measurement errors, and uncertainty in the dynamics models, and
3. any available information about initial conditions of the variables of interest.[103]

The filter consists of two discrete steps: predict, and update. With the predict step being Bayesian [104] and the update computational. The predict step projects the current state estimate ahead in time, with the probability of the *a priori* estimate conditioned on prior measurements [102]. The update step adjusts the projected estimate and estimate covariance based on the actual measurement. The advantage of Kalman filters over other methods is that

they are memory efficient as they do not need to store previous positional data and they are computationally efficient, taking only a few operations to estimate and update.

4.8 Hungarian (Munkres or Kuhn-Munkres) Algorithm

The Hungarian algorithm is again not a computer vision method but instead a method for solving the optimal assignment problem [105]. Given an assignment problem with *n* tasks and *n* possible candidates and a one to one assignment of these tasks to candidates, there are exactly *n*! possible combinations. Using brute force and calculating all possible combinations in order to find the optimal assignment would be unfeasible for any large size of *n*. The Hungarian method [106] (also known as Kuhn-Munkres algorithm or Munkres assignment algorithm) is a combinational optimisation algorithm: it will reduce a matrix of costs to find the optimal or least cost assignment.

For a *n* x *n* matrix of costs, the following steps are taken [107]:

1. Subtract row minima
2. Subtract column minima
3. Cover all zeros with a minimum number of lines.
4. Check if there are *n* number of lines present. If not continue onto five.
5. Take the smallest element not covered by lines, subtract from uncovered rows, and add to covered columns.

Meeting the criteria from step 4, shows the position of the optimal assignments. This is shown graphically in Figure 13 [107]. This algorithm is a solution to the optimal assignment problem that runs in polynomial time[108].

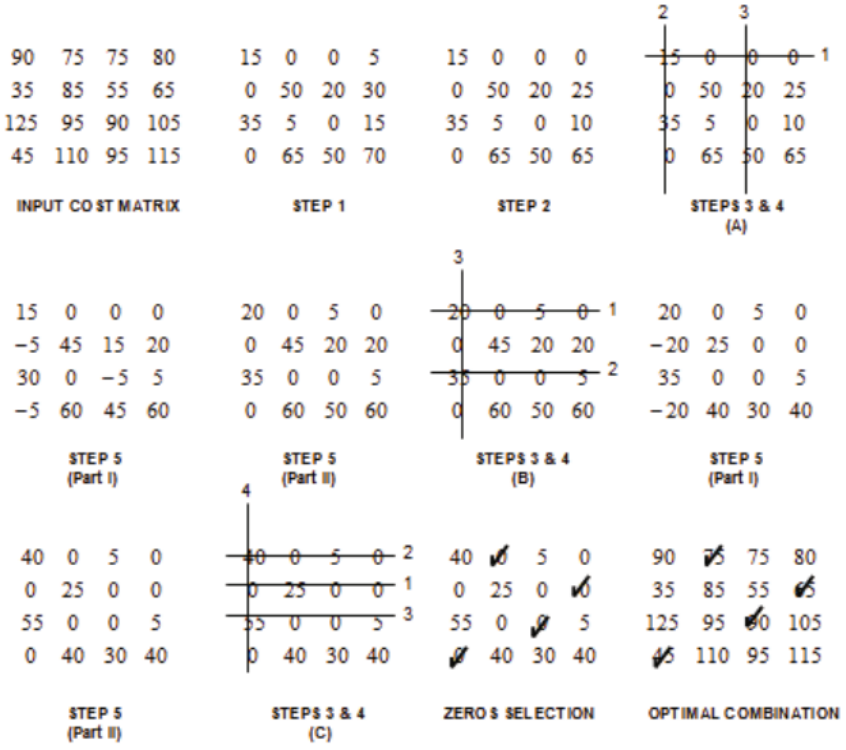

Figure 13: Hungarian method, step by step[107].

These tools provide the foundations for finding droplet positional data from the raw images captured by the high-speed camera. From identifying droplets from the raw images captured by the high-speed camera to as assigning individual paths for each of the droplets detected. From this positional droplet data, droplet movements and interactions with the target can be calculated and analysed.

Measurement of Grapevine Impedance

Plant electrical impedance was a specific area of concern in the application of electrostatics to horticultural spraying. Wood is a highly anisotropic material, with different properties across and along the grain. This holds true for impedance with higher conductivities in the axial direction compared to the radial [109, 110]. Conductivity in wood is also subject to fluctuations in temperature, with conductivity increasing near linearly with temperature [109]. Moisture content is another factor contributing to conductivity, with a linear relationship between conductivity and moisture content [111].

The impedance of the target plant could introduce issues with charge retention, altering droplet-target interactions. Primary interest is in overall resistance and capacitance at dc. However, due to capacitive effects, ac measurements must be taken to prevent capacitive charging impacting values. Lane and Law [112] noted that even under drought conditions beyond the point of recovery, no significant reduction in transient charge transfer was observed. However, plants in their testing measured at a maximum of 700kΩ, which is substantially lower than preliminary testing done here would indicate, with leaf to ground impedances taken measured well above that range.

The two following tests were conducted in conjunction with Scott Post of Lincoln Agritech, though all tests are of the authors design. These tests aimed to approximate the impedance of a target plant and provide information for later testing. Initially grapevines were set as the early-stage target plant for electrostatic spraying. As such they are used in this testing to this end.

3M Red Dot 2235 monitoring electrodes were used as leaf contacts for both tests. The sticky gel of these electrodes offered repeatable and consistent application to grapevine leaves. Impedance measurements for all test were taken with a Fluke/Philips PM6304 RCL meter with 1V peak to peak ac and no dc bias.

1 Impedance of potted grapevines

This test focusses on the electrical path for a leaf, which has gained charge from charged spray droplets, to discharge. Tests were conducted on potted grapevines, allowing for easier control of environment variables including water content of plant, and soil moisture. Grapevines were watered daily for a week prior to testing, keeping plant in a saturation condition. 30 minutes prior to any measurements, the pot was watered to saturation and left to drain.

Test 3.1 did include plants of two different ages. For 3.1a, plants were small, approximately three months old. For 3.1b, the plants were between one and two years old, being comparable to the size in an orchard.

Leaf contact was made with 3M Red Dot 2235, and soil contact with a 10mm diameter steel rod. The rod had a length of 200mm, with a sharpened tip, inserted 180mm into the soil. Multiple parallel rods were used as a measure to mitigate the earth rod being a source of impedance; however were found to be unnecessary. Wetting the soil prior to taking measurements minimised earth-rod impedance contribution such that multiple rods did not provide any observable benefit. The earth rod placement was as close to the trunk of the plant as possible. The measured grapevine was electrically isolated from nearby grapevines to prevent parallel paths.

Results

The results of this testing are shown below in Table 1. Small values of capacitance, increasing inversely with electrode distance suggests the values are majorly a result of contact capacitance.

Table 1: Impedance measurements for tests 3.1a and 3.1b. Noting reactance is inversely proportional to capacitance, these represent small values.

Test	Plant	Electrode Spacing (cm)	Frequency(Ω)			
			100	1,000	10,000	100,000
3.1a	1	81	2.1e6 - 4.2e7j	1.8e6 - 5.8e6j	1.1e6 - 1.1e6j	4.8e5 - 2.1e5j
	2	107	2.9e6 - 3.5e7j	2.4e6 - 6.1e6j	1.2e6 - 1.5e6j	5.8e5 - 3.2e5j
3.1b	1	112	1.7e6 - 2.8e7j	1.6e6 - 8.4e6j	1.0e6 - 2.2e6j	6.0e5 - 8.4e5j
	2	208	3.6e6 - 5.3e7j	2.9e6 - 9.1e6j	1.7e6 - 2.8e6j	1.1e6 - 5.7e5j

From this data, the time constant values at the low frequencies were below 0.05 s in the worst cases. However it is undetermined what part of the capacitance is from the contacts and which are internal to the plant. It is also unknown whether this will impact spray deposition as the charges invovled are small and the time a leaf is exposed to the charged spray is also minimal. Further testing would be required to determine deposition and charge transfer over time.

Looking at only the real component, knowing that this is solely from the plant, the plots in Figure 14 are generated, showing frequency versus resistance as well as electrode distance versus resistance.

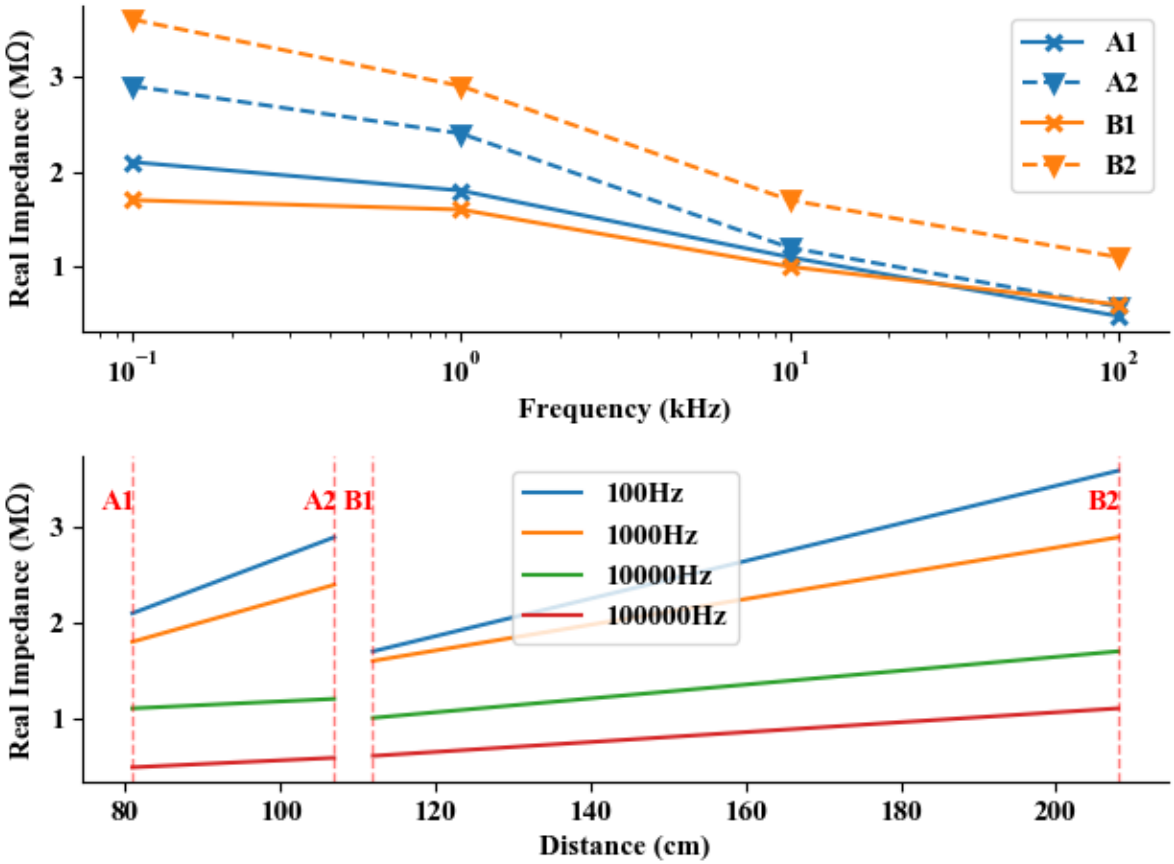

Figure 14: Potted plant impedance tests with subplots showing real impedance versus logarithmic frequency (top, subplot (a)) and real impedance versus distance (bottom, subplot (b)).

Subplot a in Figure 14 above, shows similar gradients between 100Hz to 1kHz and 10kHz to 100kHz, with a steeper slope in between. Subplot b in Figure 14, shows this again with grouping between pairs at the lower frequencies (100Hz and 100kHz), and higher frequencies (10kHz and 100kHz).

While there are too few data points to conclude, these are similar to dispersion characteristics in other biological tissues. In such tissues dielectric constant decreases in distinct steps with increased frequency [113] (shown in Figure 15 [113]), appearing in the same frequency range of α-dispersion.

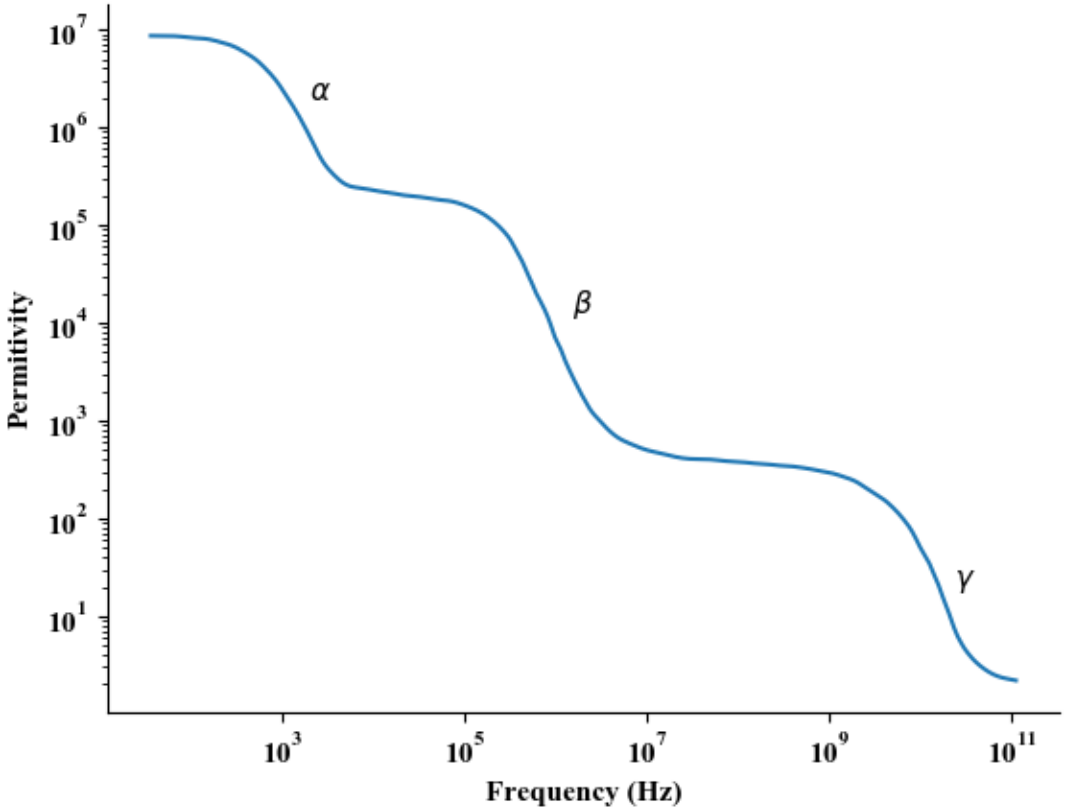

Figure 15: Plot of idealised relative permittivity of typical biological tissue with frequency variation, showing alpha, beta and gamma dispersions as labelled.

The range of frequencies and resolution tested is limited, but the change in slope could be indicative of the tested frequencies being on either side of the α-dispersion. The tested frequencies do end where β-dispersions typically becomes apparent. β-dispersions are accepted as being caused by membranes between cells in living tissues [113-115], however the cause of α-dispersion is still not concluded. While typically the tissues studied are from animals, the cell structure of plants is similar, both belonging to the eukaryote domain [116] with plants additionally having a cell wall not seen in animals. The addition of the cell wall could also mean increased capacitance between cells and β-dispersions occurring at a higher frequency. Validating similarities in the electrical properties of plant tissue to animal tissues would require a wider range of sampling frequencies at a higher resolution.

2 Impedance of grapevine sections

The results of the previous testing showed interesting relations with distance to soil. While not providing direct impact on the project, testing was conducted to investigate the variation in plant impedance at various locations in the leaf to ground path. Measuring for impendence sources within the plant required dissection. The initial cut was take from just above the soil line indicated by Figure 16 [117], a. with subsequent cuts up to the leaf stem of the leaf with the electrode.

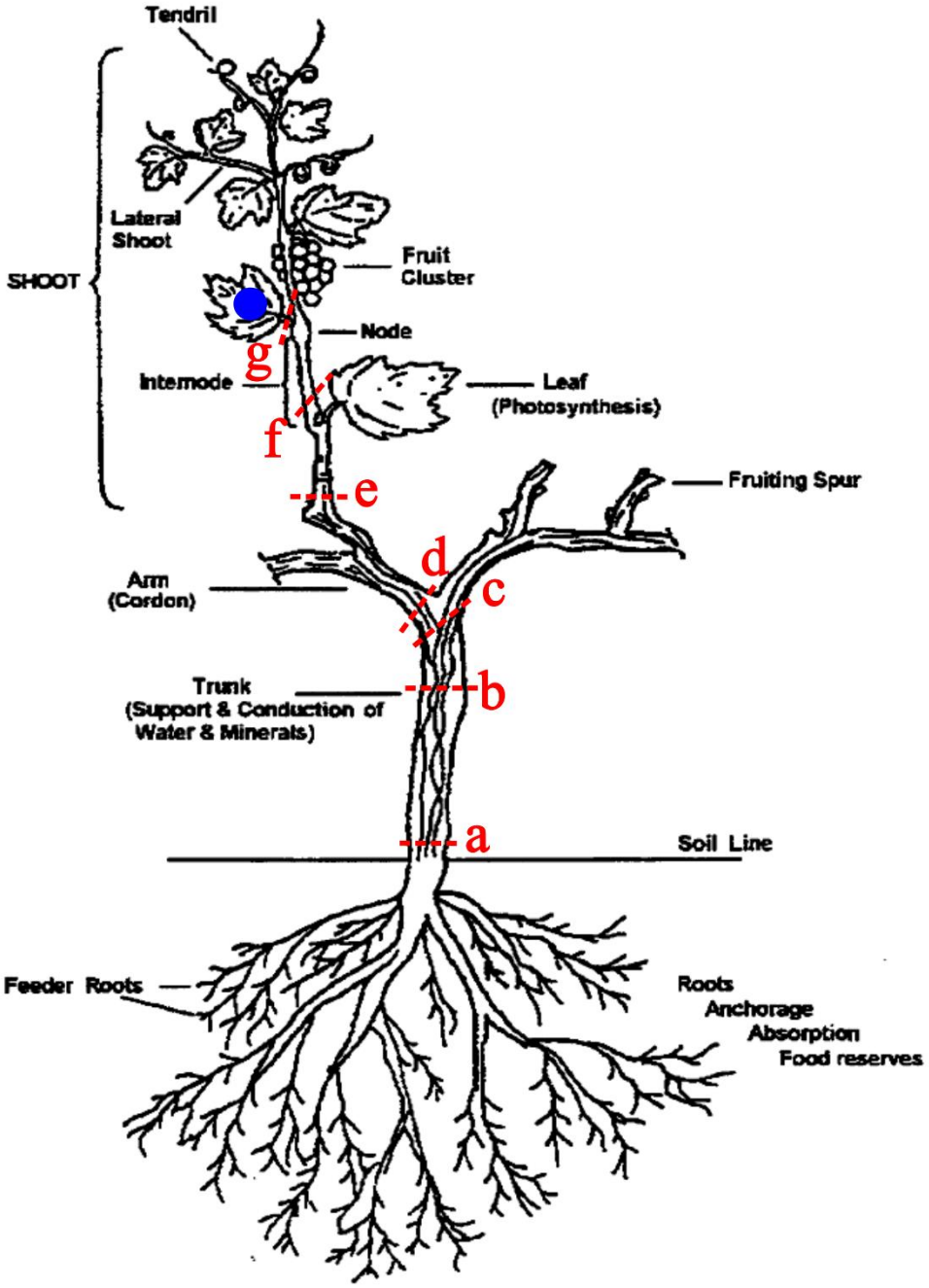

Figure 16: Anatomy of the grapevine. With permission from R.A. Hamman. Modified to show cut points: (a). above soil line, (b). above graft knot, (c). top of trunk, (d). start of arm, (e). start of shoot, (f). along shoot after fork, and (g). at leaf stem. The blue dot indicates leaf electrode position.

The plant used in this test was a potted grapevine approximately six months old. For the week prior to testing, the plant was well watered and maintained in a saturated condition

For the leaf side electrode a 3M Red Dot 2235 was used. 200ml of phosphate buffered saline (PBS) solution was used as contact on cut edge, placed in a plastic beaker with a stainless steel plate. The PBS (Invitrogen 00-3002), creates a solution of 10mM phosphate and 150mM of sodium chloride with one tablet PBS dissolved in 100mL of water [118]. When measuring, the cut edge was fully submerged, exposing all fibres to the PBS solution to ensure optimal contact. The cutting was fixed with an insulated retort stand to prevent parallel paths.

Contact resistance with 3M Red Dot either side of target leaf measured at 30kΩ, PBS solution 3M Red Dot on opposing sides of leaf at 150Ω.

Results

The results of this testing are shown below in Table 2. Again, the trend of capacitance values suggests contact capacitance from the electrode.

Table 2: Results of sectional grapevine testing. Noting reactance is inversely proportional to capacitance, these represent small values of capacitance.

Cut location	Electrode Spacing (cm)	Frequency(Ω)			
		100	1,000	10,000	100,000
above soil line	170	4.0e6 - 4.5e7j	3.0e6 - 8.0e6j	1.6e6 - 2.9e6j	1.2e6 - 6.4e5j
above graft knot	155	4.0e6 - 4.5e7j	3.0e6 - 8.0e6j	1.6e6 - 2.9e6j	1.2e6 - 6.4e5j
top of trunk	122	3.8e6 - 4.5e7j	2.9e6 - 8.4e6j	1.7e6 - 3.3e6j	1.3e6 - 6.6e5j
start of arm	110	3.6e6 - 3.5e7j	2.7e6 - 5.9e6j	1.4e6 - 2.7e6j	7.6e5 - 2.4e5j
start of shoot	35	3.0e6 - 3.0e7j	2.4e6 - 5.0e6j	1.2e6 - 1.7e6j	4.9e5 - 2.0e5j
along shoot	20	2.3e6 - 2.4e7j	2.2e6 - 3.8e6j	1.0e6 - 1.4e6j	4.1e5 - 1.7e5j
at leaf stem	10	1.1e6 - 1.9e7j	7.4e5 - 3.0e6j	4.0e5 - 1.2e6j	1.6e5 - 1.4e5j

Ignoring the capacitive contributions, plotting distance to leaf electrode versus resistance yields Figure 17.

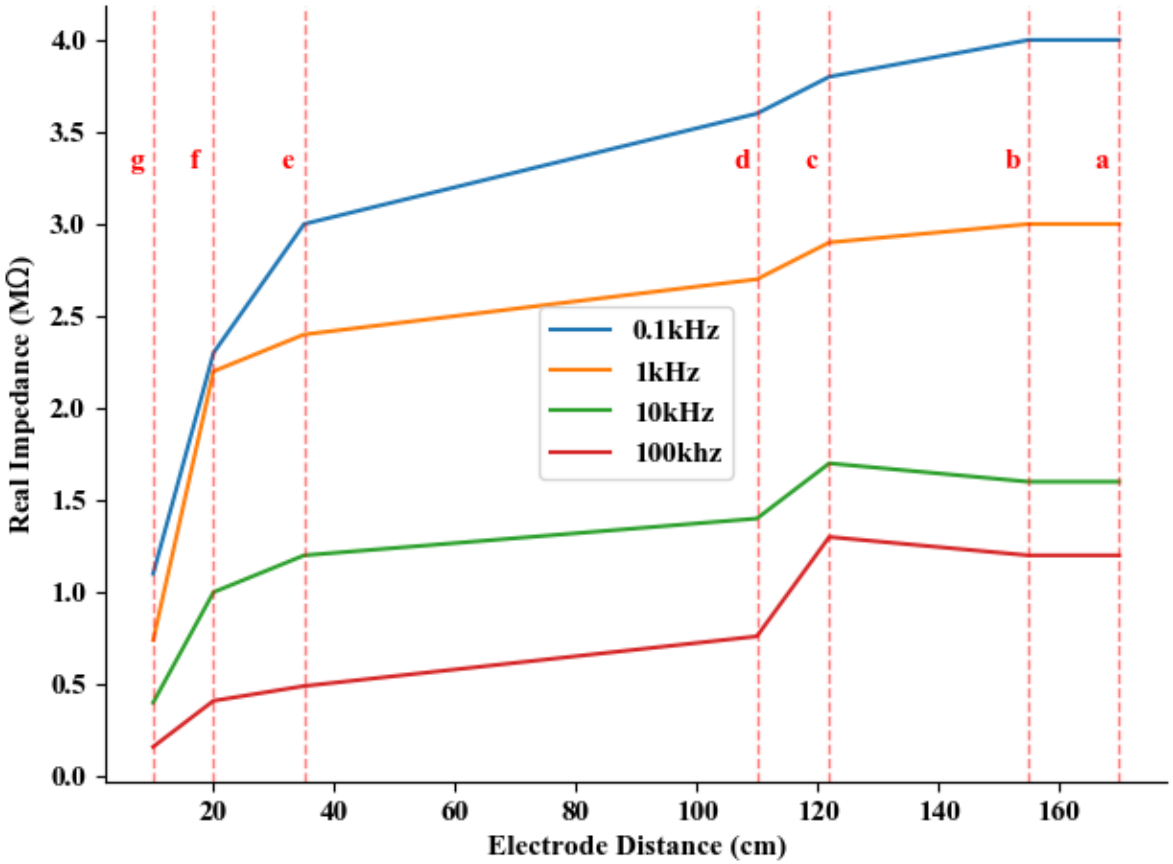

Figure 17: Distance to leaf electrode vs. Resistance. Red dashed lines represent cut lines at a) Above soil line, b) Above graft knot, c) Top of trunk, d) Start of arm, e) Start of shoot, f) Along shoot after fork, g) At leaf stem.

In Figure 17, plant limb transistions (where a shoot stems from) show the greatest changes in resistivity. This would imply that these transitions are the major contributing points to impedance. This follows intuition, as wood grain is usually longitudinal with the stem [119]. At these sections the fibre direction changes to anchor the offshoot into the shoot it comes from. The increase between b and c at higher frequencies is unknown, but could be due to inductive effects, or magnetic coupling with testing equipment when the measurement was taken.

The f-g junction at the base of the leaf is the largest single source of impendance in the leaf to earth path. This implies that any retained charge would likely be localised at each leaf, with slower charge transfer to other leaves than to earth. High impedance at junctions may cause some issue spraying leaves that either are many junctions from the root system of the plant, or share junctions with many nearby leaves. This could alter the spray distribution at high charge ratesthough the magnitude and effect on outcomes is unknown.

The limited sample size is too small to draw any quantative conclusions on. Further investigation would be required to validate any observations. An improved methodology of measuring charge transfer would also be required to quantify the effective capacitance of the leaf systems.

High Voltage Power Supply

Essential to an electrostatic system is the high voltage dc power supply. In the standard ESS sprayer, the power supply came as an integrated unit within the handle of the sprayer powered by two 9V batteries in series. Unfortunately, before testing the voltage supply for output characteristics, the supply failed during initial droplet size and velocity testing. The New Zealand technician for Electrostatic Spraying Systems stated that an in-specification sprayer should have a voltage of approximately 1200 V on the spray when measured with a plate near the nozzle tip. Initial sprayer testing with an iSeg 2000V supply showed the spray voltage was approximately half of the nozzle voltage, requiring 2400V at the nozzle to match the standard specification. Prior to finding this information, a cascaded flyback system (in essence an isolated boost converter) was designed to output between 1000 and 1500V. A revised design, two stages consisting of a boost converter and full-bridge converter with voltage doubler output, was fabricated. This solution has an output voltage between 1500V and 4000V, allowing for testing above and below the standard specification.

1 Design Overview

As the system requires the use of high dc voltages, the amount of output capacitance used for ripple suppression was a major consideration. Higher capacitance values reduce the output ripple voltage, but increase stored energy and potential harmful electric shock risk. In consideration of this, 0.05J of stored output energy was chosen as the upper limit as this was determined to pose a very low risk for harm.

To meet the higher voltage requirement, an appropriate two-stage unit was designed. The first stage was a boost converter and the second stage was a full-bridge converter with a voltage doubler output stage. The boost converter has been designed to output variable voltage between 15V and 40V, while the full-bridge/voltage doubler converter steps up a fixed 1:100 ratio. The full-bridge converter was chosen over a flyback as only a single stage required variable output and operation of the full-bridge/voltage doubler converter is simpler, with a fixed duty cycle. The fixed duty cycle at 80% also reduces output ripple at a given output voltage.

Assuming a spray rate of 0.2 kg/min and a charge to mass ratio of 10 $\frac{uC}{kg}V$ [42] imparted from nozzle to spray, the spray current is then 13.3μA at 4 kV. Early on in the design, it was decided to have a dummy load of less impedance than the spray to ensure stable operation in the no spray condition and to keep ripple current down to keep the boost converter in continuous mode. For this, 3.4 MΩ impedance was used, also serving the purpose of a voltage divider to monitor the output voltage of the full-bridge converter. This results in a current through the dummy load of 0.447 mA at the design minimum of 1500 V and 1.19 mA through the dummy load at the design maximum 4kV. Assuming an efficiency of 80 % for the full-bridge converter, this gives boost converter output currents of 62 mA at 15 V and 166 mA at 40 V.

2 Boost Converter

The PCB manufacture and construction for this converter was completed, but it was never used. This was due to testing was exclusively conducted in a laboratory environment, and the available Iso-Tech IPS2010 benchtop power supplies providing the same practical functionality. However, the design is described below.

The variable voltage output was achieved with the use of a UC3843 current mode DC-DC PWM controller. The IC is designed to drive a switch-mode converter at fixed output voltage, however the design calls for variable output voltage. As such, slight alterations to the external circuitry were made. The internal error amplifier was bypassed, using an external opamp on the compensation pin. This allowed bypassing the internal 2.5V reference voltage and an external variable reference voltage applied. This is functionally shown below in Figure 18, and its implementation in the boost converter schematic is shown in Figure 19.

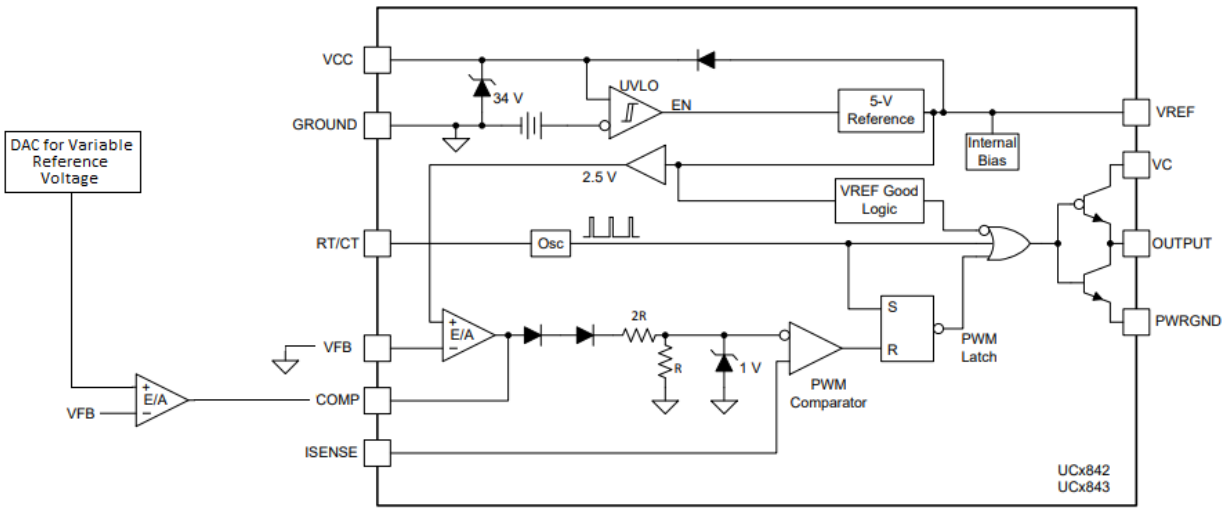

Figure 18: Functional block diagram showing VFB bypass on UC3843 controller.

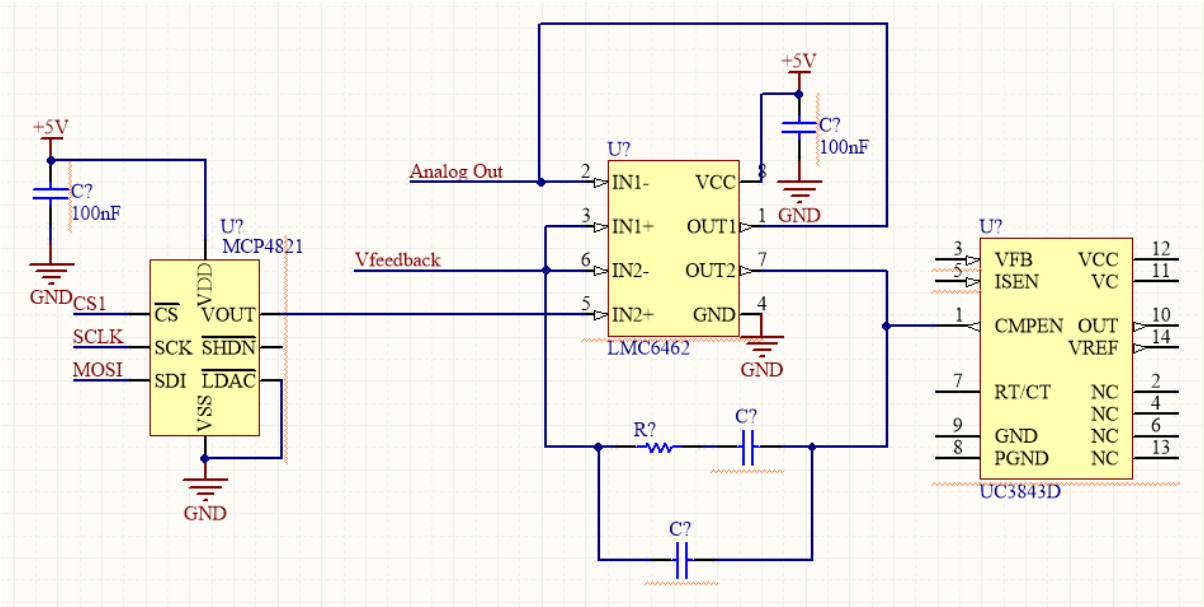

Figure 19: Section of boost converter schematic showing VFB bypass on UC3843D.

With the secondary stage having a fixed 100 times step up and a system output of 1500 to 4000 V, the boost converter must have an output range of 15 to 40 V.

Assuming negligible losses from the diode, inductor dc resistance and MOSFET, equation 10 gives a minimum duty cycle of 20 % for 15 V output and maximum duty cycle of 70 % for 40 V output.

The TDK RM 8 inductor core was used for hand winding the inductor, as this was readily available with bobbins on campus. The core has an effective area (A_e) of 64 mm^2, and being made of N87 material [120], should have a maximum flux density below 390 mT at 100 degrees to avoid saturation of the core. 100 degrees was used as a reference value as the saturation point decreased as temperature increases and it represents a worst-case scenario. The core has an ungapped inductance factor (A_L) value of 4400 (+30/-20 %) nH [121].

To ensure continuous mode operation, the inductor must be sized such that the inductor current stays above zero. As long as output current stays above the minimum critical value $I_{O(crit)}$ (A), the minimum inductance value to inductor current above zero is given by [68]:

$$L_{min} \geq \frac{V_o \times T_S}{16 \times I_{O(crit)}} \tag{11}$$

At a given output voltage V_o (V) and switching time T_S (s). With the minimum output voltage of 15 V and corresponding current value of 62 mA this gives a minimum inductance of 302.4 µH at a switching frequency of 50 kHz. With the A_L value of 4400 (+30/-20 %) nH, and assuming the lower tolerance value (3520 nH), this gives a minimum number of turns as 86 (303 nH). The average inductor current is then given by [68]:

$$I_{Lavg} = \frac{I_O}{1 - D} \tag{12}$$

For the maximum design voltage of 4000 V and the corresponding current, 166 mA, and duty cycle, 70 %, this gives an average current of 553 mA. Then calculating for the inductor current change given by [68]:

$$\Delta I_L = \frac{V_L}{L} \times \Delta T \tag{13}$$

At steady state operation, $\Delta I_L(+) = \Delta I_L(-)$, then $V_L = V_{in}$ for $\Delta T = DT$. This gives a ΔI_L of 443 mA. Now calculating peak inductor current, given as:

$$I_{Lpeak} = I_{Lavg} + \frac{\Delta I_L}{2} \tag{14}$$

This gives a peak inductor current of 775 mA. Now finally, maximum magnetic flux density can be calculated. This is given as [122]:

$$B_{max} = \frac{L I_{peak}}{n A_e} \tag{15}$$

With the calculated values 303 nH, 775 mA, 86 turns, and the given value of 64 mm^2, the maximum flux density is 42.7 mT. Well below the maximum value of 309 mT. Note that this is the minimum number of windings required for the minimum inductance required. For a margin of error, 100 turns were used. Calculation of capacitance required for desired ripple voltage is comparatively simple. This is given by [68]:

$$C \geq \frac{I_{Omax} \times D_{max}}{f_{sw} \times \Delta V_O} \tag{16}$$

A desirable ripple voltage would be less than10 % (or 4 V). This gives a minimum capacitance value of 581 nF. This is a very small capacitance and a much larger one can be used in its place. A 47 µF capacitor was used, as these were readily available. This gives a ripple current of 0.049 V or 0.12 %.

Complete schematic and artwork for this PCB is shown in Appendix 1

3 Full-Bridge and Transformer

The second stage, a full-bridge converter is a fixed step up ratio of 1:100. The design consists of a self-oscillating full-bridge gate driver, a MOSFET full-bridge, transformer and a rectification stage. The IRS2453D self-oscillating full-bridge gate driver provides integrated oscillation, dead time control, gate driver and high-side bootstrapping in a single package. In this application, the oscillator runs at 100 kHz, the maximum for the driver. Given the fixed dead time of 1µs, this results in a duty cycle of approximately 80% full-wave.

The original design for this stage utilised a centre-tapped secondary winding transformer to minimise the number of high voltage diodes while still giving full wave rectification. With 80% duty cycle, this requires 1:125 ratio of primary to secondary windings not accounting for any diode losses.

The main concern when designing a transformer for this application is the maximum magnetic flux density within the core. Too high a magnetic flux density and the core will saturate, resulting in inefficiencies and heat. As the transformer inductance is not used for smoothing in a full-bridge converter, the inductance is not a primary concern.

The core utilised is an RM 12 core, again used because of easy access to cores and bobbins. This core has an Ae of 146 mm^2 [123] and being N41 core material, the saturation flux density is 390 mT at 100 degrees [124] (used for worst case scenario). As the full-bridge converter is driven symmetrically, the flux swing (ΔB) will determine the maximum flux density in the core. This is given by [122]:

$$\Delta B = \frac{V_{in} D}{n A_e f} \tag{17}$$

At the maximum input voltage of 40 V, a fixed duty of 80 % and frequency of 100 kHz, the minimum turn requirements to be blow 390mT is 6 turns. Primary turns were selected as seven as it gave some additional headroom without increasing the secondary windings excessively. This gives a maximum flux density of 313 mT, below the maximum value but enough to cause some core losses. Secondary turns number is then 875 either side of the centre tap.

Energy stored in a capacitor is given as [125]:

$$E = \frac{CV^2}{2} \tag{18}$$

At the maximum designed voltage of 4000 V, and a maximum energy of 0.05J this give a maximum capacitance of 6.25 µF. With a maximum output current (combined spray and divider currents) of 1.33 mA, output voltage ripple at this capacitance would be 1.7 mV (from equation (16)).

Achieving symmetrical winding of the transformer proved to be difficult, with the first and second attempts resulting in voltage asymmetry on either side of the centre-tap, though both secondary sets of windings were equal in number. The cause was likely due to winding impedance variation, and since a successful alternative design was implemented (described below) the performance issue was not further investigated.

To move forward, a redesign was carried out that forewent a centre-tapped transformer. Preferably using the original PCB's and components already on hand. The simplest way to achieve this was to incorporate a transformer with a single secondary winding connected to a voltage doubler on the output. A full wave voltage-doubler is in essence two series peak detect circuits. Each of the peak detect circuits function as half-wave rectifiers, providing full wave rectification between them. The voltage output of this circuit will be approximately double the output voltage of a

normally rectified circuit but incurs double the diode conduction losses [73]. These losses limit voltage-doubler circuits to low power applications, which is appropriate in this case.

The primary windings in the transformer was kept at seven, resulting in no change in the maximum flux density. Implementing this change allowed the majority of components to remain unaltered from the original PCB design and the transformer to have a single set secondary windings. The design change is illustrated below in Figure 20.

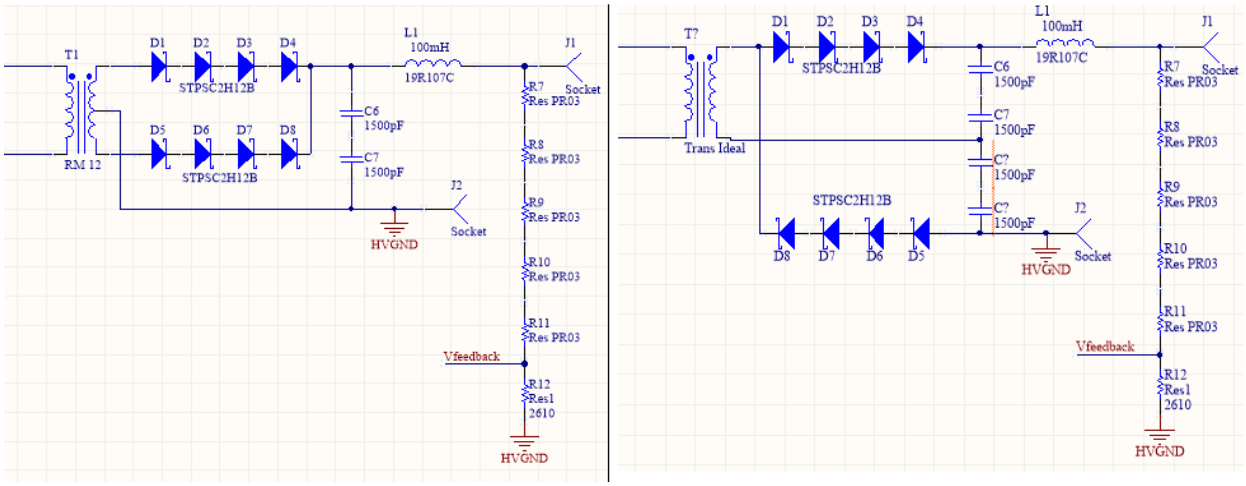

Figure 20: Original design (left), Voltage-Doubler design (right).

Because of the design change, the PCB was modified to accommodate the new circuitry. The change also had the added benefit of quartering the maximum voltage difference on the transformer from 8kV to 2kV. Output capacitance halved as a result of the configuration changes, requiring a doubling of the capacitor values to achieve the same ripple performance as previously calculated. This revised configuration was tested and verified to produce up to 4kV at the output as designed, however it was found that near the upper voltage, the transformer would arc between layers of windings despite having PET tape as insulation between winding layers, shown in Figure 21.

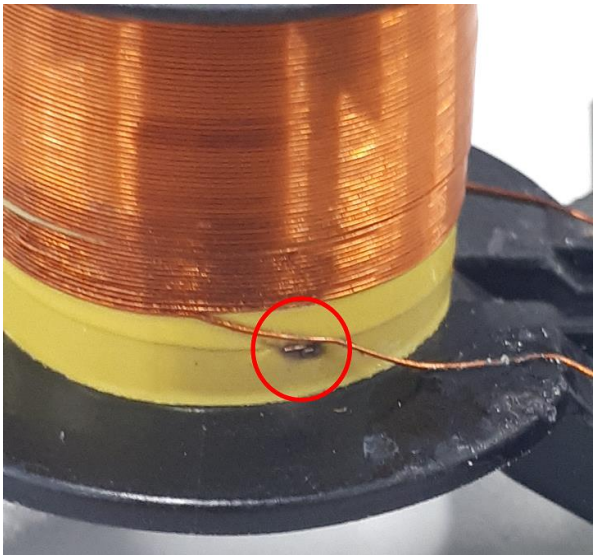

Figure 21: Damage to insulation between winding layers caused by arc discharge - highlighted in red. The arc occurred at the edge of an overlapping layer of insulation where only a single layer was present.

As an effort to remedy arcing, additional insulation was added between winding layers and additional air gap for creepage. The transformer was rewound with the addition of cellulose acetate between winding layers and 3mm of

clearance distance between the edge winding and bobbin edge, to give 6mm of creepage clearance between layers. The alternating configuration of windings over eight layers and 2kV peak voltage, the maximum difference between layer windings at the edges would be 250V. This gives a maximum potential of 41.7 V/mm between layers, low enough that arcing should not occur.

However, the effect was persistent after the rewinding, occurring around the edges of the cellulose acetate sheets. Given the low electric field strength between windings, partial discharge is more likely to be the cause of the failure, with breakdown occurring between the higher voltage windings at the outside of the transformer and free air; common in transformers with air pockets due to deteriorating insulation [126]. The transformer still provides the expected step-up ratio, where arcing would cause short circuits across the windings. The unstable output voltage further evidences this.

Areas of concentrated electric field within air pockets inside the transformer cause the air to become ionised, resulting in partial discharge. Replacing the air within and around the transformer windings with a higher dielectric strength material increases the breakdown voltage, helping prevent partial discharge from occurring. The transformer was potted with a silicone polymer, Sylgard 170, that has a dielectric strength of 18 kV/mm [127] compared to air at a dielectric strength of 2.98 kV/mm [128]. Complete removal of air pockets required complete coverage of the windings in Sylgard, and then being held in under a vacuum of 30inHg (101.6kPa) prior for 2 minutes prior to curing. The transformer windings before and after potting is shown in Figure 22.

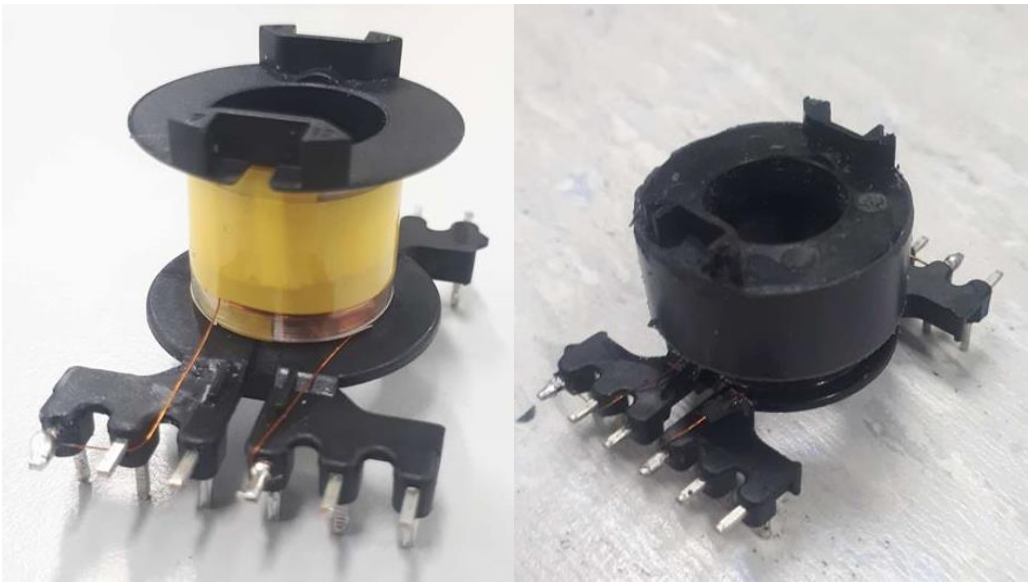

Figure 22: Transformer bobbin with cellulose acetate sheets before (left) and after (right) the Application of SylGuard 170.

The output voltage vs input voltage is shown in Figure 23

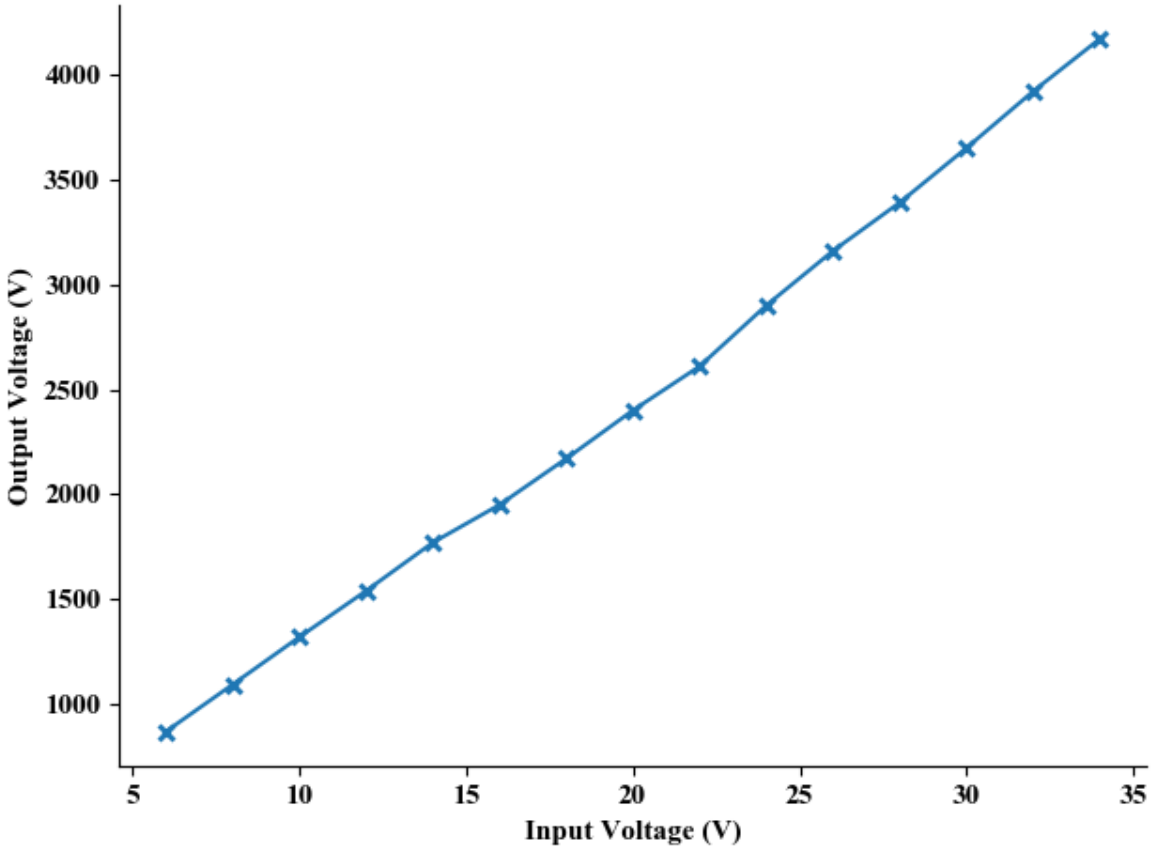

Figure 23: Input voltage vs output voltage for full-bridge converter.

The step-up was a bit more than the designed as was the current draw. The high magnetic flux density in the inductor core was a source for significant losses. Operating at the design maximum would cause the core to get warm to the touch. Ripple voltage was also higher than calculated though still below 5 %. While this design could use with more refinement, it provided the voltages needed for experimentation, while also being simple and isolating the low voltage and high voltage stages

Schematic and artwork for the full-bridge converter PCB in Appendix 2.

Imaging

Analysis of droplet motion is a key part of understanding the influence electrostatic charges have on atomised droplets and the outcomes this will have on spray deposition. As these droplets are moving at high velocities (20-40 m/s), capturing their motion requires high-speed imaging (HSI). To achieve this, a Fastcam SA5 (henceforth referred to as SA5) by Photron was used. The sensor on this camera offers a maximum 1024 x 1024 pixel resolution with 20 µm pixel size, and frame rates up to 775,000 FPS [129].

The camera offers two frame rate modes, 150K and 775K, where 150 and 775 represent the maximum frame rate in kilo frames per second (kFPS). 150K mode provides better image quality at a given framerate over the 775K mode, but with slightly lower image resolutions for a given frame rate [129]. The 150K mode also provides an increased number of resolution steps compared to 775K mode. Given that 775 kFPS would not be required, and the increased number of frame rate and resolution steps, data was captured in 150K mode. The possible frame rate settings are shown below in Table 3. Resolution decreases as framerate increases due to write speed limitations with the on-board memory.

Table 3: Excerpt from SA5 datasheet showing possible frame rate settings between 5000 and 10000 FPS in 150K mode.

Image Size / Frame (FPS)	1,024 × 1,024	1,024 × 896	1,024 × 752	1,024 × 640	1,024 × 512	896 × 896	896 × 752	896 × 640	896 × 512	768 × 768	768 × 640
5,000	○	○	○	○	○	○	○	○	○	○	○
5,400	○	○	○	○	○	○	○	○	○	○	○
6,000		○	○	○	○	○	○	○	○	○	○
7,200			○	○	○		○	○	○		○
8,000							○	○	○		○
9,000								○	○		○
10,000											○

Preliminary measurements taken with Phase Doppler Interferometer (PDI) with Scott Post found droplet diameters range between 10 to 100 µm with a median diameter of approximately 50 µm. At 1:1 magnification, a median-sized droplet will only shade a maximum of 4 pixels in a frame and a 20.48 x 20.48 mm field of view (FOV). While larger magnifications would be desirable for pixel coverage, the reduced FOV would minimise the observable distance of droplet-target interaction.

The frame rate required to image droplet motion smoothly is dependent on droplet velocity. For ease of tracking, droplet velocity in pixels per frame (PPF) should be less than the number of pixels the droplet covers. This will aid in analysis as droplet paths will likely intersect. However, with increasing frame rate, the compromise is a lower resolution and hence reduced FOV. Preliminary testing showed droplet velocities at approximately of 30 m/s. With this velocity figure and assuming unity magnification, the droplet movement between frame captures (PPF) is approximated by:

$$\frac{pixels}{frame} = \frac{{}^{m}/_{s}}{{}^{m}/_{pixel} \times {}^{frame}/_{s}} \tag{19}$$

With a pixel size of 20 µm, and an assumed velocity of 30 m/s, the pixel movement per frame is given with the values in Table 4.

Table 4: Framerates and pixel per frame velocities assuming a velocity of 30 m/s.

FPS	5000	5400	6000	7200	8000	9000	10000
PPF	36	33.33333	30	25	22.5	20	18

In practice, if the required framerate requires reduced resolution, the optimal framerate will be the lowest that can reliably have the droplet path information extracted.

Another practical consideration that will be dependent on the experimental configuration is the amount of available light. Critical to capturing quality images at high speed, is ensuring adequate light reaches the sensor. As minimum shutter speed is inversely proportional to frame rate, increasing frame rates require increasing illumination to achieve the same exposure.

A modular support structure was constructed by Mark Jermy to house the mounting of the various pieces of equipment necessary to facilitate repeatable observation of droplet motion. The support structure, constructed from 20 x 20 mm aluminium t-slot extrusion is shown in Figure 24.

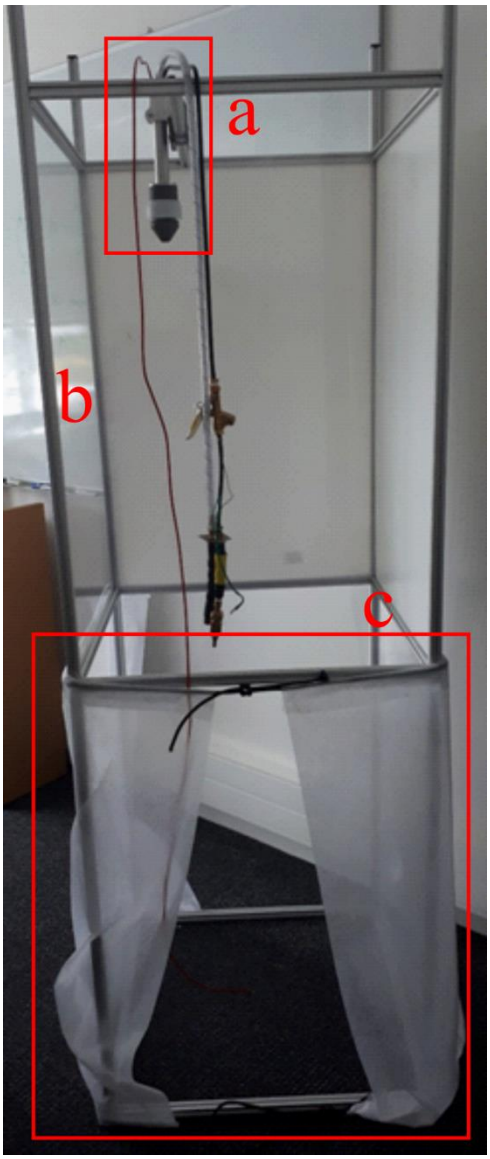

Figure 24: Support structure as originally configured. (a) Nozzle with attached hoses, (b) Perspex sheets to allow viewing of spray cone, (c) fabric catch to minimise spray losses to surrounding area while minimising deflections. Note the structure is shown vertically, but is horizontal in testing.

The structure was originally configured to have Perspex panels along the two sides around the nozzle to facilitate observation of the spray cone as it left the nozzle. Modifications were made to facilitate the observation of a target within the spray cone. Namely, the addition of a target-mounting fixture and the movement of the Perspex to surround the target as opposed to nozzle.

1 Optical Imaging

Initially, the conceptually simpler approach to imaging was taken, using standard available optics with the high-speed camera to capture droplet motion. A Model K2 DistaMax (MK2) long distance microscope [130] with a 30-Watt LED spotlight as the light source was used. The MK2 was provided with the Centritel focuser, CF-1/B and CF-2 objectives. With these, some alterations to the magnification and focal length could be made. The LED spotlight contains an internal rectifier that does not allow mains AC frequency to induce flickering.

The thread engagement of the c-mount standard does not provide adequate support for a lens the size of the MK2. A fixture plate was fabricated to support both the camera and lens while allowing for 3-point planar adjustment relative to a flat surface.

The datasheet provided by Infinity USA for the MK2 provides MAG and FOV values based on a ½ inch format sensor [130]. The c-mount adaptor provided with the Photron SA5 and the data provided on the MK2 datasheet retain the standard flange depth of 17.526mm for c-mount. As such, no complex conversions for depth of field (DOF), working distance (WD), and magnification (MAG) are necessary. Correction factors are provided for other common inch-based sensor formats with values representing the difference in area the sensors occupy within the lens's projection cone. While inch-based formats have an aspect ratio of 4:3, the magnification and FOV are dictated by the sensors horizontal size. To find the correction factor, dividing the horizontal sensor dimension of the SA5, 20.84 mm, by that of the ½ inch format, 6.4 mm, yields a factor of 3.2. The ½ inch format values for magnification from the datasheet for the objectives are shown below in Table 5, along with the corrected values for the SA5 sensor format.

Table 5: Model K2 DistaMax with Centritel focuser in central position[130].

	STD			CF-1/B			CF-2		
	Near	Mid	Far	Near	MID	Far	Near	MID	Far
WD (mm)	290	355	420	192	221	250	125	137	148
MAG	1.60	1.07	0.80	2.42	1.75	1.40	3.56	2.67	2.13
MAG SA5	5.12	3.42	2.56	7.74	5.60	4.48	11.39	8.54	6.82
DOF (mm)	0.13	0.19	0.27	0.06	0.07	0.09	0.02	0.03	0.03

The working distances described in Table 5 are only valid for the Centritel focuser in the central position. However, the WD can be increased and MAG decreased with adjustment of the focus ring and increasing distance to the subject. The DOF is also altered through adjustment but not in a significant manner.

1.1 Optical Imaging Testing Methodology

Four specific tests were designed to allow observation of electrostatic effects on deposition.

In summary (full descriptions in Appendix 3), these tests were:

1. Effect of target impedance on charge retention.

This test aims to measure if charge retention will occur/have an effect on the interaction between droplets and the target for a spray period of less than one second. The extreme cases will be tested first, low impedance earthed and open circuit. If there is an observable difference in droplet-target interaction, impedances within the range found on a potted grapevine (1 MΩ) will be tested in stepped values after high-speed footage can be analysed.

2. Nozzle voltage relationship with droplet-target interactions.

This test is to measure the relationship between the magnitude of droplet-target interaction and the nozzle voltage.

3. Variation of droplet-target interaction within spray cone.

This test is to investigate if there is variation of the wrap around effect within the spray cone due to variation of charge distribution within the spray cone and to measure if the effect decays at increased distances from the nozzle.

A number of lighting angles were trialled with the best having the camera perpendicular to the spray path, with light sources alongside the camera at a low angle converging at the centre of the spray path (illustrated in Figure 25).

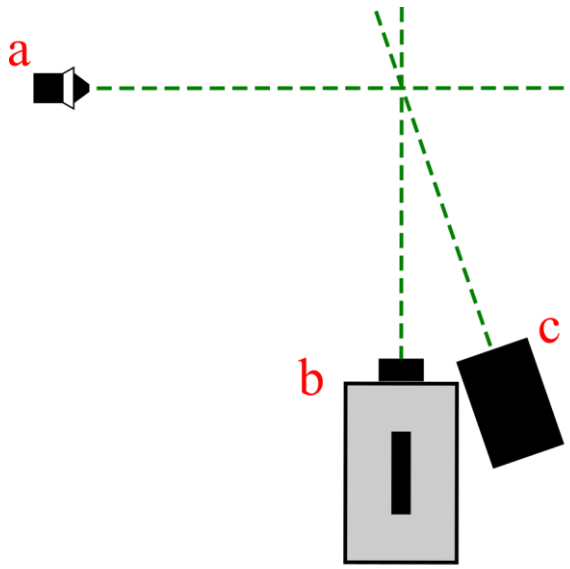

Figure 25: a. Nozzle, b. SA5+MK2, c. LED spotlight. Green dotted line to represent converging directions of a, b, and c. Shown from top view.

Having the light source at a low angle from the camera allowed the droplets to reflect the light back to the sensor. The 30 Watt light source provided sufficient light to illuminate the droplets at the desired frame rate.

Testing in this case revealed significant shortcomings of the MK2 for this application. While magnification was sufficient, the DOF was very narrow. The result of this being droplets moving in three dimensions passing through the focal plane as they crossed the frame. Owing to this, droplets could not be observed from one edge of the frame to the other. As such, no workable footage was captured for tests one through three.

2 Diffraction Imaging

The inability to effectively image individual droplet motion with the Model K2 DistaMax necessitated the implementation of an alternative solution. As a second method of imaging, as laser source was investigated. In principal, the collimated beam provides the light source and casts silhouettes of objects passing through the beam onto the sensor in manner similar to coherent diffraction imaging but at a larger scale. Being a coherent and very low divergence source eliminates the need for additional optics such as a lens. The collimated beam is placed perpendicular to the camera sensor with only the objects of interest passing through the beam. Particles travelling between the laser source and sensor create visible disruptions to the beam pattern, observed by the high-speed camera sensor. While not investigated, magnification is possible by altering beam divergence and sensor distance.

Using a laser introduces associated health and safety risks. Alterations to the optical imaging test configuration had be made to allow for testing and ensure adequate health and safety precautions are used. The low power density and wavelength of this configuration meant that this laser fell under laser class 2: meaning a visible beam and safety given a normal aversion response (typically ¼ second exposure[131]). As the test apparatus is not in a restricted access area, adequate safety systems had to be introduced to eliminate the risk of accidental harm to other users in the workspace. The apparatus was modified to include a beam enclosure, and hard mounting of the collimated laser module to the test rig. The sensor of the high-speed camera provided a beam stop. This is shown graphically in Figure 26.

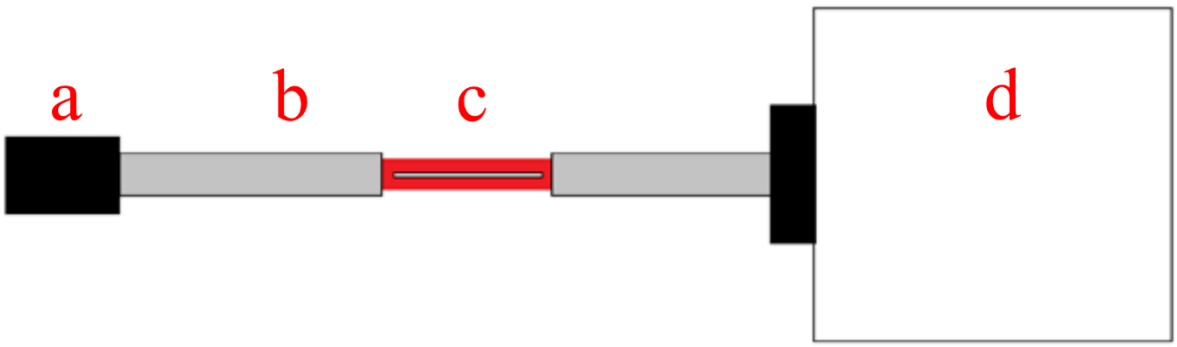

Figure 26: Illustration of imaging apparatus. (a) Laser module, (b) PVC beam enclosure in grey, (c) target centrally positioned in laser beam, (d) Photron SA5 High-speed camera. Shown from above.

Alternative mounts were made for the fixture plate to mount the PVC beam enclosure. A cap was made to protect the sensor of the camera from both dust and water droplets during imaging, and provide a point for mounting a section of the beam enclosure. This cap used an optically flat (very high level of surface flatness below 2.54 µm to minimise light distortion) camera filter and a 3D printed housing. The optical flat does create a reflective surface, but as the optically flat filter is perpendicular to the beam, it is reflected back towards the origin and kept within the beam enclosure.

A Hitachi 5mW 635nm laser diode (model number HL6312G) provides the source of laser light. Initial testing showed the beam pattern provided by the diode was divergent with uneven intensity distribution. This is not at all desirable in imaging so some optics must be used to provide the desired low divergence collimated beam. This is achieved in a three steps. The beam first passes through a 50 mm microscope objective. This focusses the beam through a 10 µm pinhole. The pinhole acts as a spatial filter, removing undesired spatial noise from the system improving beam intensity distribution. The spatial filter is placed at 50 mm from the last lens of the microscope objective such that it converges as it passes through the pinhole. Finally, a 100 mm focal length biconvex lens is positioned 100 mm from the pinhole providing a low divergence collimated beam. Shown graphically below in

Figure 27 along with the physical implementation using the Thorlabs 30 mm cage system. As the biconvex lens has a diameter of 25mm, the collimated beam diameter is 25mm.

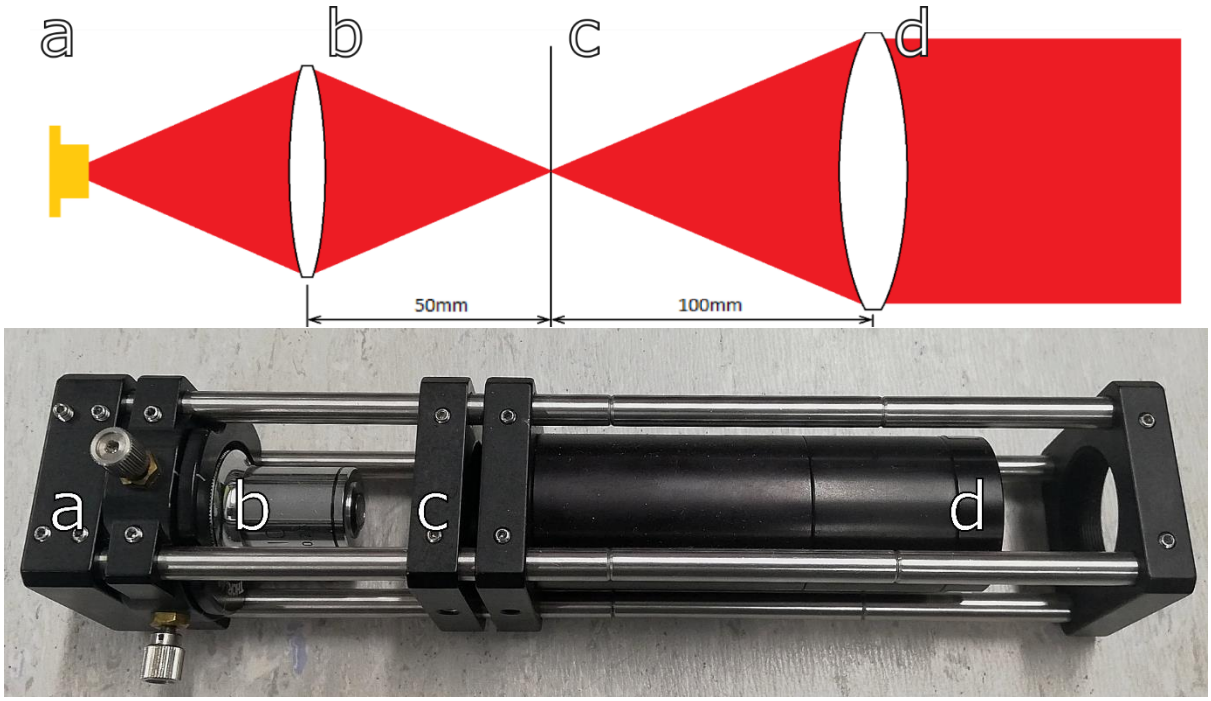

Figure 27: a. laser diode, b. 50mm objective with X-Y positioning, c. 10µm pinhole, d. 100mm biconvex lens.

The Thorlabs' 30 mm cage system provides a simple platform for securely mounting the components and facilitates mounting for the collimated laser module. A precision X-Y positioning mechanism is provided on the microscope objective mount for adjustment to ensure the converging beam passed through the pinhole. Providing the power needed to safely drive the laser diode is a Thorlabs LD1100 constant power driver.

2.1 Laser Imaging Testing

Continuing from imaging with optical methods, tests one through three were repeated with the aforementioned alterations to the testing structure. The complete test plan is shown in Appendix 4.

The output power of the laser was initially set to provide the full 5mw power the diode is capable of as constant output. At this power, a frame rate of 7200 FPS and a shutter speed of 1/frame rate, sections of the frames are overexposed and the pixels saturating. To prevent this the shutter speed was increased to 1/62000 second. As an added benefit, the increased shutter speed reduces blurring between frames.

The initial images (shown in Figure 28) captured with test methodology appeared to show a significant amount of noise. Further inspection of the images revealed that each droplet created a faint disc diffraction pattern. This pattern is similar to an Airy disc diffraction-pattern and the apparent noise were interference patterns caused by a large number of overlapping discs.

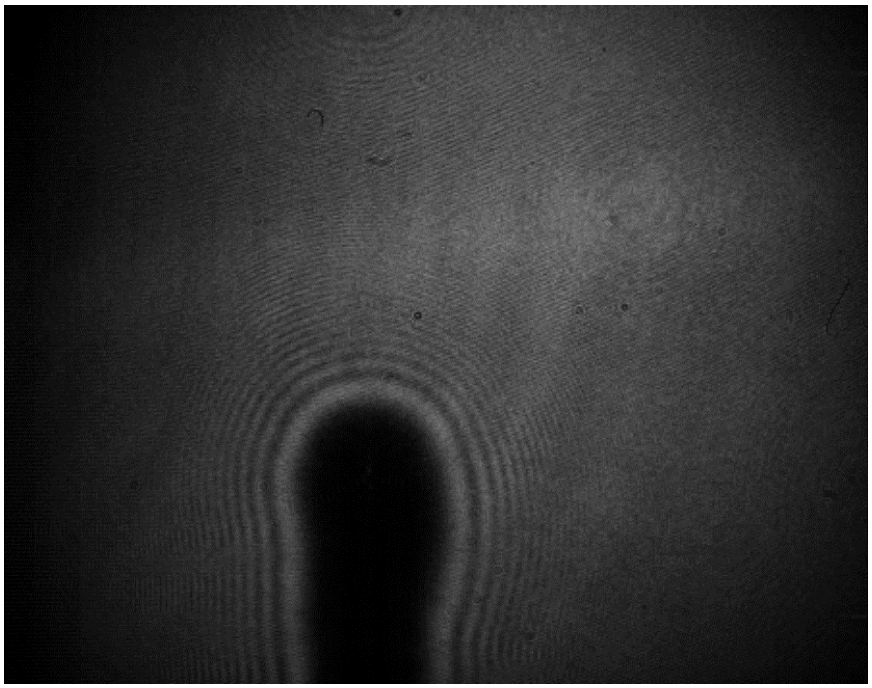

Figure 28: Still from video capture showing presence of faint diffraction patterns. The large blob in the centre of the image is the aluminium plate sitting within the laser beam. The plate is used at the spray target.

An Airy disc [79] is the resulting diffraction pattern of a spatially coherent source of light passing through a small circle aperture, which is a bright central disc surrounded by concentric bright rings, as shown in Figure 29.

Figure 29: Airy disc from laser through small circular aperture [132].

Ideally, a single droplet would be isolated and imaged, allowing verification of the Airy disc pattern created by diffraction around the droplets. This was not feasible in practice. However, it was possible to create photomasks that will allow light transmission similar to that of a singular droplet.

These photomasks consist of small aluminium disc approximately centred on a quartz plate. Aluminium is deposited onto the plate with Direct Current Sputtering, a method of thin film physical vapour deposition, resulting in a 100 nm film. The film is coated with a photoresist and the desired disc area is cured with a Heidelberg µPG-101 laser writer. The plate is then etched and the excess aluminium film removed [133]. The result is an inverted aperture of known size and shape. Photomasks were made in 15, 40, 60 and 80 µm circle diameters. Shown in Figure 30 is the 80 µm mask under 500x magnification.

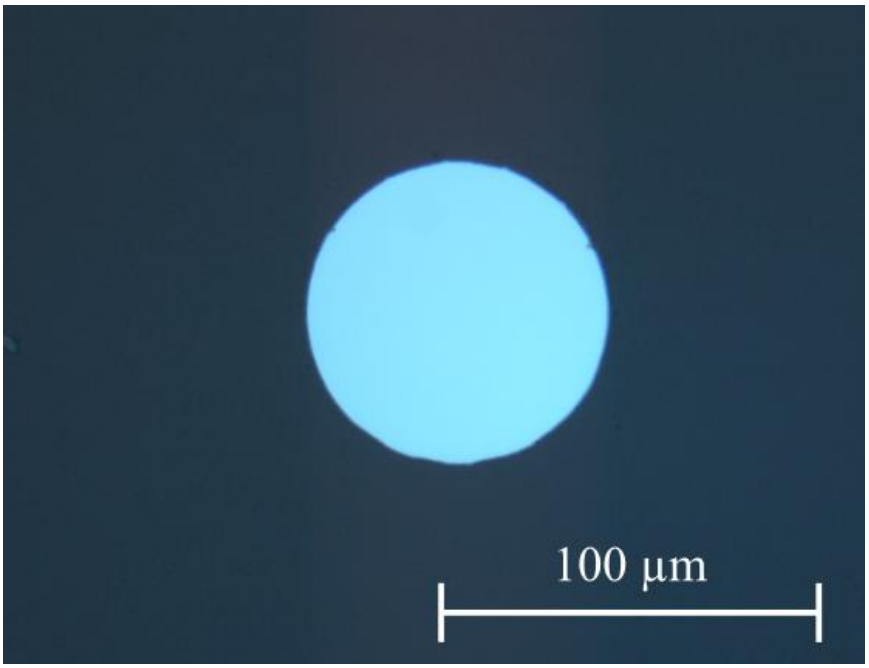

Figure 30: Close up of 80 micron mask at 500 times magnification. In this image the plate is front lit, resulting in the aluminium mask reflecting light back to the camera sensor and dark contrast with the clear quartz plate.

Some additional undesired areas of aluminium film were left on the quartz plate as a result of the etching process. However, their locations are known so can be accounted for. These are highlighted in Figure 31.

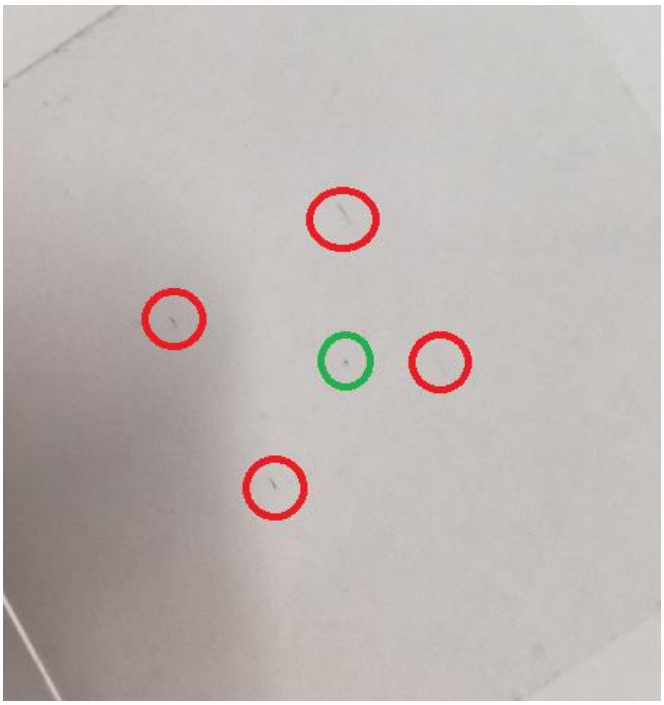

Figure 31: Full mask highlighting desired disc in green and undesired excess in red.

A 3D printed fixture was created to hold the masks within the beam at the same position that spray droplets would be observed. The image captured for the 80 µm disc is shown in Figure 32.

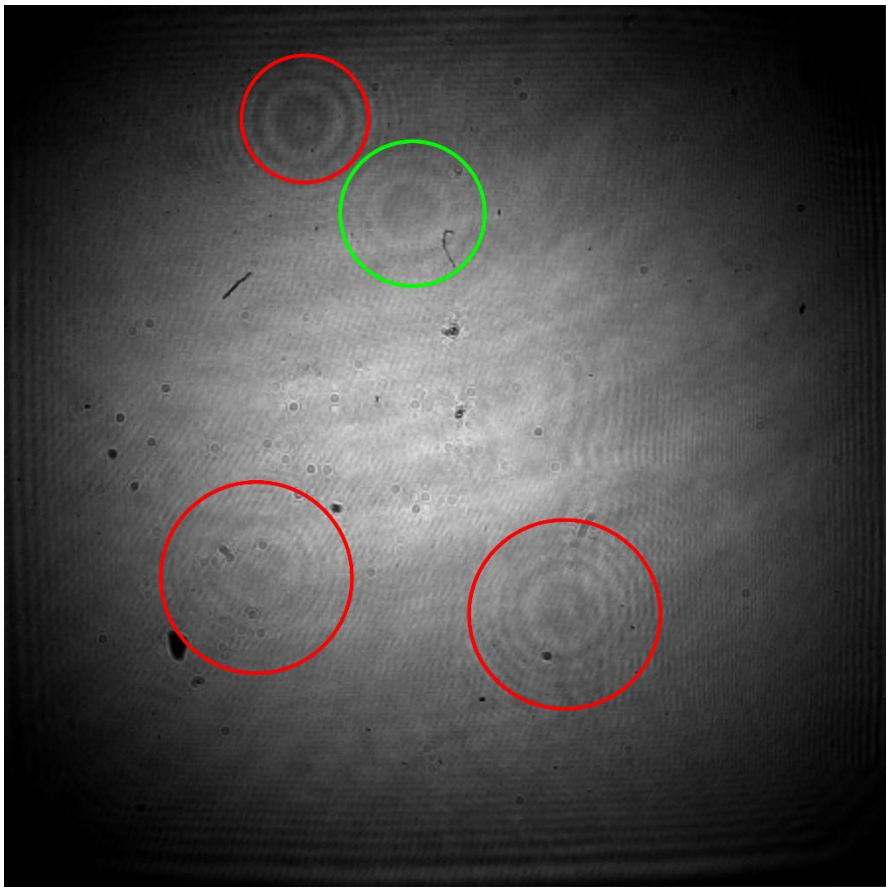

Figure 32: Greyscale converted capture of 80 µm photomask showing Airy discs resulting from light-blocking circles. Red circles highlight the undesired excess and green highlighting the desired disc as in Figure 31. One undesired spot is not visible due to low beam intensity in that region. Dark spots throughout image are due to dust on the sensor

Multiple diffraction patterns are visible, most of which are the known areas of aluminium film (from Figure 31), but some diffraction patterns are due to dust particles that could not be removed from the plates, prior to the captures. The photomasks were flushed with isopropanol prior to imaging in an effort to minimise the dust presence but not all particles could be removed and are visible in the image. Worthy of note is that even the additional non-circular areas of aluminium film present on the photomask create a circular Airy disc pattern.

This diffraction pattern is only occurring as a direct result of the light coming from a spatially coherent source. While the presence of Airy discs allows for a much larger observable disruption caused by the droplets, additional image processing is required to isolate individual droplets and determine their positions.

Droplet Path Tracking

Moving from the raw images as shown in the previous chapter, to droplet detections and droplet paths requires the use of additional appropriate image processing tools. The OpenCV library provides the necessary tools. As processing speed was not a performance consideration in this case, Python was chosen over C++ to implement OpenCV. There are two distinct objectives with droplet path tracking: droplet detection and detection-path allocation. With regards to droplet detection, a number of filtering steps are used to improve signal to noise ratio before being correlated with a known droplet-like kernel. With detection-path allocation, the paths are allocated algorithmically, using a number of expected parameters. The steps taken to achieve tracked droplets from raw images are expanded in the following sections.

1 Droplet Detection

1.1 Background subtraction

A number of the objects in frame, such as the target and any dust particles trapped on the optical flat or sensor, are time invariant or do not provide droplet information. While they do not provide any additional information that will aid in droplet detection, they do add more information to be processed and as such introduce added risk of false positives. Ideally, a background still image would be captured prior to time-variant imaging and the still image information removed. However, in this case, the target moves, and liquid accumulates on the target, both of which cause time variant image effects. A still image captured prior to time-variant imaging would not be representative of the background.

A background approximation can be generated using a moving average of the frames. With a slow average, the low frequency information can be adequately approximated while the high frequency information (droplets) will not be. A simple way to implement this is with an exponentially weighted average filter (EWMA), represented by the equation [134]:

$$dst(x,y) \leftarrow (1-\alpha) \cdot dst(x.y) + \alpha \cdot src(x,y) \tag{20}$$

Each incoming frame alters the average by a specified weighting, α which in this case was 0.5, chosen experimentally as it showed good background subtraction without loss of features of interest.. A lower weighting will decreases the speed and frequency response of the filter, with the opposite being true for a larger weighting. The frequency response for this is shown in Figure 33 for a framerate of 7200FPS.

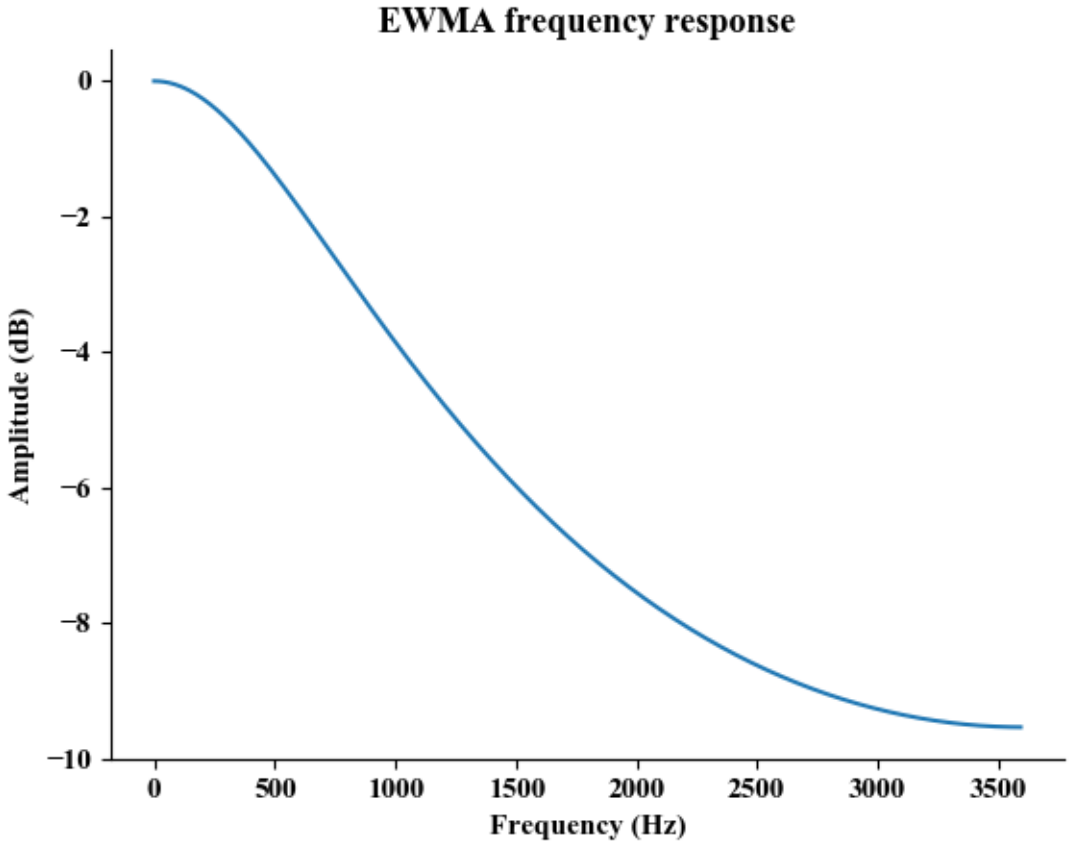

Figure 33: Frequency response for a EWMA with sigma of 0.5 at a framerate of 7200fps.

This averaged "background" is subtracted from the current frame, and the image normalised. A raw frame is shown below in Figure 34 next to a corrected frame.

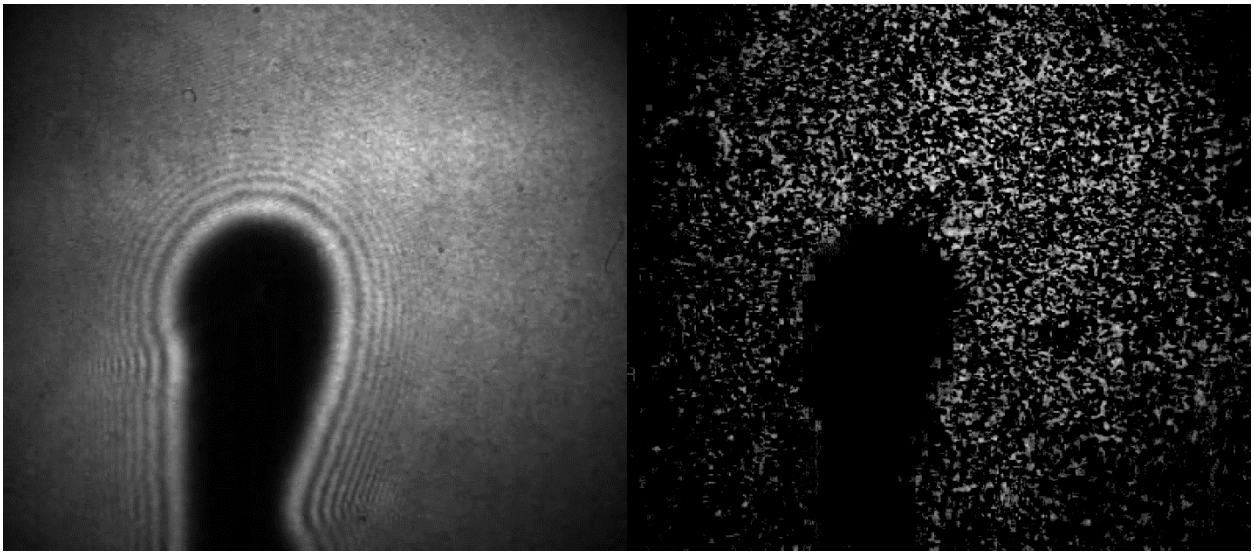

Figure 34: Raw frame (left) and background removed (right).

1.2 Noise reduction

The amount of overlapping Airy disc patterns creates a noisy image. The majority of the overlapping rings do not provide useful information as they are inseparable from the rings they intersect with. The noise they add is of high spatial frequency in comparison to the Airy disc kernels to be correlated with. A low pass filter such as a Gaussian blur will reduce the high frequency components from the image. A Gaussian blur is applied in the same manner as a normal correlation with a kernel of Gaussian distribution. In this case, the Gaussian kernel has a standard deviation of 2.7 and a size of 7x7 pixels, resulting in the kernel shown in Table 6. These values were chosen experimentally, as reducing the maximum number of false positives in the correlations without significant reduction in false negatives

Table 6: Gaussian kernel weightings with sigma of 2.7 and size 7x7 used for high frequency noise reduction.

0.00973723	0.01372051	0.0168551	0.01805171	0.0168551	0.01372051	0.00973723
0.01372051	0.01933327	0.02375015	0.02543627	0.02375015	0.01933327	0.01372051
0.0168551	0.02375015	0.02917611	0.03124743	0.02917611	0.02375015	0.0168551
0.01805171	0.02543627	0.03124743	0.03346581	0.03124743	0.02543627	0.01805171
0.0168551	0.02375015	0.02917611	0.03124743	0.02917611	0.02375015	0.0168551
0.01372051	0.01933327	0.02375015	0.02543627	0.02375015	0.01933327	0.01372051
0.00973723	0.01372051	0.0168551	0.01805171	0.0168551	0.01372051	0.00973723

The effects of the blur are shown in Figure 35. The same blur must also be applied to the kernel being correlated with.

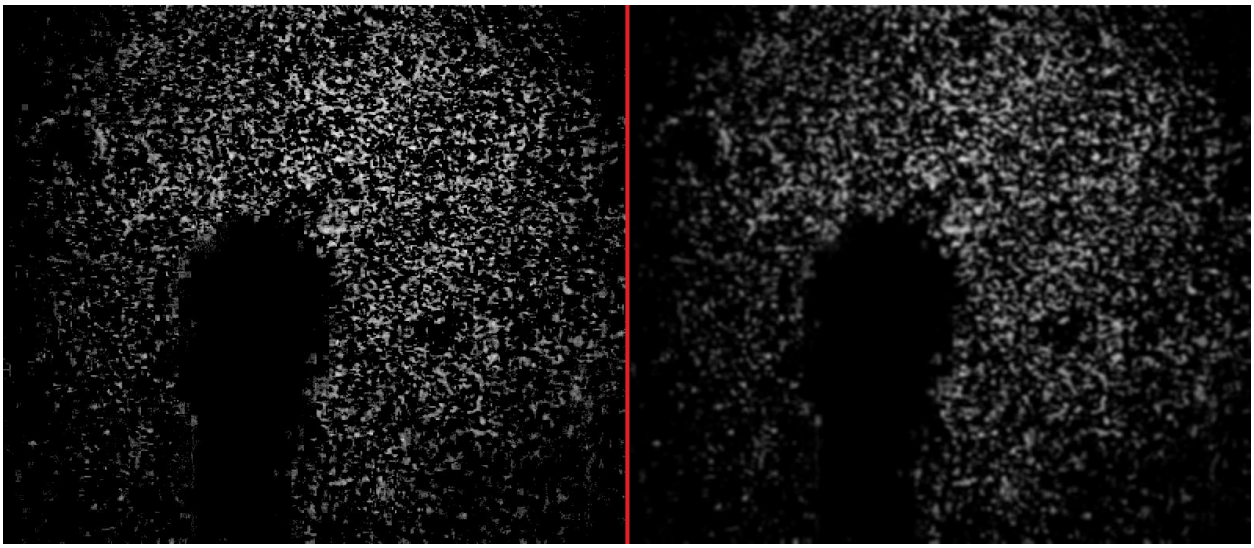

Figure 35: Background removed image (left) and with Gaussian blur applied (right).

1.3 Droplet Airy Disc Correlation

1.3.1 Kernel Generation

As discussed earlier, the diffraction patterns from the droplets are in a form similar to Airy discs. These discs can be simulated using a Fresnel (near field) or Fraunhofer (far field) approximation. Determining which approximation would best to describe the observed diffractions, is done by finding the Fresnel number (ref):

$$F = \frac{a^2}{L\lambda} \tag{21}$$

Where a is the aperture radius, L is the distance of observation from aperture, and λ is the incident wavelength. For Fresnel numbers $F > 1$, the distance between aperture and observation plane will greatly affect the resulting wavelet pattern. Here the Fresnel near-field diffraction approximation describes the expected pattern. For $F \ll 1$ the diffracted waves can be considered parallel and are less affected by the distance from the source and the Fraunhofer far-field approximation us used.

Given the laser wavelength of 635nm, aperture radius of 50 µm and observation plane distance of approximately 600mm, we have a Fresnel number of 65.6×10^{-3}. This Fresnel number is far smaller than one, meaning the Fraunhofer approximation is most valid. The approximation of irradiance pattern, given as [135]:

$$I_2(x,y) = \left(\frac{w^2}{\lambda z}\right)^2 \left[\frac{J_1\left(2\pi \frac{w}{\lambda z}\sqrt{(x^2+y^2}\right)}{\frac{w}{\lambda z}\sqrt{(x^2+y^2}}\right]^2 \tag{22}$$

Where w is the half-width of the aperture, λ is wavelength, J is the Bessel function, and z is the propagation distance.

Upon implementing in code, an important consideration is maintaining the scaling between sensor size and droplet size. When generating kernels, the frame to droplet ratio was maintained but at a much higher resolution. This was then down sampled the correct resolution of the sensor. Using the Fraunhofer approximation, the kernel as shown in Figure 36 was generated with an aperture passing light, shown in the pixel corrected size of 200x200 pixels.

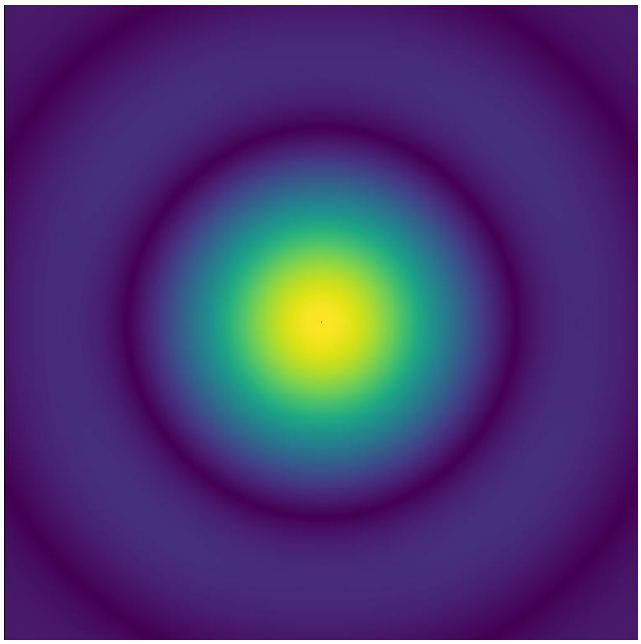

Figure 36: Droplet simulated with Fraunhofer approximation.

While it does appear these kernels have the same patterning as the observed images, the scaling when corrected does not match the observed images. The Fresnel number would indicate the diffraction should be far field; as described by the Fraunhofer approximation. Available literature only describes Fresnel numbers for laser sources without optics attached; it is likely that lens focal lengths will have an impact on Fresnel number, with the distance L possibly being a ratio of lens focal length to distance as opposed to distance from aperture. No further investigation was done into finding the cause however.

Kernels were then generated using the Fresnel approximation, given as[135]

$$U_2(x_2, y_2) = \frac{\exp(jkz)}{j\lambda z} \exp\left[j\frac{k}{2z}(x^2 + y^2)\right] \times \mathcal{F}\left\{(x, y)\exp\left[j\frac{k}{2z}(x^2 + y^2)\right]\right\} \quad (23)$$

The Fourier transform is evaluated such that:

$$f_x \to \frac{x}{\lambda z} \qquad f_y \to \frac{y}{\lambda z} \quad (24)$$

Diffraction patterns simulated with the Fresnel approximation yielded similar results to the observed patterns; however, there was an obvious inversion of maxima and minima resulting in flat correlation peaks. Simple inversion of the Airy disk gave a closer pattern, but still a poor correlation. Inverting the aperture to be a block light (point blocking) as opposed to pass light (point sourcing) provided a better correlation than simple inversion. The three diffraction pattern approximations are shown below in Figure 37. Note the difference in magnitude between rings for the inverted approximation and inverted aperture approximation.

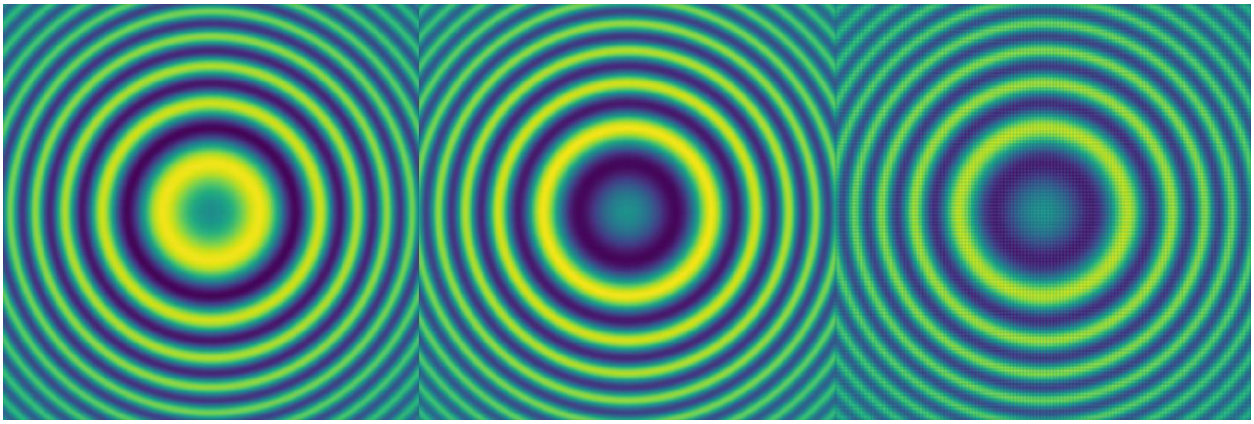

Figure 37: Fresnel approximation (left), with inversion (middle), with inverted aperture (right).

The Fraunhofer approximation was again simulated with a point block aperture, but no difference is observable in the kernel.

1.3.2 Correlation

OpenCV offers three difference template-matching operations with normalised counterparts (square difference, cross correlation and correlation coefficient methods). In practice, the correlation coefficient method and square difference method offered similar contrast between correlation peaks and background, though inverted from each other (shown in Figure 38). The simulated kernel used in this case had an 80µm aperture and was 600mm between imaging and observation planes, directly representative of the physical case. The correlation coefficient method was chosen as it resulted in positive peaks. To keep the frames bounded and for easier thresholding, the normalised method was used.

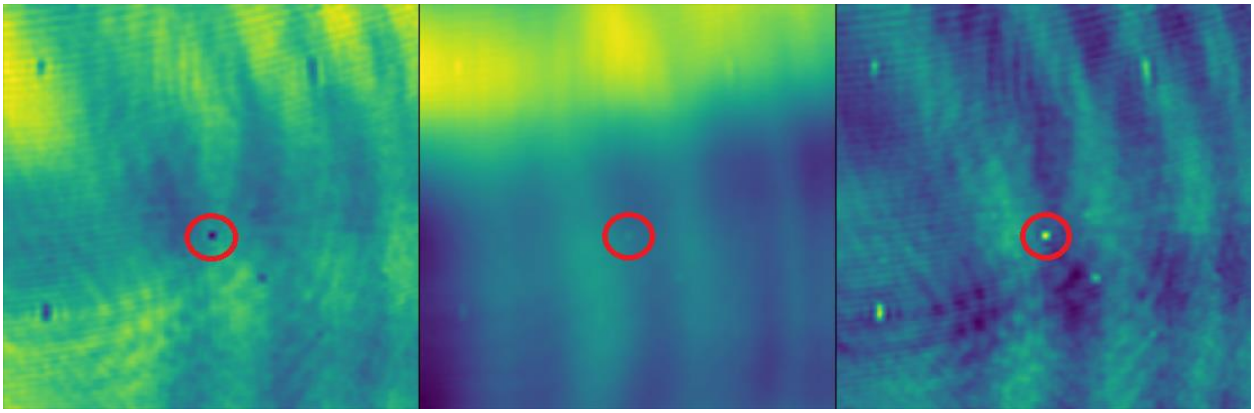

Figure 38: Square difference, cross correlation, and correlation coefficient template matching methods. Peak circled in red.

Experimentally, it was found that aperture size had a smaller influence on the resulting diffraction pattern. Alterations to aperture size at a given distance showed greater similarity than kernels with alterations in distance at a given aperture size. This does mean that depth information for each droplet could be gained by iterating through kernels for every frame and finding the strongest correlation. It may be possible to do this with droplet size also, but likely less accurate, as kernels had greater similarity between aperture steps than with observation plane to imaging plane steps. However, neither of these were tested in practice. As a result of how correlations are done, aligning the edges of the kernel to the frame, the X-Y pixel dimensions of the original capture is reduced by half the X-Y dimensions of the kernel.

1.4 Blob detection

The output from the template matching is a colour gradient map representing how similar the images are to the kernel. A peak against the rest of the image represents a strong match with the kernel. Noise and reduced sharpness of the image result in lower correlation strengths than would occur in an ideal situation with spread and flat peaks.

The simplest method to go from this heat map to detection of positions is to use a “blob” detector algorithm. The “blob” detector provided by OpenCV, simpleblobdetector, uses a border following algorithm to detect edges of thresholded “blobs”. While the implementation in OpenCV does allow filtering by value, thresholding was done outside of the function to allow for visualisations of the “blobs” being detected. Figure 39 shows the matchTemplate output alongside the thresholded and simpleblobdetector outputs.

Figure 39: Correlation (left), thresholded (middle), blob detector (right).

2 Droplet-Path Assignment

The blob detector provided the correlation centres, but detections alone do not provide information on droplet trajectory. These detections need assignment to the droplet paths to which they belong. A simplified flow diagram of how droplet assignment is handled is shown in Figure 40.

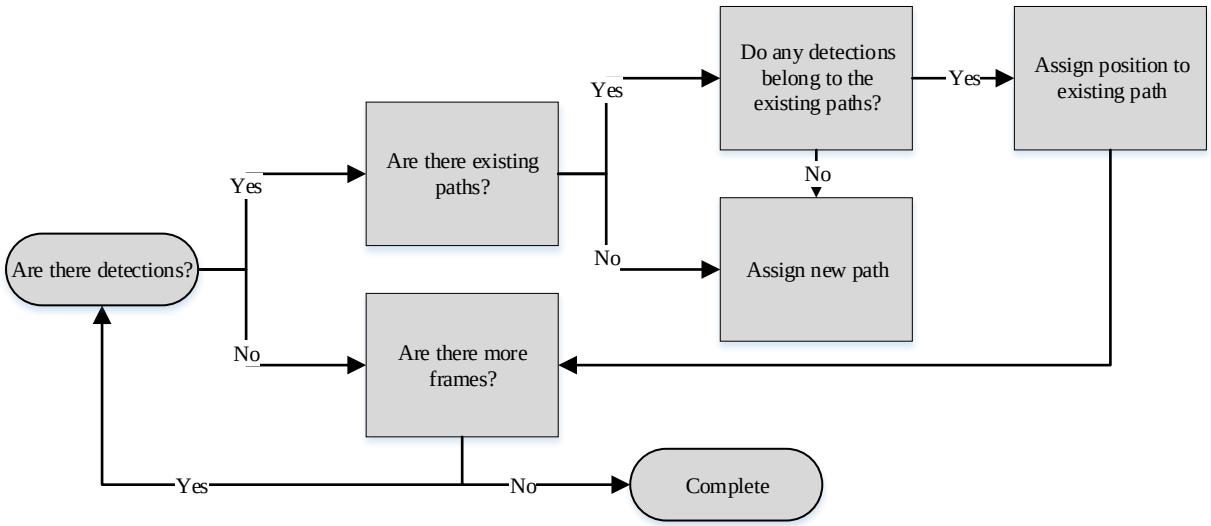

Figure 40: Simplified flow diagram of droplet assignment.

On the surface, this sounds like a simple problem, but as there is still noise present, detections are not consistent meaning a droplet can go undetected for several frames, and droplets often run close to parallel or cross paths. Answering the question of "Do any detections belong to existing paths?" requires three smaller problems to be solved: estimating the next position of the droplet, finding the detection with the highest probability of belonging to the path, and handling the case where a droplet can go undetected for several frames.

Estimating the next position of the droplet requires the use of a motion model. A linear Kalman filter offers a simple approach to characterising the motion model that is computationally cheap while also providing reasonable accuracy in estimates. As the Kalman filter used only considers position and velocity, at least two positions are required to be known, or a good initial estimate of velocity. Droplets can enter the frame on a number of trajectories, so the best approach here is to use two detections. A rough guess is required in assigning a second detection to the droplet path. In practice, this is done by assigning the closest detection within a radius of 30 pixels in the next frame. Incorrect guesses can stem from this and if the droplet goes undetected for its second frame it is lost. However, this has not had significant impacts on the effectiveness of droplet path tracking.

With the estimates of the droplet paths, the next problem is assigning detections to them. This is done by finding the cost of each detection to the estimate: the lower the cost, the higher the probability of being correct. Two parameters define the cost; distance between estimate and detection, and angle from previous detection to the estimate and detection. The function that calculates cost of a droplet assignment is defined as:

$$C(\underline{\hat{x}}, \underline{x}_{det}) = \left|\underline{\hat{x}} - \underline{x}_{det}\right| + \alpha\theta \tag{25}$$

Where:

$$\theta = \frac{(\underline{x}_{det} - \underline{x}_{n-1})}{\left|\underline{x}_{det} - \underline{x}_{n-1}\right|} \cdot \frac{(\underline{\hat{x}} - \underline{x}_{n-1})}{\left|\underline{\hat{x}} - \underline{x}_{n-1}\right|} \tag{26}$$

And $\underline{\hat{x}}$ is predicted next position, $\underline{x}_{det}$ is a given detection, $\underline{x}_{n-1}$ is the previous known position, and α is some scaling constant.

In the practical case, alpha was 0.5, giving half as much importance compared to velocity. Defining cost in this way, measuring distance from estimate to detection relies on valid droplet positional estimates from the motion model of the Kalman filter. As cost is a product of both velocity and angle, the minimum radius of curvature that can be tracked is dependent on the frame-to-frame delta of both, as long as no detections are found closer to the estimate than the actual droplet.

With this equation of cost, a matrix is created with each of the columns representing paths and each of the rows representing detections. The values representing the cost between respective paths and detections. With a matrix defining cost between each path and detection, the matrix must now be reduced to find the cheapest pairing between a path and droplet. For this, the Hungarian method was implemented [106]. This method is computationally simple and provides the lowest cost element for each row and column. With indexes to these values within the cost matrix, the cost can be thresholded. As the position of the cost is known, the detection can be assigned to the path it belongs to.

Every detection that goes unassigned is checked against the edge criteria to start a new path. The images are noisy and as such, there are instances where a droplet path may not have a detection that belongs to it for a number of frames. It would not be very robust to exclude a method of handling such a case. In this situation, the motion model is relied on, and the estimates propagated forward while bounding maximum velocity to 40, as previously found. The estimates act in place of valid detections, but are stored separately. If this list grows over a length of ten, the path is considered lost and deleted. A path with enough valid detections is be stored for later analysis. If a valid detection is found after propagating estimates, the estimates are considered true and are added to the list of valid detections. If there are no existing paths, detections are checked for their position in the observable frame. If close enough to the leading edges, then a new instance of path is created for them. The flow diagram expanding on detection assignment is shown below in Figure 41.

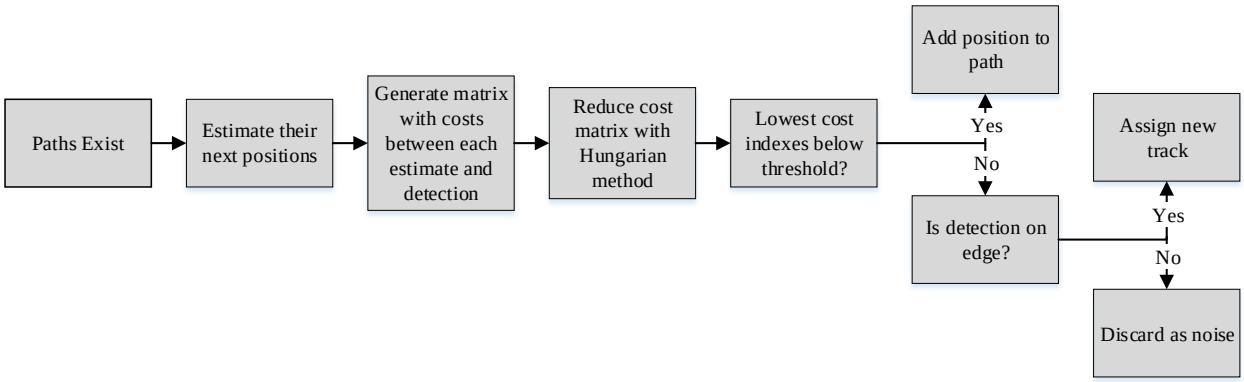

Figure 41: Flow diagram expanding on detection assignment.

An important shortfall to note is that with the laser light source used the imaging plane is not planar but a volume between the source and sensor. All imaging is therefore two-dimensional as there is no measure of depth. As mentioned in 6.1.3.2, it may be possible to extract depth data, but this was not investigated here.

An example of the path progression of multiple tracked droplets is shown in Figure 42. The excess detections shown either are the result of noise, or belong to droplet paths that did not meet the criteria to be tracked. The outer red box represents the edge of the detectable zone (reduction due to correlation) and the inner box represents the boundary to initialise as a new path. Airflow direction is right to left. The green point at the end of the path is the current droplet detection being tracked and allocated to the path.

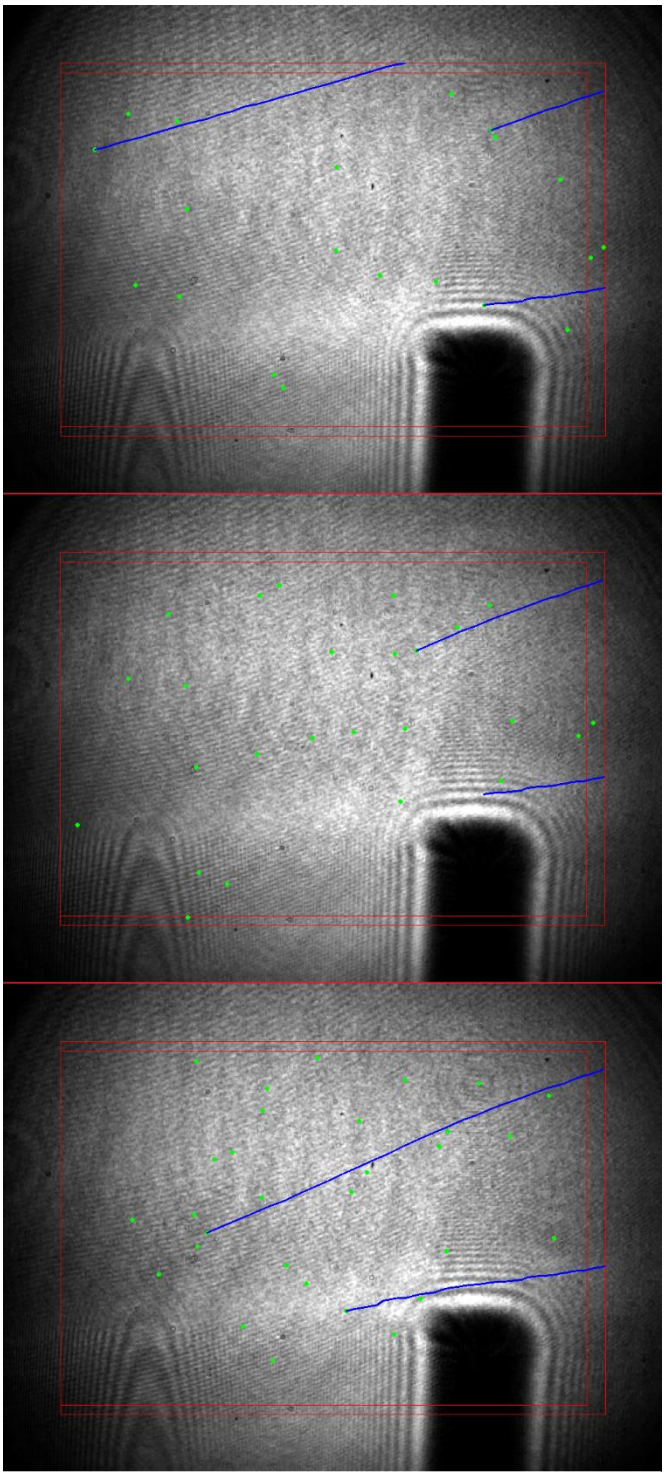

Figure 42: Progression of droplet path. Note that the bottom path in the second frame has a missed detection (no green point at end) and is found in the third frame using propagated estimates.

Three further examples of randomly selected tracked droplet paths are shown in Figure 43 to demonstrate correct assignment of multiple intersecting paths as well as tight curvatures in droplet path.

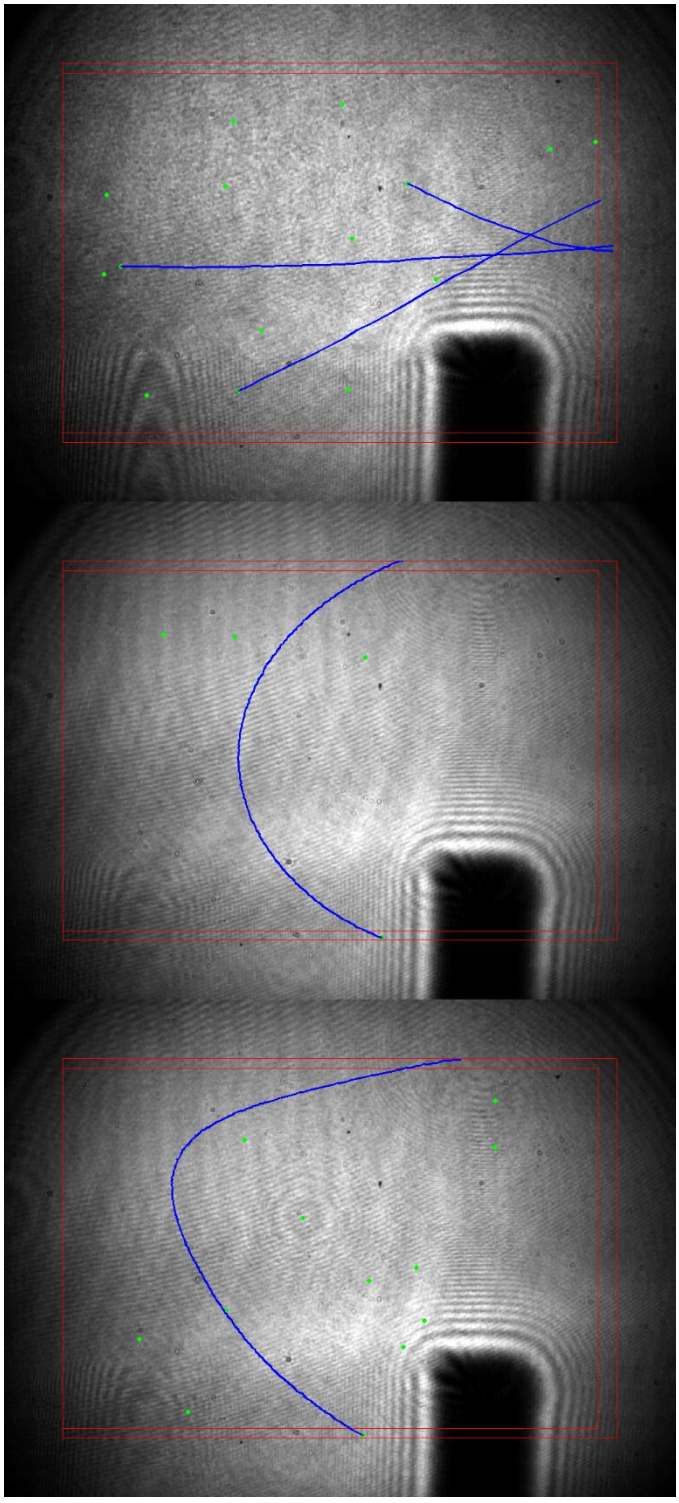

Figure 43: Series of frames from different captures overlaid with detections (green) and paths (blue). Note the correct assignment of multiple intersecting paths and values of curvature have been correctly tracked.

Analysis of Droplet Data and Results

As identified in chapter 5, the conducted experiments are;

1. Effect of target impedance on charge retention.

This test aims to measure if charge retention will occur/have an effect on the interaction between droplets and the target for a spray period of less than one second. The extreme cases will be tested first, low impedance earthed and open circuit. If there is an observable difference in droplet-target interaction, impedances within the range found on a potted grapevine (1 MΩ) will be tested in stepped values after high-speed footage can be analysed.

2. Nozzle voltage relationship with droplet-target interactions.

This test aims to measure the relationship between the magnitude of droplet-target interaction and the nozzle voltage.

3. Variation of droplet-target interaction within spray cone.

This test is to investigate if there is variation of the wrap around effect within the spray cone due to variation of charge distribution within the spray cone and to measure if the effect decays at increased distances from the nozzle.

This chapter covers the analysis of the data captured from the above experiments.

Limitations of testing and observational methods

There are limitations to the test methodology that must be understood when viewing the results. The droplets are moving in three-dimensional space, however only two dimensions are captured here. While measures were taken in the test configurations, droplet movement in the unobserved horizontal dimension are possible and will not be properly captured during analysis. Additionally, a droplet moving toward the target already and slowing due to aerodynamic effects will have a negative acceleration.

There may be some bias in the droplets that the algorithm has detected based on the correlation kernel used and the Kalman filters motion model. Without further analysis of the raw footage, it is impossible to know what these biases are and their effect on the outcome.

Droplet size and charge magnitude are a distribution requiring a statistical model to characterize. The analysis here does not create such a model and as such cannot characterize motion.

Removal of low quality droplet paths

Applying the tracking algorithm to 85 captured high speed videos resulted in 15,425 tracked paths. However, not all of the allocations in the tracked paths are correct and not all of the droplet paths intersect with the frame in a way that provides useful data on droplet interaction with the target. Figure 44 shows a plot of one such track with a bad allocation. Bad allocations are characterised by a sudden change in droplet velocity magnitude or direction. Figure 45 shows an example of a track that does not provide information about the droplets interaction with the target. These tracking data that were of no practical use were manually inspected and removed.

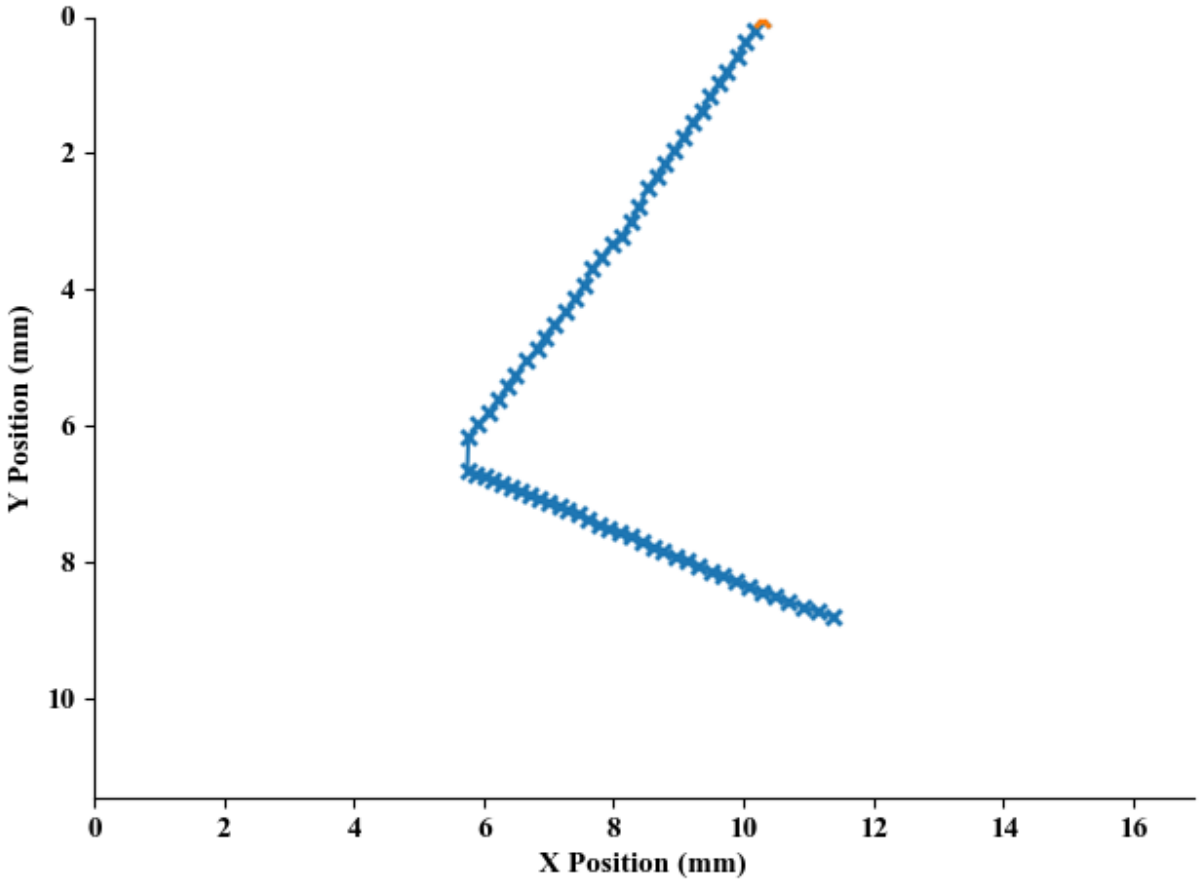

Figure 44: Example plot of droplet track with obvious change of direction and velocity due to incorrect position allocation. Orange cross represents start position of track. Blue crosses represent allocated positions.

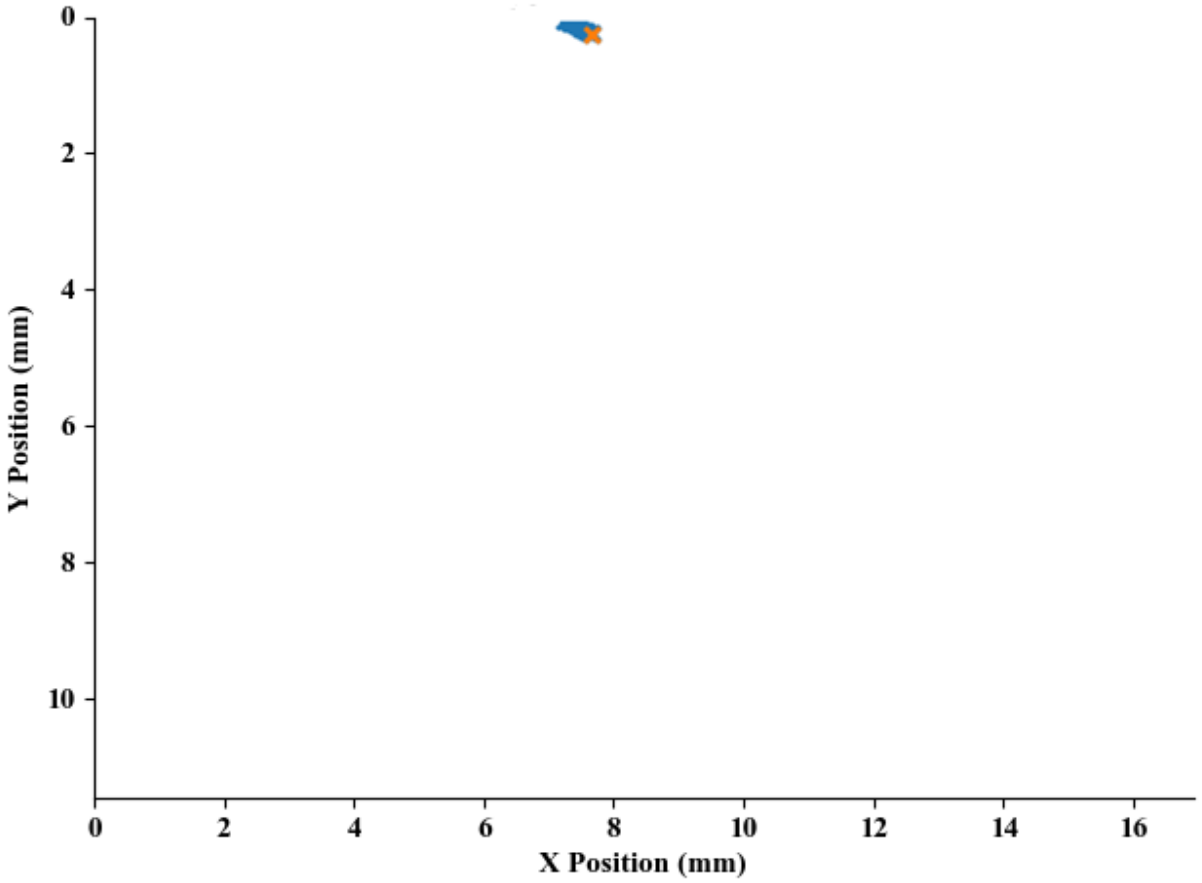

Figure 45: Example of droplet track removed as being too short to show interaction with target.

Pre-processing of the Data

Determining the interaction between target and spray droplets relies on velocity and acceleration data for the droplets paths. The Python library Numpy provides functions that generate this data for discrete time values such as that provided by the droplet tracking. The positional data however still contains a lot of high frequency noise, and acceleration values gained by taking the double derivative are not representative of the accelerations a droplet would experience.

When removing the high frequency noise, considerations must be made to preserve the integrity of the desired data. Too much filtering and the data is no longer representative of the droplets movements, too little smoothing and the velocity and acceleration values for the path are only representative of the noise. The frequency of this noise occurs at the sampling frequency 1/framerate, due to the way droplet centres are identified through correlation and blob detection. Noise in the raw image impacts correlation strength frame to frame, resulting in a differently shaped blob when thresholded. The blob detector then finds mass centres for the blobs that do not perfectly align with the physical droplet position, resulting in noisy frame to frame movements.

With limitations of excessive smoothing in mind, a reasonable method of removing this noise was to smooth the raw data with a small averaging filter, interpolate the data, and then more aggressively smooth the interpolated data with another averaging filter. In this case, smoothing used a three tap averaging filter for the first pass, five times up-sampling with linear interpolation, and a 20 tap averaging filter for the second pass. Due to the way averaging

filters work, the start and end values of quantity sampling window-1 have invalid values so must be removed. This process does reduce the number of viable samples and usable track length. The x and y positional data are independent and so interpolated values are calculated on each axis independently with linear interpolation.

For taking the derivative, the Numpy gradient function is used. The function numerically calculates the discrete derivative of the input array using central difference for the data points, given by:

$$\Delta f(x) = f(x+1) - f(x-1) \tag{27}$$

However, this cannot be calculated for the start and end data points, so the forward difference and backward differences are instead calculated as identified by:

$$\Delta f(x) = f(x+1) - f(x) \text{ and } \Delta f(x) = f(x) - f(x-1) \tag{28}$$

The end values are only representative of a half step of x but are placed at the end positions of x. Because of this, the end values where discarded after the first derivative and second derivative steps as they would result in higher than actual velocity and especially acceleration values. The results of this smoothing and trimming process is shown in Figure 46 with the droplet entering from right. The original track (dashed yellow line) extends beyond the smoothed track (solid blue line) due to trimming. Also, due to the position of the target in the viewing field, very few droplets were tracked wrapping around and impacting the back side of the target. Droplets were captured impacting the front side of the target but showed no interaction with the target as there was no trajectory change while in viewing field, so were excluded from the analysis.

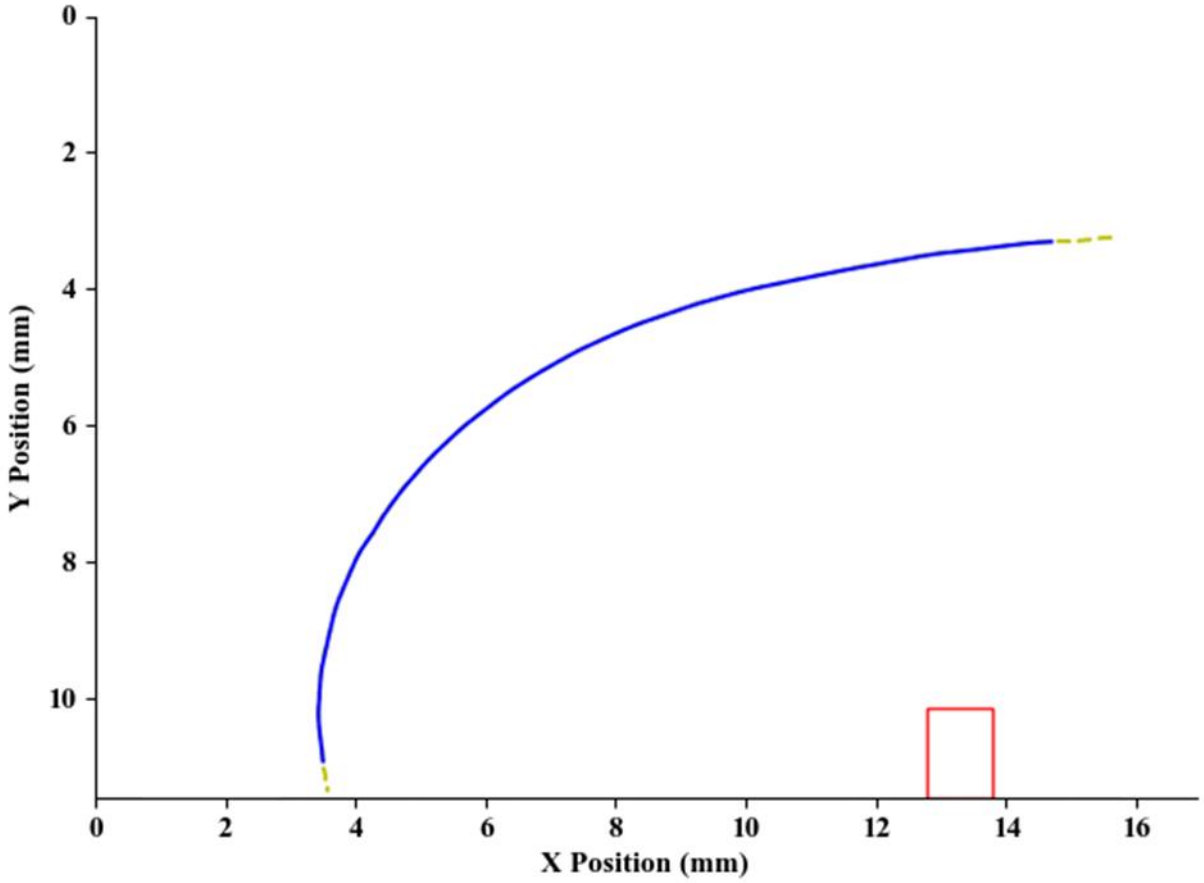

Figure 46: Original track shown in dashed yellow, processed track after smoothing and interpolation shown in blue. Droplet enters observational field from right.

It then needs to be determined whether the acceleration vector is towards the target or not. To obtain this information, the closest point on the target to the droplet position needs to be determined. Breaking the areas around the target up into small sections can facilitate a simple analytical answer. The area around the target can be broken up into sections, shown in Figure 47, with the closest point defined.

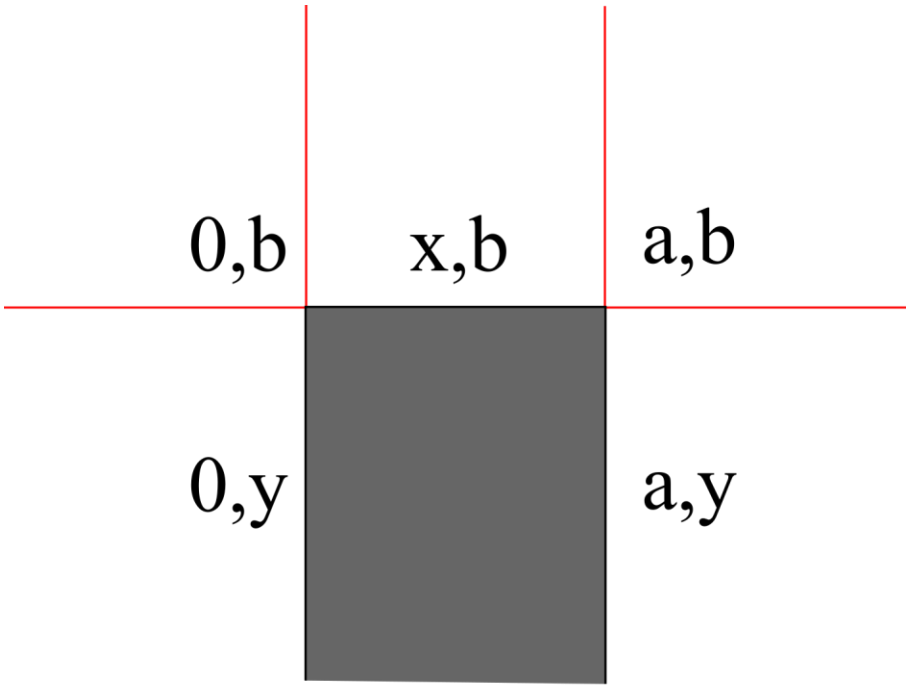

Figure 47: If the bottom left point is described as (0,0), the width defined as (a) and height as (b), the area around the target can be segmented as indicated with the red lines. The point on the target closest to the droplet's position is then described by the values in the sections.

With the vector describing the droplet position and the closest corresponding point on the target defined, the dot product can be taken with the acceleration vector at that droplet position. If the value is positive, the acceleration can be said to be in the direction of the target. As such, the component of acceleration toward the target is found.

Test 1: Effect of target impedance on charge retention.

The objective of this test was to determine if an open or high impedance path to earth would have any impact on charge retention and target-droplet interaction over a spray period of one second. Images were taken with no charge, the target grounded through low impedance, grounded through a series 1MΩ resistance, and ungrounded, all with a fixed nozzle voltage of 4kV. Originally, these were normalized for distance from target squared, as Coulombs law would suggest would be appropriate. However, this did not linearize the accelerations, indicating environmental forces play a significant role in droplet movements. The accelerations were instead averaged across the entire droplet's movement and plotted at the middle point of time they were observed. The result is shown in Figure 48, with means and standard deviations shown in Figure 49.

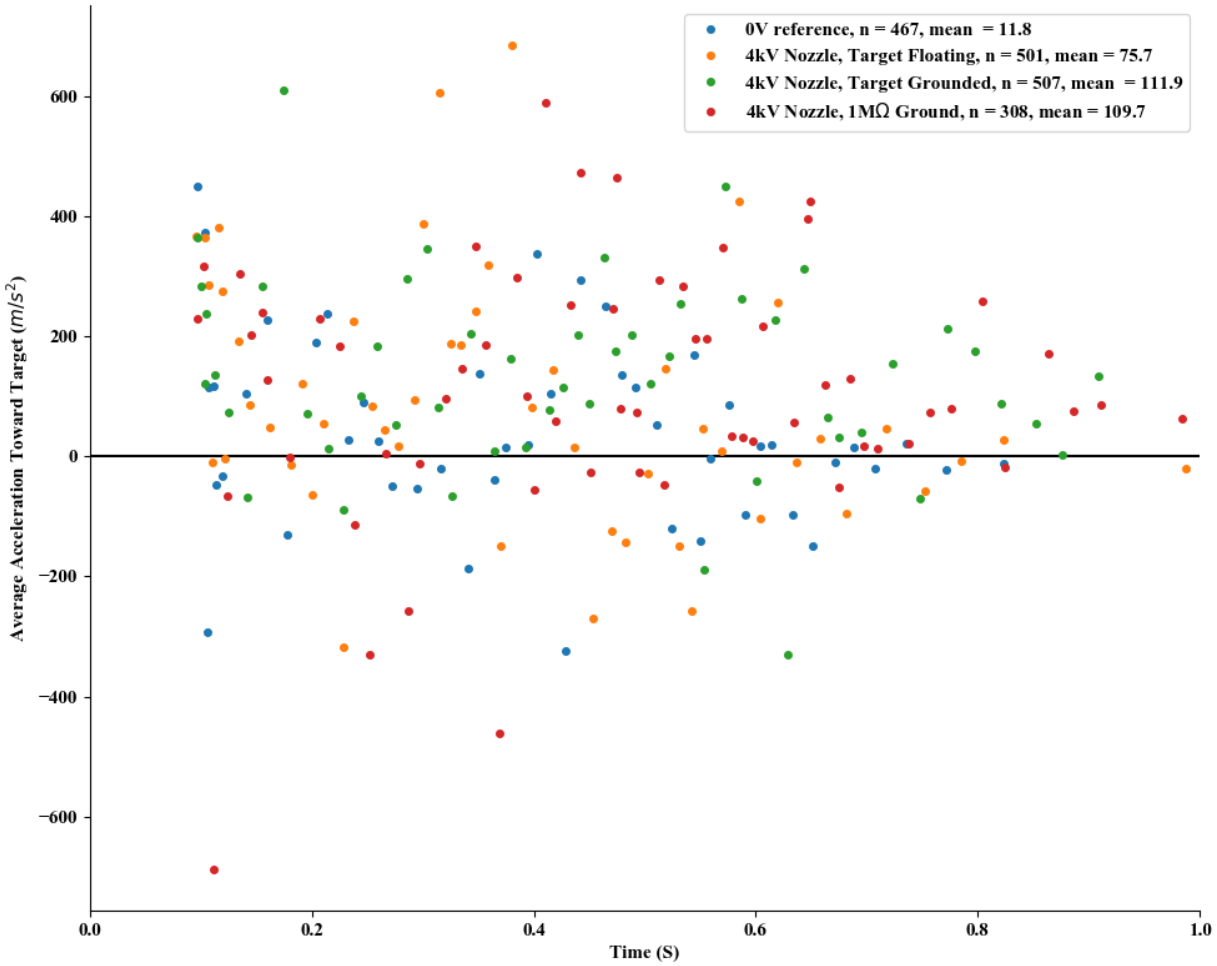

Figure 48: Average acceleration of droplet path toward the target plotted at the time they were observed. Note that while many droplets were tracked, only a small sample of all droplets were plotted for clarity.

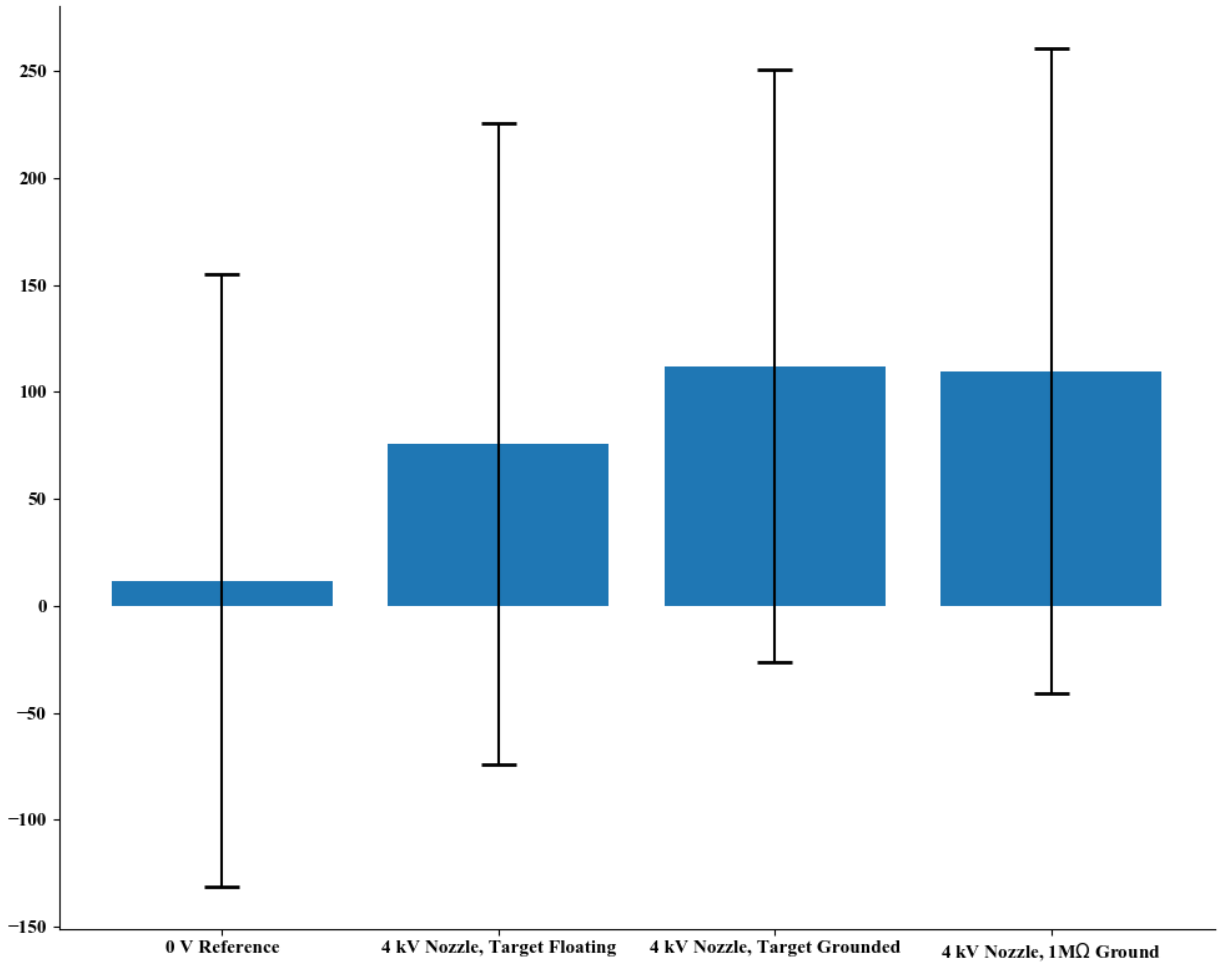

Figure 49: Mean acceleration toward target for each test condition, with error bars representing ± one standard deviation overlaid

The uncharged spray case shows a near zero value for mean accelerations toward the target as would be expected with no added attractive forces. All test cases with charged spray show mean accelerations in the direction of the target, with no significant difference between the low impedance and 1 MΩ grounded conditions. The floating plate condition does show a slightly lower mean value of accelerations toward the target indicating that with a longer spraying period, sufficient charge may build up to impact efficacy of droplet deposition. This could also pose an issue with more complex impedance networks as may be present in larger plants with many shared junctions (areas of large impedance contribution identified in Chapter 3) in the ground path. Further characterization of plant tissues and impedance network as well as charge transfer to the plant from the spray would be necessary. Droplet accelerations do show decay over time, in both positive and negative value for all spray conditions. This does suggest some steady state condition that is not reached within the spray period of one second.

Test 2: Nozzle voltage relationship with droplet-target interactions.

This test aimed to measure effect of nozzle voltage on droplet-target interactions influenced by electrostatic force. The target (grounded through a low impedance path) was sprayed at a distance of 600 mm from the nozzle at the spray cone center with nozzle voltages between 2000 V to 4500 V in steps of 500 V.

The droplet acceleration toward the target were plotted versus droplet distance from the target. Four random samples of this from the 2500 V test are shown below in Figure 50. The second line along the x-axis is from the droplet passing its closest distance toward the target along its path and getting further away. While the average acceleration is positive, it is again evident there is no strong relationship. This trend is the same for all charged conditions. The cause of the highly oscillating accelerations is likely due to environmental factors such as turbulence.

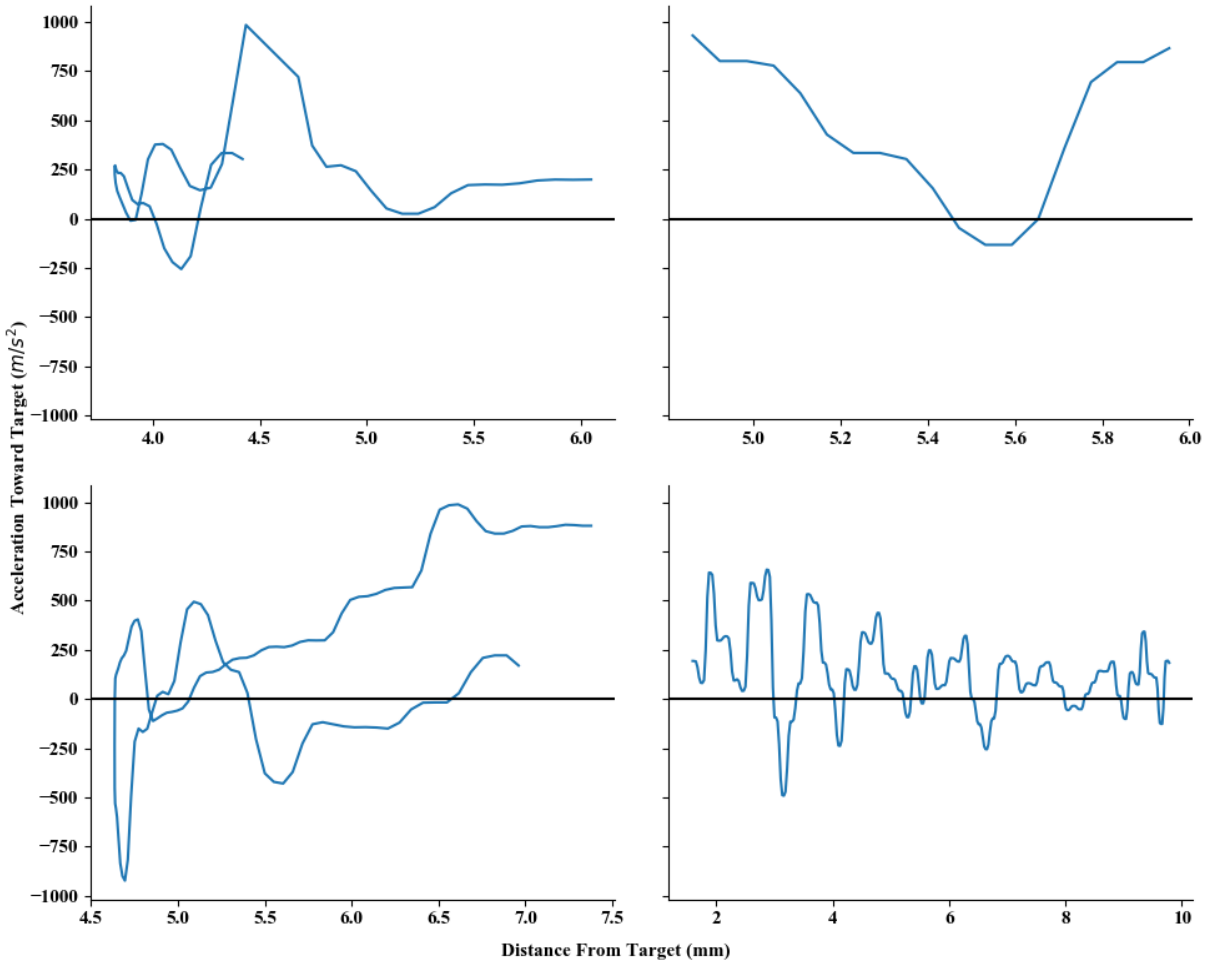

Figure 50: Droplet acceleration towards target plotted versus distance of droplet for 2500 V test. Four samples were represented at random from list of all 2500 V samples. Second line along the x-axis is from the droplet passing its closest distance toward the target along its path and getting further away..

While the aim of this test was to show a relationship between nozzle voltage and the distance from the target the droplet can be seen to be influenced by electrostatic force, no conclusive relationship can be shown. The distribution of droplet size and droplet charge and hence charge to mass ratio, mean interactions require a statistical model to characterize the effect. A model would also be required to account for aerodynamic effects.

Without making a complex model of the system, average observations of the system can be made from the data. Viewing the average acceleration of a droplet at its midpoint time as in test 1 gives Figure 51.

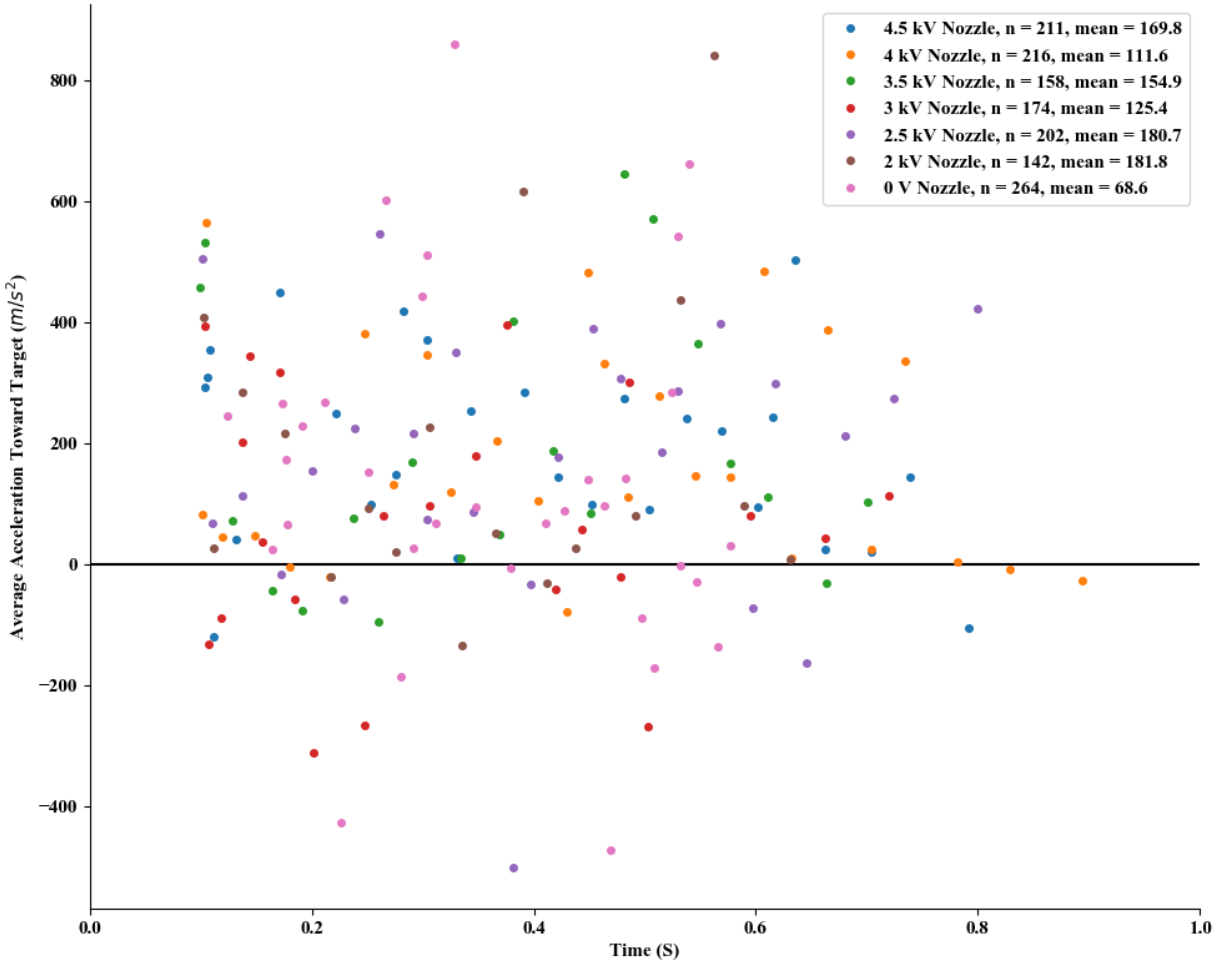

Figure 51: Sample of droplet accelerations versus time for 0 V and voltage steps between 2000 V and 450 0V. Mean acceleration for each voltage step is also shown.

Viewing just the mean acceleration versus voltage gives Figure 52.

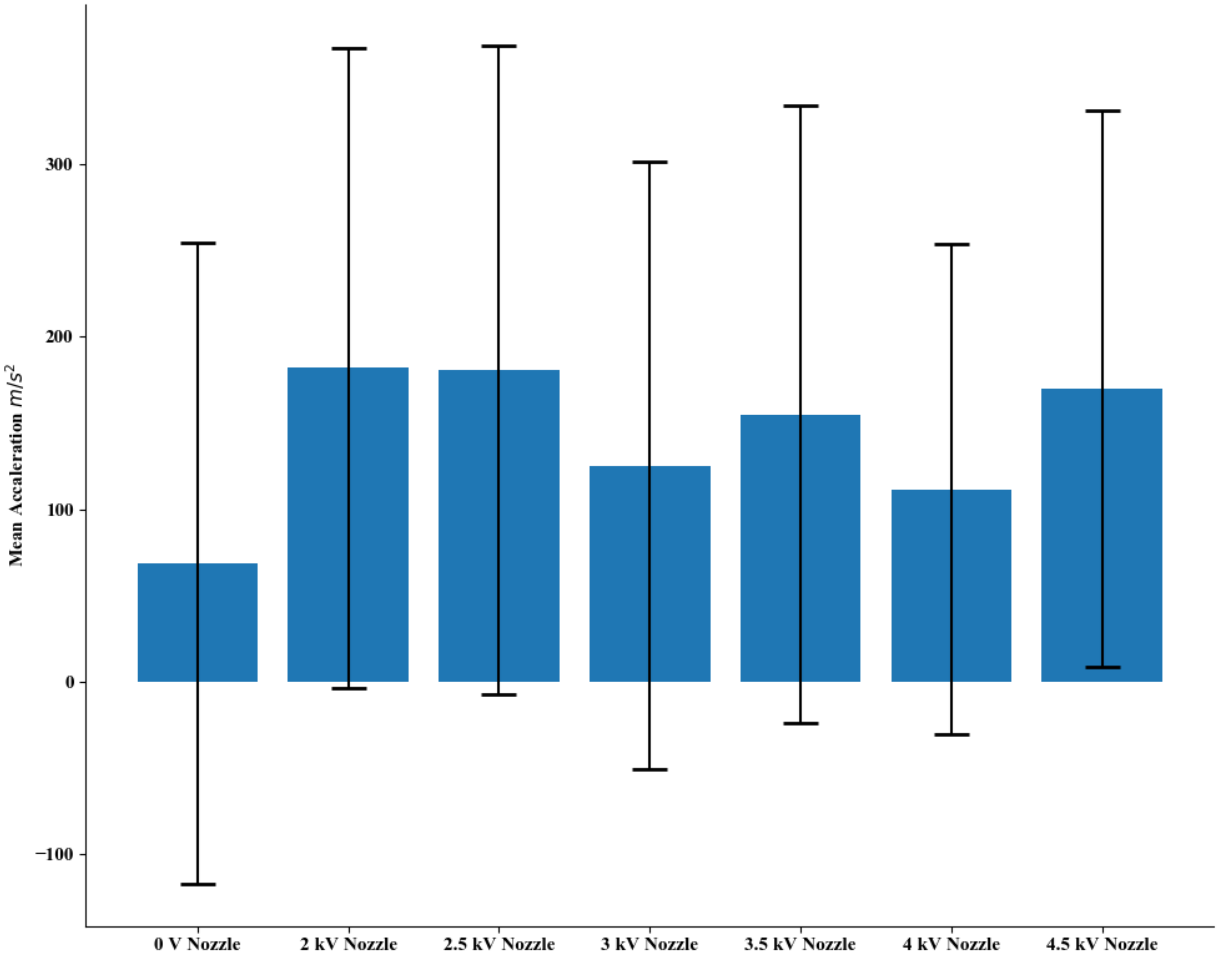

Figure 52: Mean voltage versus acceleration toward target with error bars representing ± one standard deviation overlaid

Mean acceleration for charged sprays are notably higher than uncharged in the direction of the target, however with significant overlap in standard deviation. This does still show a trend of increase attraction with charged sprays in comparison to uncharged. The lower voltage of 2000 V shows the largest mean attractive acceleration, with fluctuations through the voltage steps. This is however not completely representative of the droplet target interactions. Viewing droplet paths shows a greater number of large accelerations at the higher voltages, but occurring less consistently than at the lower voltages. Space charge and mutual repulsion may be having a negative impact at this distance for the higher voltages resulting in higher charge-to-mass ratio droplets being dispersed into the surrounding environment and lower charged droplets interacting with the target. This would suggest an upper voltage limit for a given nozzle design, with a flattening then decreasing curve as voltage goes beyond the upper limit.

The uncharged spray having a small positive mean acceleration toward the target is expected. Because of airflow from the nozzle, a low-pressure area will form behind the target on the far side, in a manner similar to a gurney flap [136]. This in combination with gravity forces allows for more opportunity for droplets to be pulled toward this low-pressure zone resulting in an acceleration toward the target.

Test 3: Variation of droplet-target interaction within spray cone.

A non-uniform charge distribution through the spray cloud is to be expected, with contributions from the nozzle geometry as well as space charge effects after the spray has left the nozzle. This will result in differing interactions with the target, dependent on its position within the spray cone. Test three aims to identify the difference in interactions. The target was stepped in distances between 600 mm and 1200 mm from the nozzle in 200 mm steps. At each step, images were captured at the center of the spray cone as well as the upper and lower edge. The spray cone is approximately 20 degrees at no charge, so the upper and lower edges are defined as ±10 degrees. The nozzle voltage was kept constant at 4000 V.

Each distance step was plotted giving Figure 53, Figure 54, Figure 55, and Figure 56.

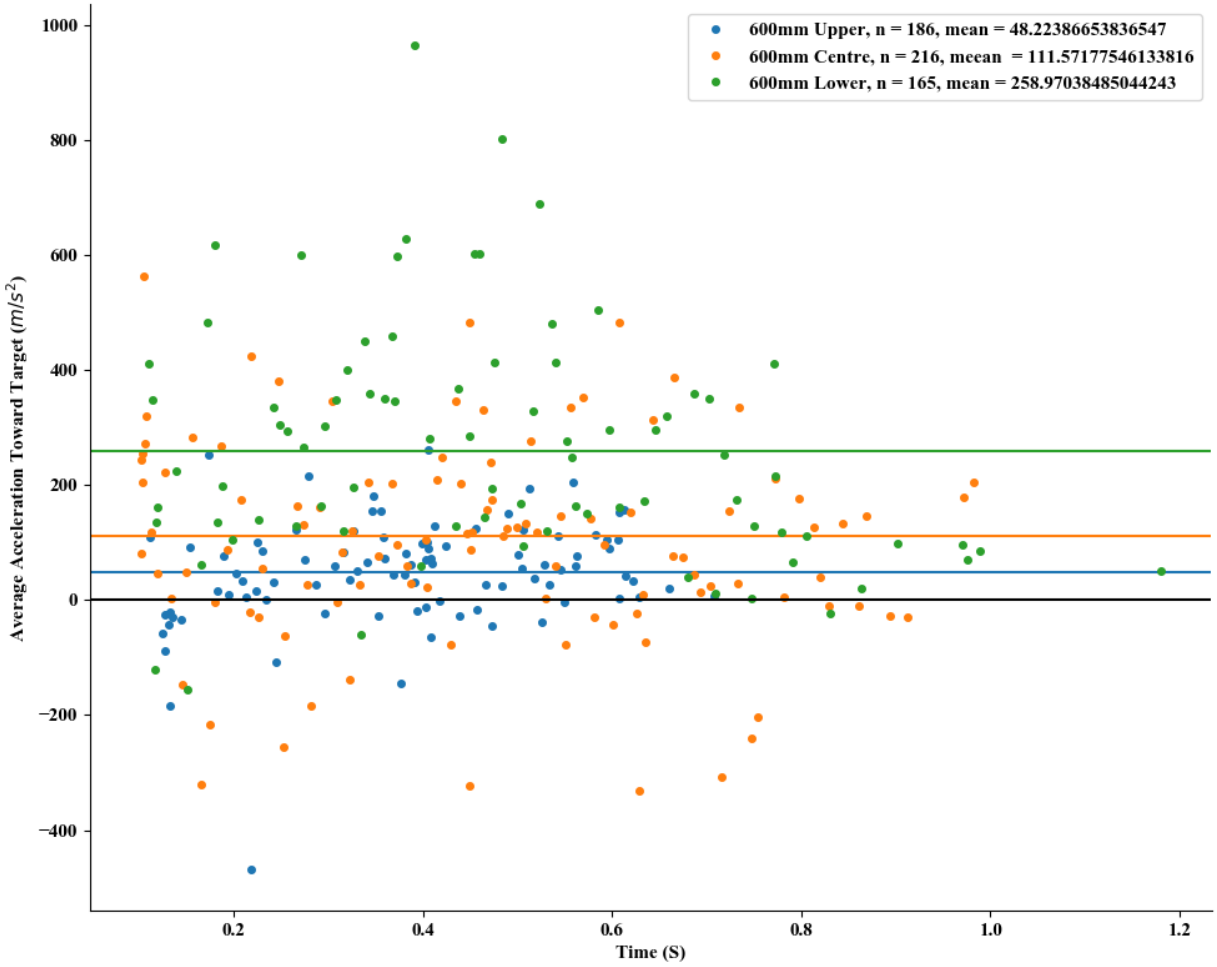

Figure 53: Accelerations versus time for upper, centre, and lower spray cone positions at 600 mm from nozzle.

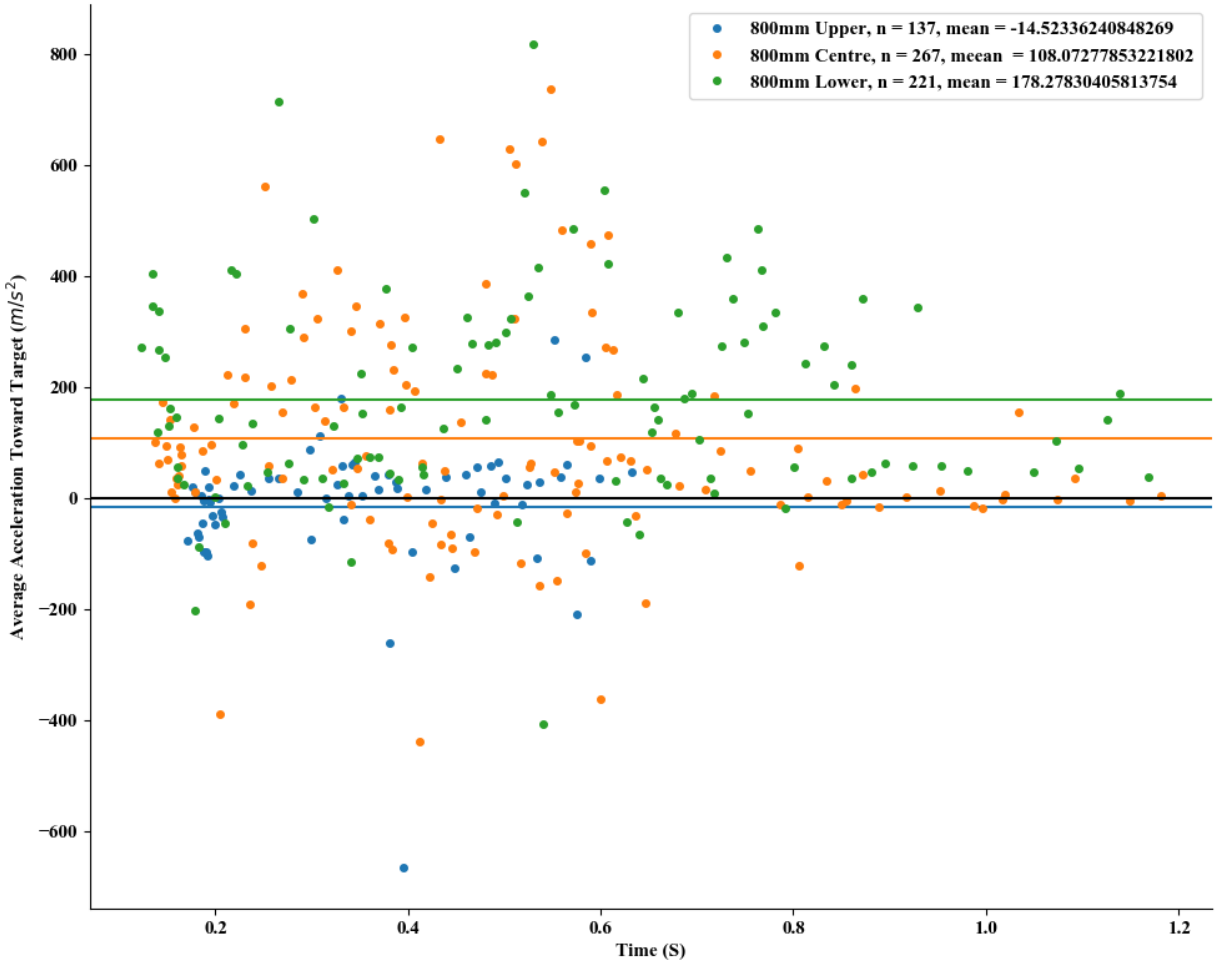

Figure 54: Accelerations versus time for upper, centre, and lower spray cone positions at 800 mm from nozzle.

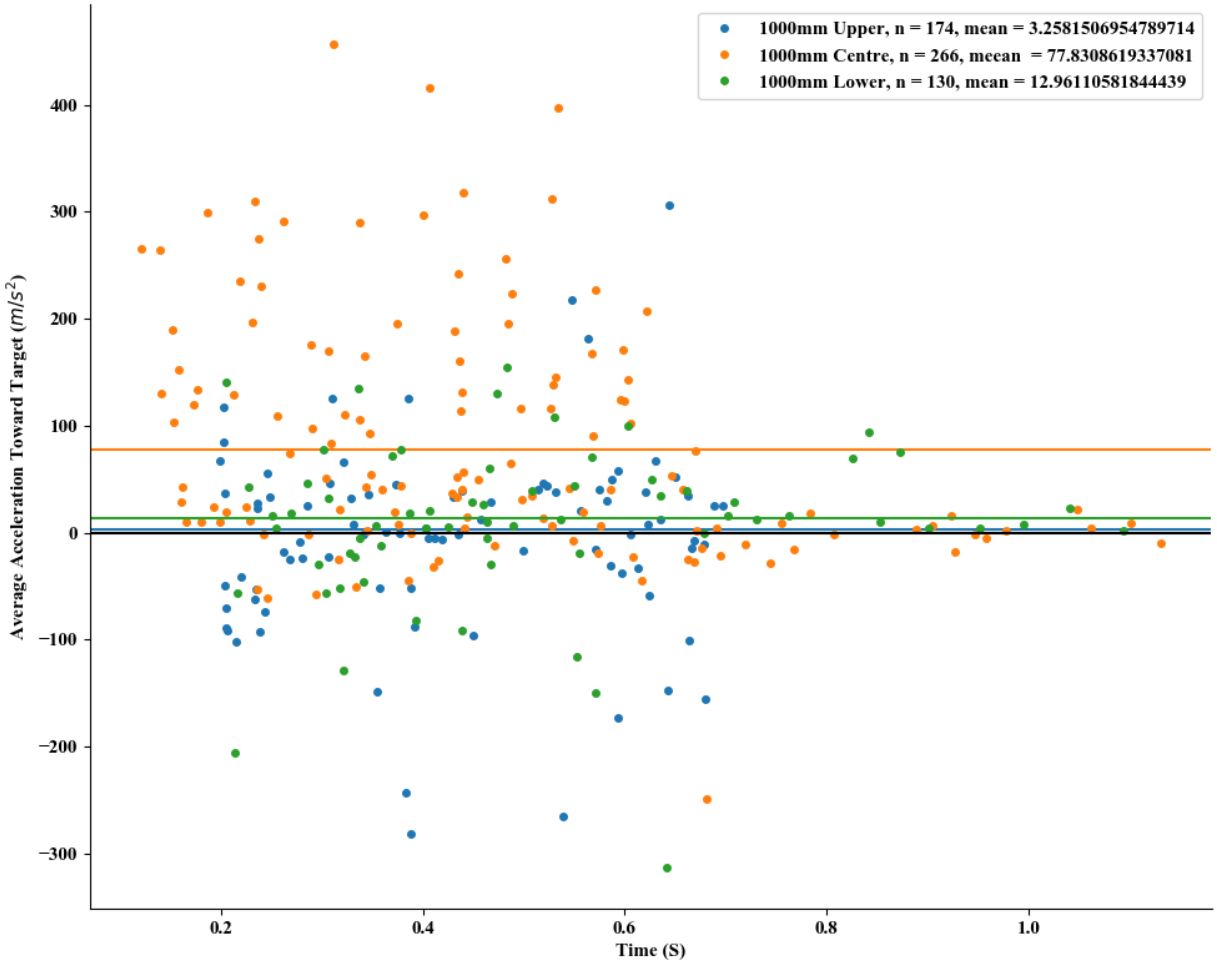

Figure 55: Accelerations versus time for upper, centre, and lower spray cone positions at 1000 mm from nozzle.

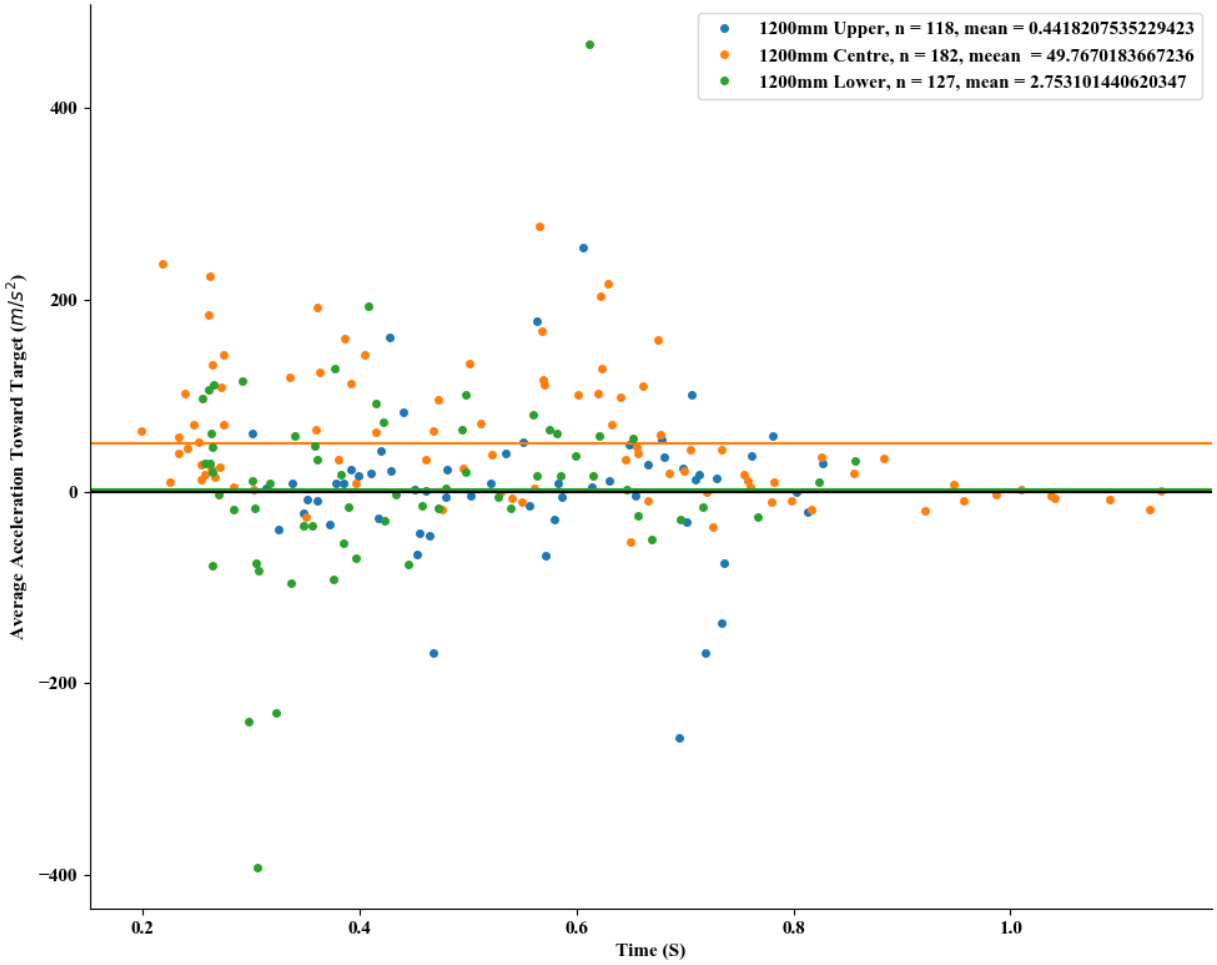

Figure 56: Accelerations versus time for upper, centre, and lower spray cone positions at 1200 mm from nozzle.

At distances 600 mm and 800 mm, the lower position in the spray cone has much greater average acceleration than the center and upper positions. However, above 800 mm the center position has the greater average acceleration, with the accelerations at the edges becoming negligible. The acceleration values reduced significantly as distance increases for all cases. The droplets at the upper edge of the spray cone show some ability to overcome gravity, indicating Coulombic forces are greater than gravity forces here, though the average acceleration is lower than other positions. This may gain be indicative of space charge effects causing droplets of higher charge to mass ratio to be dispersed before reaching the target at larger distances from the nozzle indicating nozzle distance plays an important factor in deposition. Droplets near the center of the spray cone while still have decreased attraction at distance, are more difficult to disperse and so retain attractive forces for greater distances.

Overall, these interactions are as expected, showing attraction to the target when the spray is charged. Test 1 showed that at normal plant impedances for a single target, charge retention may is no issue. However when floating or a larger impedance network as presented in a real plant, charge retention may become an issue at longer spray periods. The results from test 2 indicate that while spraying at increasing voltages had the similar average accelerations, the behavior of the spray changed. At higher nozzle voltages, larger accelerations are seen, however occurring less consistently than at the lower nozzle voltages. This could be due to space charge and mutual repulsion effects causing droplets of higher charge-to-mass ratio to be dispersed before reaching the target. This is suggestive of an upper voltage limit before spray deposition efficacy decreases. Test 3 shows that Coulombic forces are greater than

gravity forces for charged droplets, and an inverse relationship between nozzle distance from target and magnitude of attractive forces.

Future Research

The results show an improvement in spraying outcomes with the use of electrostatic spraying within the scope of the original brief. The process of research within the brief has shown research areas which can be further built upon. Areas within plant tissue characterisation, charged spray testing, and particle path reconstruction could benefit from further research, detailed below in order of which sections they are relevant to.

1 Characterization of Plant Tissue Impedance

As noted in Chapter 3, plant impedance shows potential similarity in properties to other living tissues showing some sign of dispersions as present in animal tissue. However, the small sample size of a limited frequency range does not give enough confidence to draw any conclusions. Further research in this area would look further into any similarity with a higher resolution sweep of an extended range of frequencies to characterize the frequency-impedance relationship of plant tissue. Additionally as noted in Chapter 7, it may require investigation into charge retention characteristics in this distributed impedance network and how this would affect spray deposition.

2 Bipolar Charge Spraying

As noted, spray cloud space charge can be a restricting factor in the efficacy of induction charged electrostatic spraying systems. Further research could look into the losses attributable to this and the mitigation of this effect using bipolar charging to limit the net charge imparted onto the spray cloud. An approach similar to Zhao et al. [58] measuring current paths out of the system would provide a strong indication as to any performance benefits.

A high-voltage h-bridge was designed with the intention of testing this, but constructed was not completed. As would be expected, the design is simple, only consisting of the MOFET's and the required circuitry to drive them. The required switching frequency was expected to be below 10Hz, handled externally by a microcontroller. The board has three isolated 12V power supplies in the form of A23 batteries. One for each of the high sides and one for the low side to keep isolation from the low voltage circuitry. Each of these 12V supplies provide power for opto-isolators and MOSFET drivers for their respective part of the circuit. The artwork for this board is shown below in Figure 57.

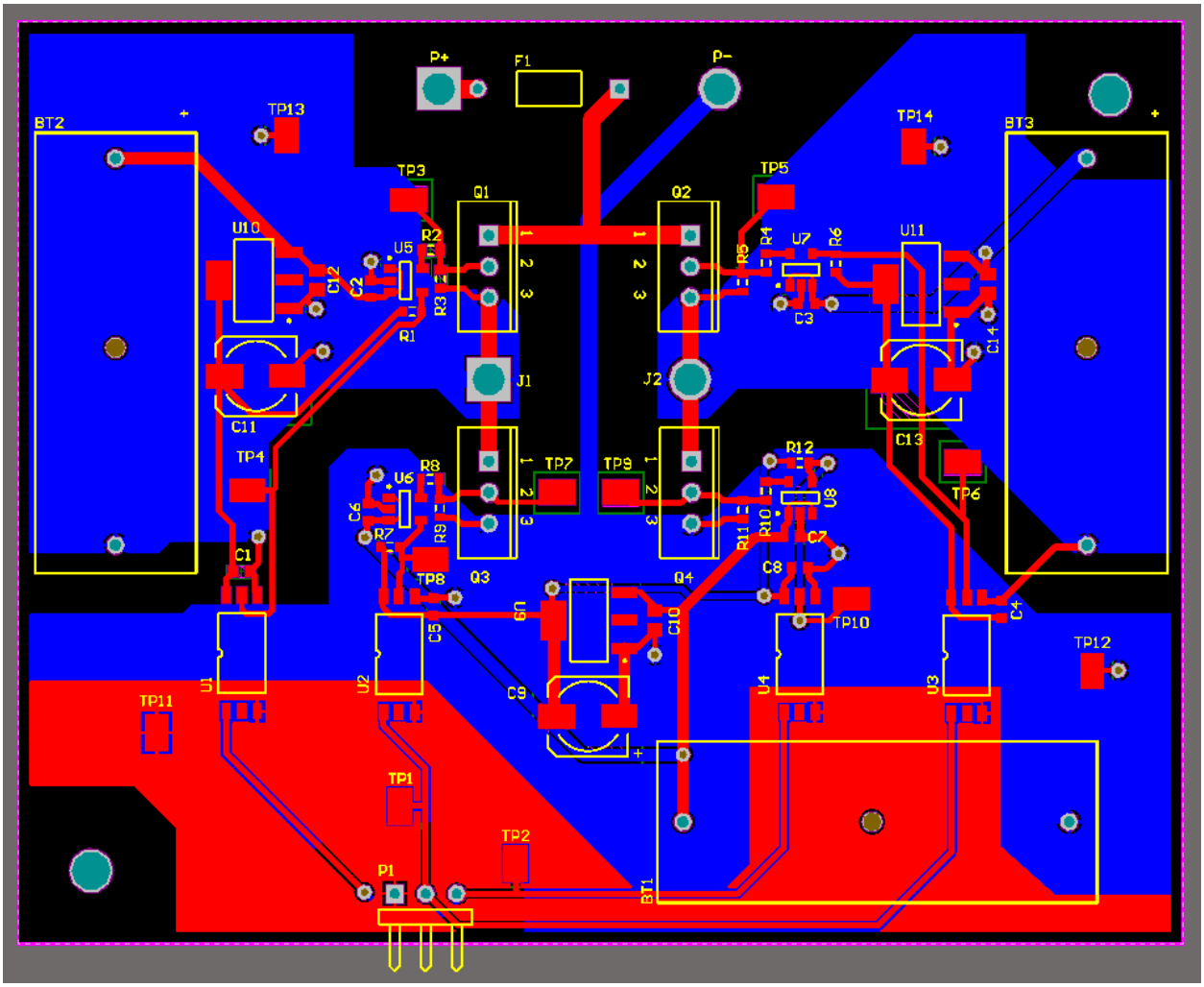

Figure 57: PCB artwork for H-Bridge.

Soon after the board was constructed and tested, the higher voltage requirements became known so the board would require modification to accommodate IGBT's to allow for higher voltage switching.

3 Spray direction control with charged deflection plates

Different target plants and spray environments benefit from an application specific spray pattern. Spray pattern is dependent on nozzle geometry, and once designed cannot be changed beyond altering air and liquid flow rates but these introduce other changes to spray characteristics. Using charged sprays introduces the possibility to alter spray paths independently of the nozzle with electrostatic forces. Charged plates would offer such a way to apply an electrical field to the spray to alter the spray cone outside of the nozzle.

This may allow for optimisation for the spray cone for a given target plant and environmental conditions. Testing will be required to verify if this would have any practical benefit when used in conjunction with electrostatically charged sprays in a real world scenario.

4 Depth Reconstruction with Diffraction Kernel Correlation

A shortfall of the path reconstruction process used here is the lack of depth information extracted from the images. As noted in Chapter 5, correlation strength was dependent on depth from the observation plane of the simulated kernel. This may allow for depth reconstruction. Utilizing a greater number of kernels and iterating through to find

the strongest correlation peak for each given particle, allowing depth information to be extracted however with an increased computational expense.

5 Improved motion modeling and statistical analysis

This research has provided a basic method of analyzing particle motion using laser imaging and simple Kalman filtering. An improved motion model with better velocity calculation and acceleration would provide better predictions with less false positives.

As identified in Chapter 7, droplet diameter and charge are not evenly distributed. This also means droplet charge to mass ratio will also be probabilistically distributed. Also identified in Chapter 7, environmental factors such as turbulence are also present, effecting droplet interactions with the target. While testing apparatus can be isolated to some degree, the nature of twin-fluid air-shear spraying will mean aerodynamic effects will always be present, requiring a model to better characterize the interactions in this use case.

Conclusion

Increasing demands for food production and other agricultural products push demands for improved crop yields. Chemical pest management in the form of pesticides is a widely used method of increasing crop yields, over 90% of which is applied as liquid sprays. Poor application efficacy of these pesticides onto the target plant introduce concerns for both the environment and human health for those that come into contact.

Traditional spraying techniques result in up to 70% off target losses, with less than 1% of the active chemical reaching the target pest. These losses are highly configuration dependent needing to be selected for the target plant and environmental conditions. One method to improve spray efficacy, electrostatically charging the liquid spray, has been previously introduced to market. This thesis has investigated factors influencing the liquid spray deposition onto the target, looking into plant impedances and using computer vision to quantify depositions with the ESS electrostatic nozzle. A high voltage power supply has also been developed to allow control of nozzle voltage.

Chapter 3 investigated overall leaf to ground impedances of potted grapevines and potential sources for the found values. It was found that the frequency and impedance relationship appears to follow dispersions found in other living tissues. It was also found that physical junctions in the plant where plant fibres intersect provided the largest impedance contributions with apparent linear regions in between.

Chapter 4 discussed the design and fabrication of a high voltage power supply, which allowed for variable output voltage for use in testing of the ESS electrostatic nozzle, consisting of a boost converter and full-bridge converter.

Chapter 5 shows the design of tests using high speed imaging to capture droplet movements, and interactions with the target. Firsty a long distance microscope was tested, but ultimately proved to be insufficient for imaging droplets with the desired outcomes. The test configuration was then changed to useaa laser diode as the light source, for used in diffractive imaging.

From there, Chapter 6 covers the extraction of droplet paths from the captured images. Using kernels developed with Fresnel diffraction approximations for correlation to detect the centres of the diffractions caused by the droplets passing through the coherent light. A Kalman filter was implemented to estimate positions and the Hungarian method used to assign detections based on the estimate.

Chapter 7 then covers the analysis and results of the droplet path data. Overall, the interactions observed were as expected, showing increased attraction to the target when the spray is charged. Test 1 showed that at normal plant impedances for a single target, charge retention may is no issue. However, floating or larger impedance network as presented in a real plant, charge retention may present issues at longer spray periods. The results from test 2 indicate that while spraying at increasing voltages had the similar average accelerations, the behavior of the spray changed. At higher nozzle voltages, larger accelerations are seen, however occurring less consistently than at the lower nozzle voltages. This could be due to space charge and mutual repulsion effects causing droplets of higher charge-to-mass ratio to be dispersed before reaching the target. This is suggestive of an upper voltage limit before spray deposition efficacy decreases. Test 3 shows that Coulombic forces are greater than gravity forces for charged droplets, and an inverse relationship between nozzle distance from target and magnitude of attractive forces.

The research covered in this project highlighted areas where continuing research can be conducted. Plant tissue impedance could be further characterised to investigate the similarities seen with other living tissues. This would require a broader frequency range with higher resolution between frequency steps. In addition, the impedance network within a living plant could be investigated for possible charge retention issues for a more complex network as would be found in a larger plant.

An h-bridge was constructed to allow for bipolar switching of the voltage supplied to the nozzle, but this was never implemented in this project. Space charge within the spray cloud has been identified as a potential restricting factor

deposition efficiacy, with bipolar charging presenting a potential solution. Measurement of current paths out of the plant would allow for verification of this, with increased current indicating improved deposition.

Also considered but never tested is the application of charged deflection plates to alter the shape of the spray cone independently of the nozzle geometry. This may provide some benefit in deposition when used in conjunction with charged sprays to better optimise the spray cone for a given target plant and spray environment.

The lack of depth perception in the test configuration used is a factor limiting the analysis of droplet interactions. Droplets could be moving in the depth direction without any indication. However as noted in Chapter 5 correlation strength was dependent on the depth of the simulated kernel potentially allowing for depth information reconstuction.

The motion model implemented in this project was simple and improvement on what was implemented here would allow for improved particle tracking with applications in other fields. Statistical analysis considering droplet size distribution, spary cone charge distribution and turbulence characterization would allow for much more complete analysis of the data gathered.

[1] D. R. Bottrell and D. G. Bottrell, *Integrated pest management*. Council on Environmental Quality, 1979.
[2] M. K. Patel, "Technological improvements in electrostatic spraying and its impact to agriculture during the last decade and future research perspectives–A review," *Engineering in agriculture, environment and food*, vol. 9, no. 1, pp. 92-100, 2016.
[3] P. Fourie, M. Du Preez, J. Brink, and G. Schutte, "The effect of runoff on spray deposition and control of Alternaria brown spot of mandarins," *Australasian Plant Pathology*, vol. 38, no. 2, pp. 173-182, 2009.
[4] S. E. Law, "Agricultural electrostatic spray application: a review of significant research and development during the 20th century," *Journal of Electrostatics*, vol. 51, pp. 25-42, 2001.
[5] W. Hoffmann and A. Hewitt, "Comparison of droplet imaging systems for water-sensitive cards," *Aspects of Applied Biology*, vol. 71, pp. 463-466, 2004.
[6] M. Teske, H. Thistle, and G. Ice, "Technical advances in modeling aerially applied sprays," *Transactions of the ASAE*, vol. 46, no. 4, p. 985, 2003.
[7] J. Kabashima, D. Giles, and M. Parrella, "Electrostatic sprayers improve pesticide efficacy in greenhouses," *California Agriculture*, vol. 49, no. 4, pp. 31-35, 1995.
[8] J. C. van de Zande *et al.*, "Spray techniques: how to optimise spray deposition and minimise spray drift," *The Environmentalist*, vol. 28, no. 1, pp. 9-17, 2008.
[9] P. Groenendijk, J. W. van der Kolk, and K. Z. Travis, "Prediction of exposure concentration in surface waters," *Freshwater field tests for hazard assessment of chemicals*, pp. 105-125, 1994.
[10] R. Schulz, "Comparison of spray drift-and runoff-related input of azinphos-methyl and endosulfan from fruit orchards into the Lourens River, South Africa," *Chemosphere*, vol. 45, no. 4-5, pp. 543-551, 2001.
[11] E. Hodgson and P. E. Levi, "Pesticides: an important but underused model for the environmental health sciences," *Environmental Health Perspectives*, vol. 104, no. suppl 1, pp. 97-106, 1996.
[12] V. Drevenkar and S. Fingler, "Z. Frçbe in Chemical Safety International Reference Manual," ed: VCH, Weinheim, 1994.
[13] S. D. Faust and O. M. Aly, "Water pollution by organic pesticides," *Journal-American Water Works Association*, vol. 56, no. 3, pp. 267-279, 1964.
[14] M. G. Cahill, G. Caprioli, M. Stack, S. Vittori, and K. J. James, "Semi-automated liquid chromatography–mass spectrometry (LC–MS/MS) method for basic pesticides in wastewater effluents," *Analytical and bioanalytical chemistry*, vol. 400, no. 2, pp. 587-594, 2011.
[15] M. Köck-Schulmeyer, M. Villagrasa, M. L. de Alda, R. Céspedes-Sánchez, F. Ventura, and D. Barceló, "Occurrence and behavior of pesticides in wastewater treatment plants and their environmental impact," *Science of the total environment*, vol. 458, pp. 466-476, 2013.
[16] J. Jeyaratnam, "Acute pesticide poisoning: a major global health problem," *World health statistics quarterly 1990; 43 (3): 139-144*, 1990.
[17] C. Wesseling, R. McConnell, T. Partanen, and C. Hogstedt, "Agricultural pesticide use in developing countries: health effects and research needs," *International journal of health services*, vol. 27, no. 2, pp. 273-308, 1997.
[18] M. C. Alavanja, J. A. Hoppin, and F. Kamel, "Health effects of chronic pesticide exposure: cancer and neurotoxicity," *Annu. Rev. Public Health*, vol. 25, pp. 155-197, 2004.
[19] S. R. Kirkhorn and M. B. Schenker, "Current health effects of agricultural work: respiratory disease, cancer, reproductive effects, musculoskeletal injuries, and pesticide–related illnesses," *Journal of Agricultural Safety and Health*, vol. 8, no. 2, p. 199, 2002.
[20] S. Reichenberger, M. Bach, A. Skitschak, and H.-G. Frede, "Mitigation strategies to reduce pesticide inputs into ground-and surface water and their effectiveness; A review," *Science of the Total Environment*, vol. 384, no. 1-3, pp. 1-35, 2007.
[21] S. E. Law and M. D. Lane, "Electrostatic deposition of pesticide spray onto foliar targets of varying morphology," *Transactions of the ASAE*, vol. 24, no. 6, pp. 1441-1445, 1981.
[22] M. F. Waxman, *The agrochemical and pesticides safety handbook*. CRC Press, 1998.
[23] D. Singhanwal, "Concept of Rotary Atomization," R. a. concept.gif, Ed., ed. Wikipedia, 2019.
[24] "Spray Expert, "Plain orifice spray nozzle," P. o. nozzle.png, Ed., ed. Wikipedia, 2011.
[25] "Spray Expert, "Internal mix two-fluid spray nozzle," I. wiki.png, Ed., ed. Wikipedia, 2011.

[26] D. Smith, S. Askew, W. Morris, D. Shaw, and M. Boyette, "Droplet size and leaf morphology effects on pesticide spray deposition," *Transactions of the ASAE,* vol. 43, no. 2, p. 255, 1997.
[27] B. Cooke, E. Hislop, P. Herrington, N. Western, and F. Humpherson-Jones, "Air-assisted spraying of arable crops, in relation to deposition, drift and pesticide performance," *Crop Protection,* vol. 9, no. 4, pp. 303-311, 1990.
[28] E. Hislop, N. Western, B. Cooke, and R. Butler, "Experimental air-assisted spraying of young cereal plants under controlled conditions," *Crop Protection,* vol. 12, no. 3, pp. 193-200, 1993.
[29] M. Piché, B. Panneton, and R. Thériault, "Field evaluation of air-assisted boom spraying on broccoli and potato," *Transactions of the ASAE,* vol. 43, no. 4, p. 793, 2000.
[30] W. Taylor and P. Andersen, "Enhancing conventional hydraulic nozzle use with the Twin Spray System," *BCPC Monograph (United Kingdom),* 1991.
[31] R. Derksen and D. Breth, "Orchard air-carrier sprayer application accuracy and spray coverage evaluations," *Applied Engineering in Agriculture,* vol. 10, no. 4, pp. 463-470, 1994.
[32] F. Hall, "Influence of canopy geometry in spray deposition and IPM," *HortScience,* vol. 26, no. 8, pp. 1012-1017, 1991.
[33] F. Juste, S. Sanchez, R. Iban? ez, L. Val, and C. Garcia, "Measurement of spray deposition and efficiency of pesticide application in citrus orchards," *Journal of Agricultural Engineering Research,* vol. 46, no. 5211, pp. 187-196, 1990.
[34] M. Knoche, N. K. Lownds, and M. J. Bukovac, "Spray application factors and plant growth regulator performance: IV. Dose response relationships," *Journal of the American Society for Horticultural Science,* vol. 125, no. 2, pp. 195-199, 2000.
[35] J. Whitney and M. Salyani, "Deposition characteristics of two air-carrier sprayers in citrus trees," *Transactions of the ASAE,* vol. 34, no. 1, pp. 47-0050, 1991.
[36] P. Steiner, "Factors affecting the efficient use of orchard airblast sprayers," *Trans. Ill. Hort. Soc,* vol. 110, pp. 57-64, 1977.
[37] H. Zhu, D. Reichard, R. Fox, R. Brazee, and H. Ozkan, "Simulation of drift of discrete sizes of water droplets from field sprayers," *Transactions of the ASAE,* vol. 37, no. 5, pp. 1401-1407, 1994.
[38] G. Carman, "Evaluation of citrus sprayer units with air towers [Insecticide application]," *Citrograph,* 1977.
[39] R. Derksen and R. Gray, "Deposition and air speed patterns of air-carrier apple orchard sprayers," *Transactions of the ASAE,* vol. 38, no. 1, pp. 5-11, 1995.
[40] C.-A. d. Coulomb, "Premier Mémoire sur l'Electricité et le Magnétisme," *Histoire de l'Académie Royale des Sciences,* pp. 569-577, 1785.
[41] G. P. Castle and I. I. Inculet, "Space charge effects in orchard spraying," *IEEE transactions on industry applications,* no. 3, pp. 476-480, 1983.
[42] G. A. Matthews, "Pesticide application methods," 4th ed. no. Book, Whole). Hoboken, NJ: John Wiley & Sons, 2013, ch. Electrostatically Charged Sprays.
[43] J. Carlton, L. Bouse, and I. Kirk, "Electrostatic charging of aerial spray over cotton," *Transactions of the ASAE,* vol. 38, no. 6, pp. 1641-1645, 1995.
[44] V. R. Mamidi, C. Ghanshyam, P. M. Kumar, and P. Kapur, "Electrostatic hand pressure knapsack spray system with enhanced performance for small scale farms," *Journal of Electrostatics,* vol. 71, no. 4, pp. 785-790, 2013.
[45] S. Zhao, G. Castle, and K. Adamiak, "Factors affecting deposition in electrostatic pesticide spraying," *Journal of Electrostatics,* vol. 66, no. 11-12, pp. 594-601, 2008.
[46] L. Rayleigh, "XX. On the equilibrium of liquid conducting masses charged with electricity," *The London, Edinburgh, and Dublin Philosophical Magazine and Journal of Science,* vol. 14, no. 87, pp. 184-186, 1882.
[47] A. Gomez and K. Tang, "Charge and fission of droplets in electrostatic sprays," *Physics of Fluids,* vol. 6, no. 1, pp. 404-414, 1994, doi: 10.1063/1.868037.
[48] S. L. Post and R. L. Roten, "A Review of the Effects of Droplet Size and Flow Rate on the Chargeability of Spray Droplets in Electrostatic Agricultural Sprays," *Transactions of the ASABE,* vol. 61, no. 4, pp. 1243-1248, 2018.
[49] E. M. Purcell and D. J. Morin, *Electricity and Magnetism*. Cambridge University Press, 2013.

[50] H. E. Hadley, *Magnetism & Electricity for Beginners*. Macmillan & Company, 1899.
[51] S. E. Law, J. R. Cooke, and S. C. Cooper, "Space charge suppression of electrostatic-induction spray charging," *Journal of electrostatics*, vol. 40, pp. 603-608, 1997.
[52] S. E. Law, "Embedded-electrode electrostatic-induction spray-charging nozzle: theoretical and engineering design," *Transactions of the ASAE*, vol. 21, no. 6, pp. 1096-1104, 1978.
[53] R. Coffee, "Electrodynamic energy-a new approach to pesticide application," in *Proceedings 1979 British Crop Protection Conference-Pests and Diseases.*, 1980, no. Volume 3, pp. 777-789.
[54] J. Marchant and R. Green, "An electrostatic charging system for hydraulic spray nozzles," *Journal of Agricultural Engineering Research*, vol. 27, no. 4, pp. 309-319, 1982.
[55] M. J. Hurley *et al.*, *SFPE handbook of fire protection engineering, fifth edition*. 2016, p. 683.
[56] A. Arnold and B. Pye, "Spray application with charged rotary atomisers," *Monograph, British Crop Protection Council*, pp. 109-117, 1980.
[57] J. F. Hughes, *Electrostatic Particle Charging-Industrial & Health Care Applications: Ist*. Research Studies Press, 1997.
[58] S. Zhao, G. Castle, and K. Adamiak, "The effect of space charge on the performance of an electrostatic induction charging spray nozzle," *Journal of Electrostatics*, vol. 63, no. 3-4, pp. 261-272, 2005.
[59] S. C. Cooper and S. E. Law, "Bipolar spray charging for leaf-tip corona reduction by space-charge control," *IEEE transactions on industry applications*, no. 2, pp. 217-223, 1987.
[60] G. Matthews, "Changes in application techniques used by the small scale cotton farmer in Africa," *International Journal of Pest Management*, vol. 36, no. 2, pp. 166-172, 1990.
[61] R. Smith, "Electrodyn' sprayer: matching the technology to contrasting areas of smallholder agriculture," *Chemistry and Industry*, pp. 196-9, 1988.
[62] Martignani. "MARTIGNANI ELECTROSTATIC SPRAY DEVICE,." https://www.martignani.com/en/martignani-electrostatic-spray-device (accessed 12 Oct., 2020).
[63] Spectrum Electrostatic Sprayers. "Spectrum the Electrostatic Sprayer." http://www.spectrumsprayer.com/ (accessed 12 Oct., 2020).
[64] Electrostatic Spraying Systems. "ESS - Electrostatic Sparying Systems." https://maxcharge.com/ (accessed 12 Oct., 2020).
[65] On Target Spray Systems. "On Target Spray Systems." (accessed 12 Oct., 2020).
[66] S. E. Law and S. C. Cooper, "Electrostatic-induction spray-charging nozzle system," ed: Google Patents, 1998.
[67] S. C. Cooper and S. E. Law, "Electrostatic spray nozzles for abrasive and conductive liquids in harsh environments," ed: Google Patents, 1998.
[68] E. Rogers, "Understanding boost power stages in switchmode power supplies," *TI Literature No. SLVA061*, 1999.
[69] B. J. Saharia and B. K. Talukdar, "Theoretical study on performance constraints of a DC-DC buck-boost converter," 2015 2015, no. Conference Proceedings: IEEE, pp. 1-4, doi: 10.1109/EPETSG.2015.7510119.
[70] P. Villard, "Transformateur à haut voltage. A survolteur cathodique," *Journal de Physique Théorique et Appliquée*, vol. 10, no. 1, pp. 28-32, 1901.
[71] P. Horowitz, "The art of electronics," Third ed. no. Book, Whole). New York, NY: Cambridge University Press, 2015, p. 37.
[72] H. Greinacher, "Das Ionometer und seine Verwendung zur Messung von Radium- und Röntgenstrahlen [The ionometer and its application to the measurement of radium- and Rontgen rays]," *Physikalische Zeitschrift (in German)*, pp. 410-415, 1914:15 1914:15.
[73] E. Gates, *Introduction to electronics*. Cengage Learning, 2011.
[74] M. K. Patel, H. K. Sahoo, M. K. Nayak, A. Kumar, C. Ghanshyam, and A. Kumar, "Electrostatic nozzle: new trends in agricultural pesticides spraying," *SSRG International Journal of Electrical and Electronics Engineering*, pp. 6-11, 2015.
[75] P. A. Franken and R. H. Sands, "The LASER, Light Amplification by Stimulated Emission of Radiation," presented at the The Ann Arbor Conference on Optical Pumping, University of Michigan, 15 June to 18 June, 1959.

[76] L. A. Coldren, S. W. Corzine, and M. L. Mashanovitch, *Diode Lasers and Photonic Integrated Circuits*. Wiley, 2012.
[77] R. N. Hall, G. E. Fenner, J. Kingsley, T. Soltys, and R. Carlson, "Coherent light emission from GaAs junctions," *Physical Review Letters*, vol. 9, no. 9, p. 366, 1962.
[78] B. Oliver, "Sparkling spots and random diffraction," *Proceedings of the IEEE*, vol. 51, no. 1, pp. 220-221, 1963.
[79] G. B. Airy, "On the Diffraction of an Object-glass with Circular Aperture," *Transactions of the Cambridge Philosophical Society*, vol. 5, pp. 283-291, 1835.
[80] "Understanding Spatial Filters." Edmund Optics. https://www.edmundoptics.com/knowledge-center/application-notes/lasers/understanding-spatial-filters/ (accessed 07/10, 2020).
[81] A. De Witte, "Interference in scattered light," *American Journal of Physics*, vol. 35, no. 4, pp. 301-313, 1967.
[82] W.-K. Chen, "The electrical engineering handbook," 1 ed. no. Book, Whole). Amsterdam;Boston;: Elsevier Academic Press, 2005, ch. 4 - Digital Image Processing.
[83] OpenCV. "OpenCV - About." OpenCV. https://opencv.org/about/ (accessed 08/04, 2020).
[84] M. Piccardi, "Background subtraction techniques: a review," in *2004 IEEE International Conference on Systems, Man and Cybernetics (IEEE Cat. No. 04CH37583)*, 2004, vol. 4, no. Conference Proceedings: IEEE, pp. 3099-3104 vol.4, doi: 10.1109/ICSMC.2004.1400815.
[85] J. Carlo and J. Hall, "Spatial filtering using 3 x 3 kernel convolutions," in *Smart Sensors*, 1979, vol. 178: International Society for Optics and Photonics, pp. 154-161.
[86] M. K. Gardner *et al.*, "Model convolution: a computational approach to digital image interpretation," *Cellular and molecular bioengineering*, vol. 3, no. 2, pp. 163-170, 2010.
[87] L. S. Athanasiou, D. I. Fotiadis, and L. K. Michalis, "5 - Plaque Characterization Methods Using Optical Coherence Tomography," in *Atherosclerotic Plaque Characterization Methods Based on Coronary Imaging*, L. S. Athanasiou, D. I. Fotiadis, and L. K. Michalis Eds. Oxford: Academic Press, 2017, pp. 95-113.
[88] R. K. Pearson and M. Gabbouj, *Nonlinear digital filtering with Python: an introduction*. CRC Press, 2018.
[89] OpenCV Team. "OpenCV: Image Filtering." PpenCV. https://docs.opencv.org/master/d4/d86/group__imgproc__filter.html#gac05a120c1ae92a6060dd0db190a61afa (accessed 25 Oct, 2020).
[90] E. S. Gedraite and M. Hadad, "Investigation on the effect of a Gaussian Blur in image filtering and segmentation," in *Proceedings ELMAR-2011*, 2011: IEEE, pp. 393-396.
[91] T. Lindeberg, "Detecting salient blob-like image structures and their scales with a scale-space primal sketch: A method for focus-of-attention," *International Journal of Computer Vision*, vol. 11, no. 3, pp. 283-318, 1993, doi: 10.1007/BF01469346.
[92] C. Damerval and S. Meignen, "Blob Detection With Wavelet Maxima Lines," *IEEE Signal Processing Letters*, vol. 14, no. 1, pp. 39-42, 2007, doi: 10.1109/LSP.2006.879830.
[93] S. Hinz, "Fast and subpixel precise blob detection and attribution," 2005 2005, vol. 3, no. Conference Proceedings: IEEE, pp. III-457, doi: 10.1109/ICIP.2005.1530427.
[94] A. Rosenfeld and C.-Y. Sher, "Detecting image primitives using feature pyramids," *Information Sciences*, vol. 107, no. 1, pp. 127-147, 1998, doi: 10.1016/S0020-0255(97)10021-4.
[95] C.-P. Yu, G. Ruppert, R. Collins, D. Nguyen, A. Falcao, and Y. Liu, "3D blob based brain tumor detection and segmentation in MR images," in *2014 IEEE 11th International Symposium on Biomedical Imaging (ISBI)*, 2014: IEEE, pp. 1192-1197.
[96] A. Hocking, Y. Sun, J. E. Geach, and N. Davey, "Mining hubble space telescope images," in *2017 International Joint Conference on Neural Networks (IJCNN)*, 2017: IEEE, pp. 4179-4186.
[97] H. Kong, H. Cinar Akakin, and S. Sarma, "A Generalized Laplacian of Gaussian Filter for Blob Detection and Its Applications," *Cybernetics, IEEE Transactions on*, vol. 43, pp. 1719-1733, 01/09 2013, doi: 10.1109/TSMCB.2012.2228639.
[98] R. C. Gonzalez, R. E. Woods, and S. L. Eddins, *Digital Image processing using MATLAB* (no. Book, Whole). Upper Saddle River, NJ: Pearson/Prentice Hall, 2004.

[99] L. Vincent and P. Soille, "Watersheds in digital spaces: an efficient algorithm based on immersion simulations," *IEEE Transactions on Pattern Analysis and Machine Intelligence,* vol. 13, no. 6, pp. 583-598, 1991, doi: 10.1109/34.87344.
[100] S. Suzuki, "Topological structural analysis of digitized binary images by border following," *Computer vision, graphics, and image processing,* vol. 30, no. 1, pp. 32-46, 1985.
[101] R. E. Kalman, "A New Approach to Linear Filtering and Prediction Problems," *Journal of Basic Engineering,* vol. 82, no. 1, pp. 35-45, 1960, doi: 10.1115/1.3662552.
[102] G. Bishop and G. Welch, "An introduction to the kalman filter," *Proc of SIGGRAPH, Course,* vol. 8, no. 27599-23175, p. 41, 2001.
[103] P. S. Maybeck, *Stochastic models, estimation and control* (no. Book, Whole). New York: Academic Press, 1979.
[104] J. Diard, P. Bessiere, and E. Mazer, *A Survey of Probabilistic Models Using the Bayesian Programming Methodology as a Unifying Framework*. 2003.
[105] J. Munkres, "Algorithms for the assignment and transportation problems," *Journal of the society for industrial and applied mathematics,* vol. 5, no. 1, pp. 32-38, 1957.
[106] H. W. Kuhn, "The Hungarian method for the assignment problem," *Naval Research Logistics (NRL),* vol. 52, no. 1, pp. 7-21, 2005.
[107] G. Medina-Acosta and J. Delgado-Penín, "On the feasibility of a channel-dependent scheduling for the SC-FDMA in 3GPP-LTE (mobile environment) based on a prioritized-bifacet Hungarian method," *EURASIP Journal on Wireless Communications and Networking,* vol. 2011, 12/01 2011, doi: 10.1186/1687-1499-2011-71.
[108] A. Frank, "On Kuhn's Hungarian method—a tribute from Hungary," *Naval Research Logistics (NRL),* vol. 52, no. 1, pp. 2-5, 2005.
[109] N. Nursultanov, C. Altaner, and W. Heffernan, "Effect of temperature on electrical conductivity of green sapwood of Pinus radiata (radiata pine)," *Wood Science and Technology,* vol. 51, no. 4, pp. 795-809, 2017.
[110] W. Simpson and A. TenWolde, "Physical properties and moisture relations of wood," 1999.
[111] S. Sharma, S. Shukla, and B. Kamala, "Studies on DC electrical resistivity of plantation grown timbers," *Holz als Roh-und Werkstoff,* vol. 55, no. 6, pp. 391-394, 1997.
[112] M. D. Lane and S. E. Law, "Transient charge transfer in living plants undergoing electrostatic spraying," *Transactions of the ASAE,* vol. 25, no. 5, pp. 1148-1153, 1982.
[113] H. P. Schwan, "Electrical properties of tissue and cell suspensions," in *Advances in biological and medical physics*, vol. 5: Elsevier, 1957, pp. 147-209.
[114] S. Grimnes and Ø. G. Martinsen, "Alpha-dispersion in human tissue," in *Journal of Physics: Conference Series*, 2010, vol. 224, no. 1, pp. 1-4.
[115] D. Dean, T. Ramanathan, D. Machado, and R. Sundararajan, "Electrical impedance spectroscopy study of biological tissues," *Journal of electrostatics,* vol. 66, no. 3-4, pp. 165-177, 2008.
[116] S. M. Adl *et al.*, "The revised classification of eukaryotes," *Journal of eukaryotic microbiology,* vol. 59, no. 5, pp. 429-514, 2012.
[117] R. A. Hamman, S. D. Savage, and H. J. Larsen, "Colorado grape growers' guide, The," *Bulletin (Colorado State University. Cooperative Extension Service); 550A*, 1998.
[118] Invitrogen, "00-3002 Phosphate Buffer Saline," in *00-3002*, ed.
[119] S. Thelandersson and H. J. Larsen, *Timber engineering*. John Wiley & Sons, 2003.
[120] EPCOS AG, "Ferrites and accessories - SIFERRIT material N87," ed, 2017.
[121] EPCOS AG, "Ferrites and accessories - RM 8, RM 8 LPCore and accessories," ed, 2017.
[122] K. H. Billings and T. Morey, *Switchmode power supply handbook*. McGraw-Hill, 2011.
[123] EPCOS AG, "Ferrites and accessories - RM 12, RM 12 LP Core and accessories

", ed, 2017.
[124] EPCOS AG, "Ferrites and accessories - SIFERRIT material N41," ed, 2017.
[125] R. A. Serway and C. Vuille, *College Physics*. Cengage Learning, 2014.

[126] C. Laurent and C. Mayoux, "Partial discharge. XI. Limitations to PD as a diagnostic for deterioration and remaining life," *IEEE Electrical Insulation Magazine*, vol. 8, no. 2, pp. 14-17, 1992.
[127] D. CORNING, ""SYLGARD® 170 Silicone Elastomer"," in *Sylgard 170 Datasheet*, ed.
[128] F. Peek, "The law of corona and the dielectric strength of air," *Proceedings of the American Institute of Electrical Engineers*, vol. 30, no. 7, pp. 1485-1561, 1911.
[129] Photron, *FASTCAM SA5, FASTCAM SA5 RV Hardware Manual Revision 2.05E*, 2.05E ed. PHOTRON LIMITED, 2014, p. 111.
[130] Infinity-USA. *Model K2 DistaMax™Long-Distance Microscope System*. (2017). www.infinity-usa.com: Infinity Photo-Optical Company.
[131] H. Bargman, "Laser classification systems," (in eng), *J Clin Aesthet Dermatol*, vol. 3, no. 10, pp. 19-20, 2010. [Online]. Available: https://pubmed.ncbi.nlm.nih.gov/20967190

https://www.ncbi.nlm.nih.gov/pmc/articles/PMC2958191/.
[132] C. R. R. Nave. "Circular Aperture Diffraction." Georgia State University. http://hyperphysics.phy-astr.gsu.edu/hbase/phyopt/cirapp2.html (accessed 16-06, 2020).
[133] K. R. Williams and R. S. Muller, "Etch rates for micromachining processing," *Journal of Microelectromechanical systems*, vol. 5, no. 4, pp. 256-269, 1996.
[134] OpenCV. "Motion Analysis and Object Tracking." OpenCV. https://docs.opencv.org/3.4/d7/df3/group__imgproc__motion.html (accessed 2020).
[135] D. Voelz, "Computational fourier optics: a MATLAB tutorial," 2011: Society of Photo-Optical Instrumentation Engineers.
[136] R. Myose, M. Papadakis, and I. Heron, "Gurney flap experiments on airfoils, wings, and reflection plane model," *Journal of Aircraft*, vol. 35, no. 2, pp. 206-211, 1998.

Appendices

Appendix 1 - Boost Converter Schematic and PCB Artwork

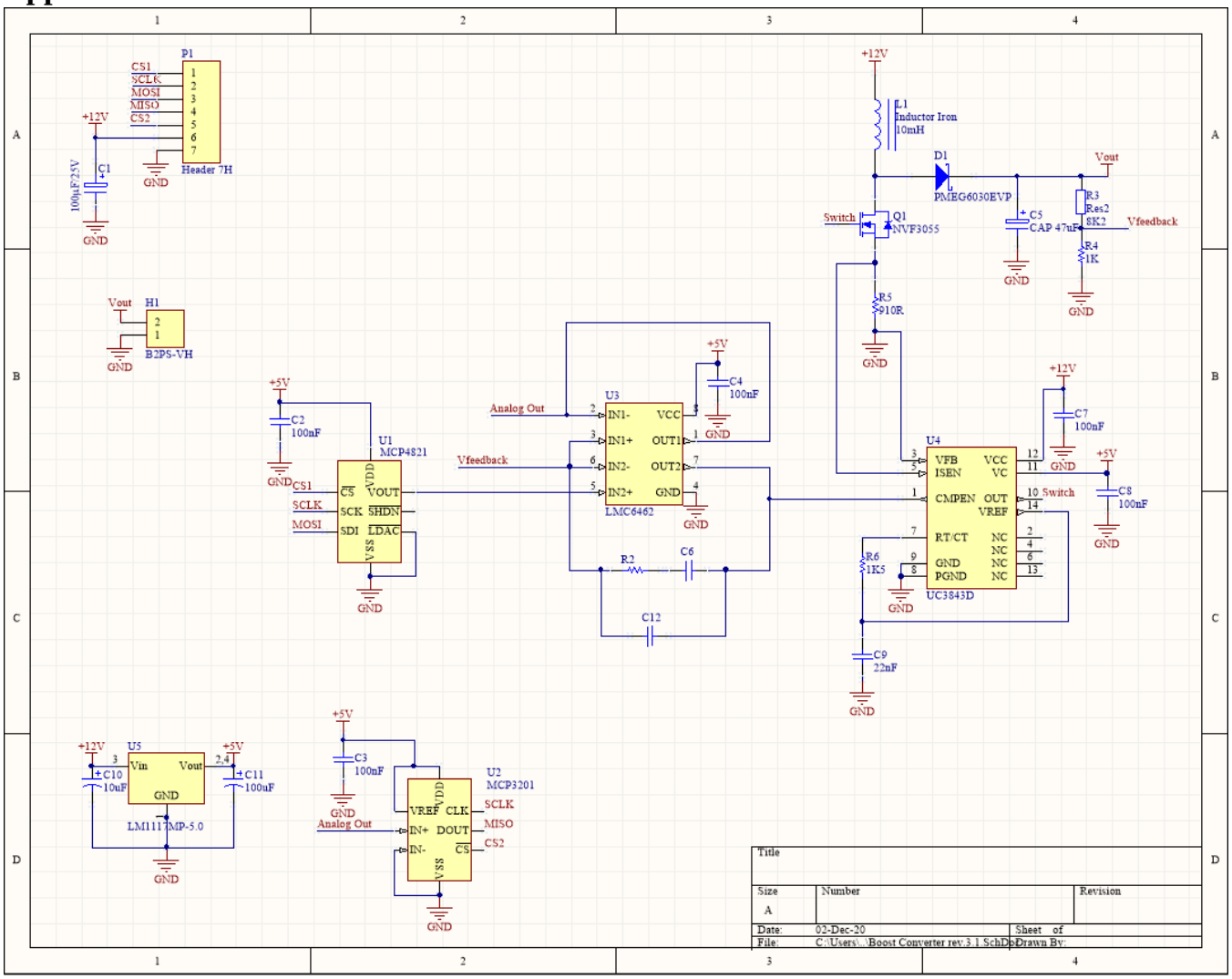

Figure 1: Schematic of boost converter.

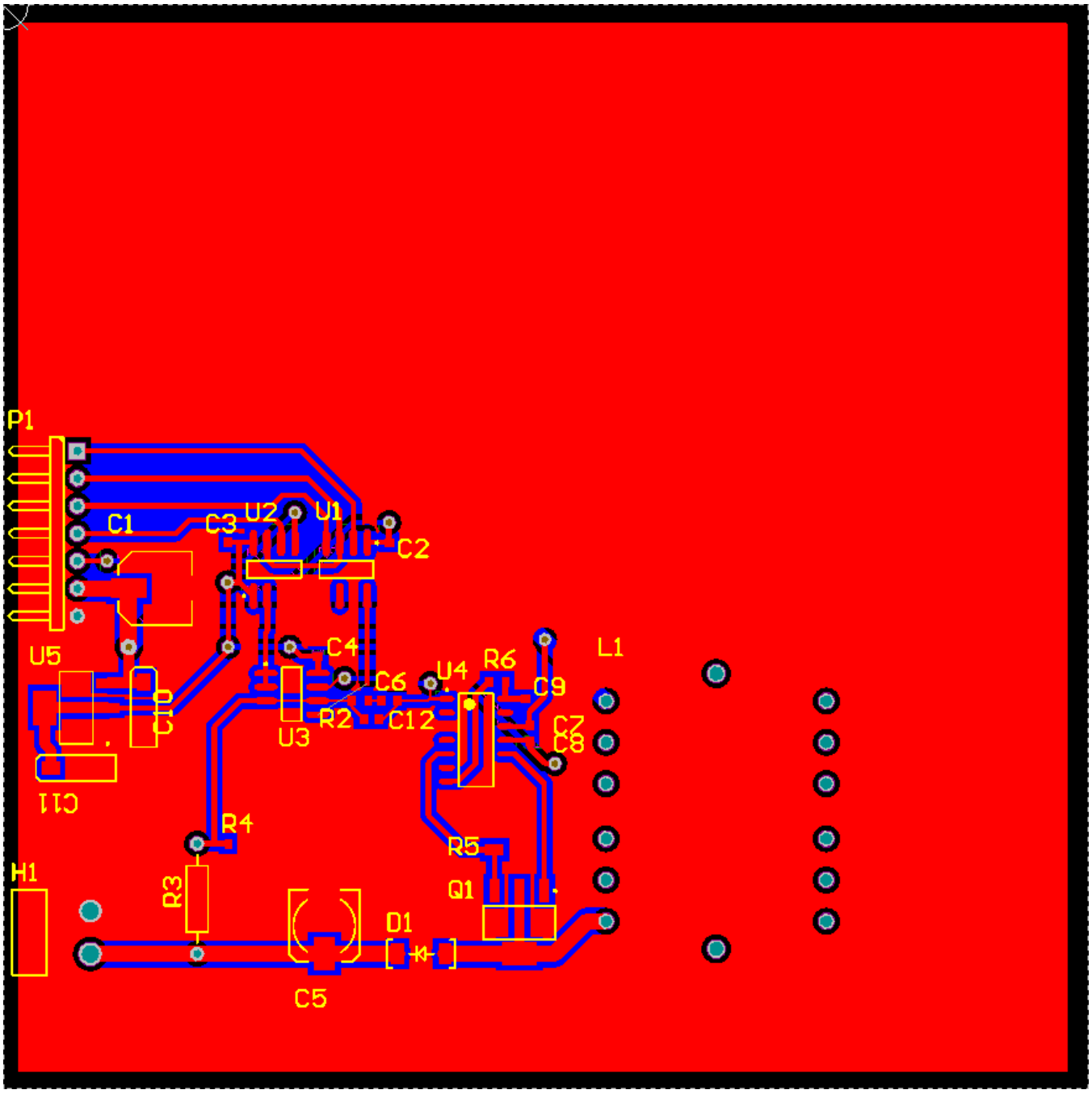

Figure 2: Boost converter PCB artwork showing top layer.

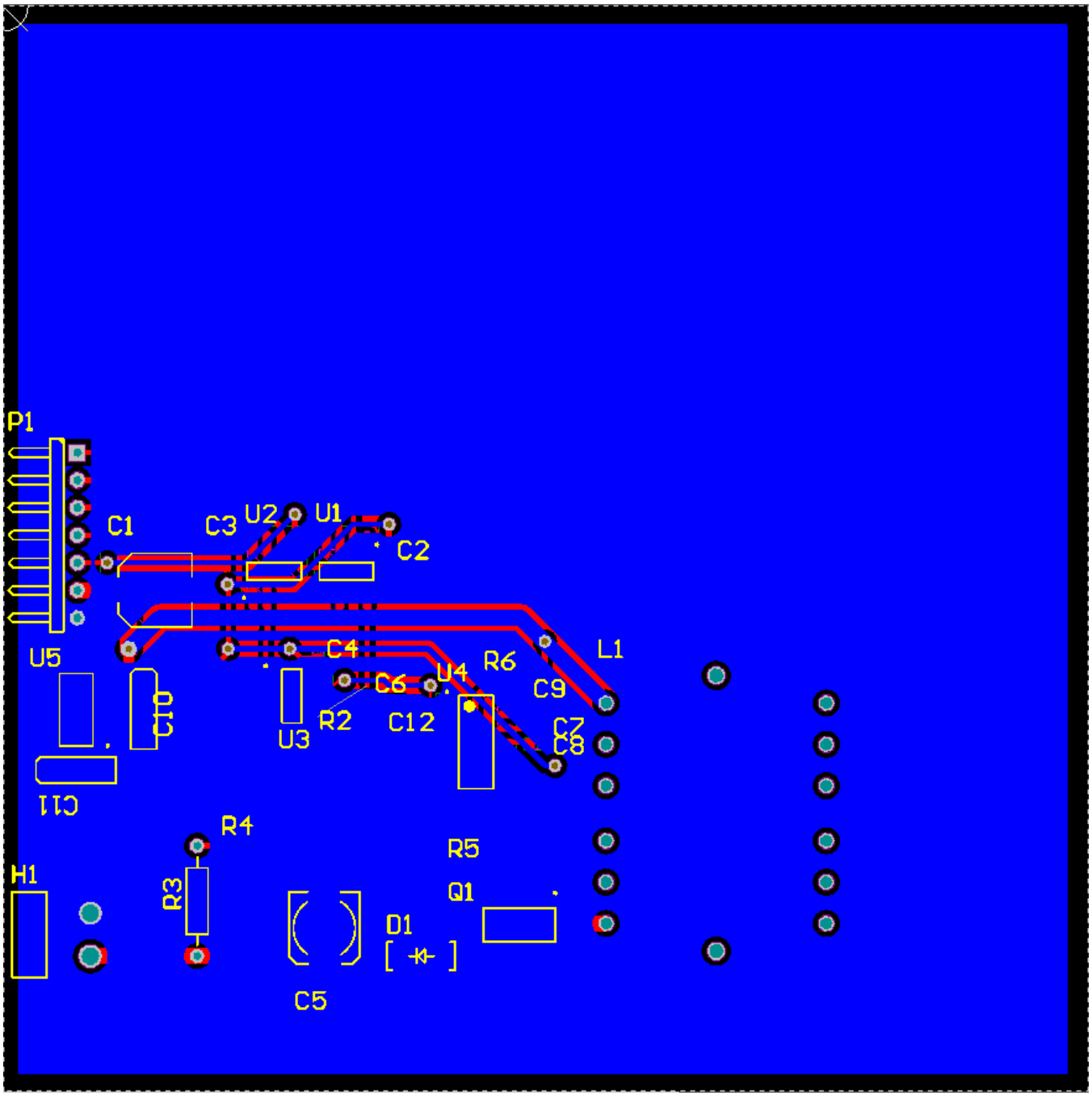

Figure 3: Full-bridge converter PCB artwork showing bottom layer

Appendix 2 – Full-Bridge Converter Schematic and PCB Artwork

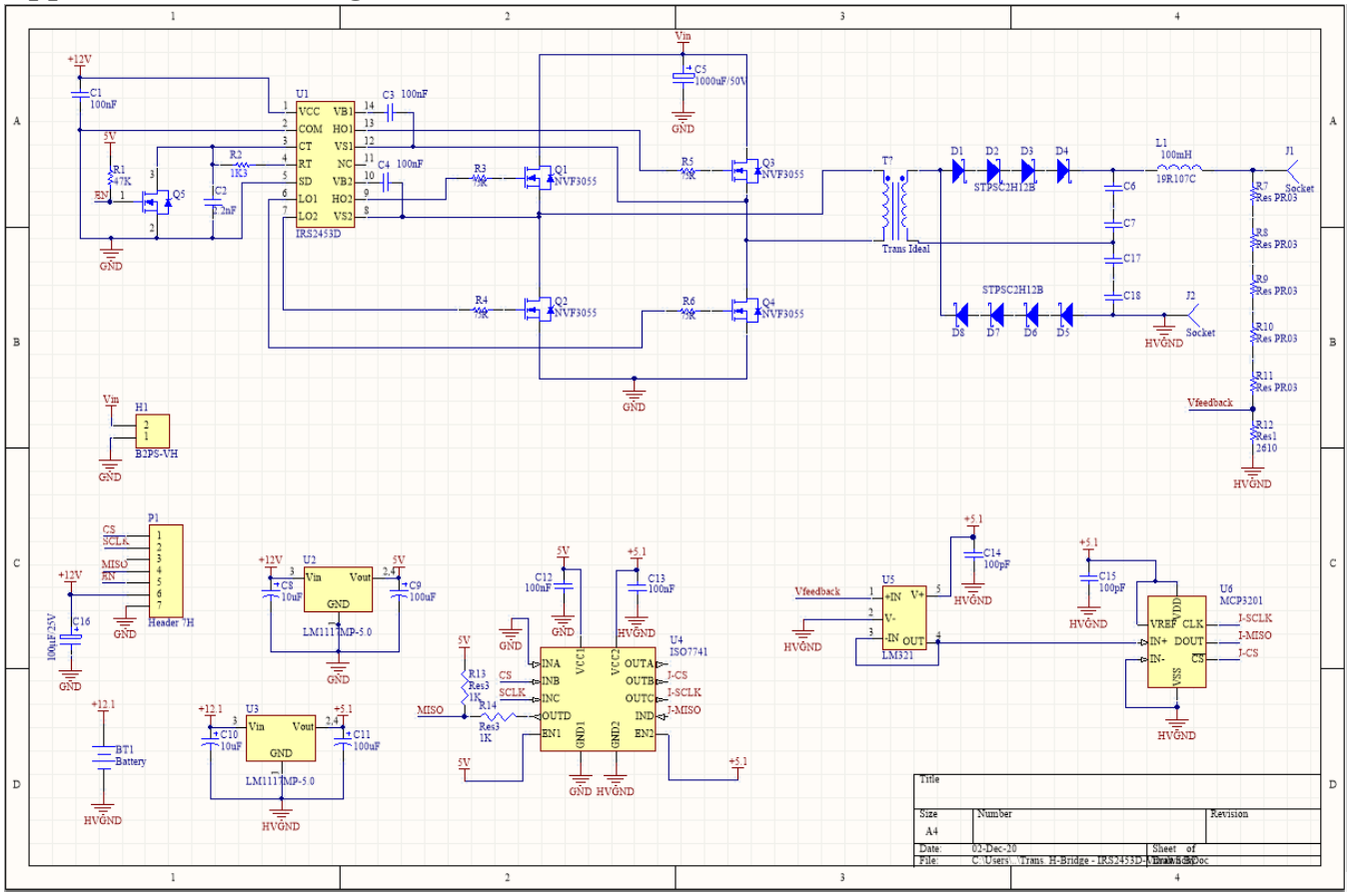

Figure 1: Schematic of full-bridge converter.

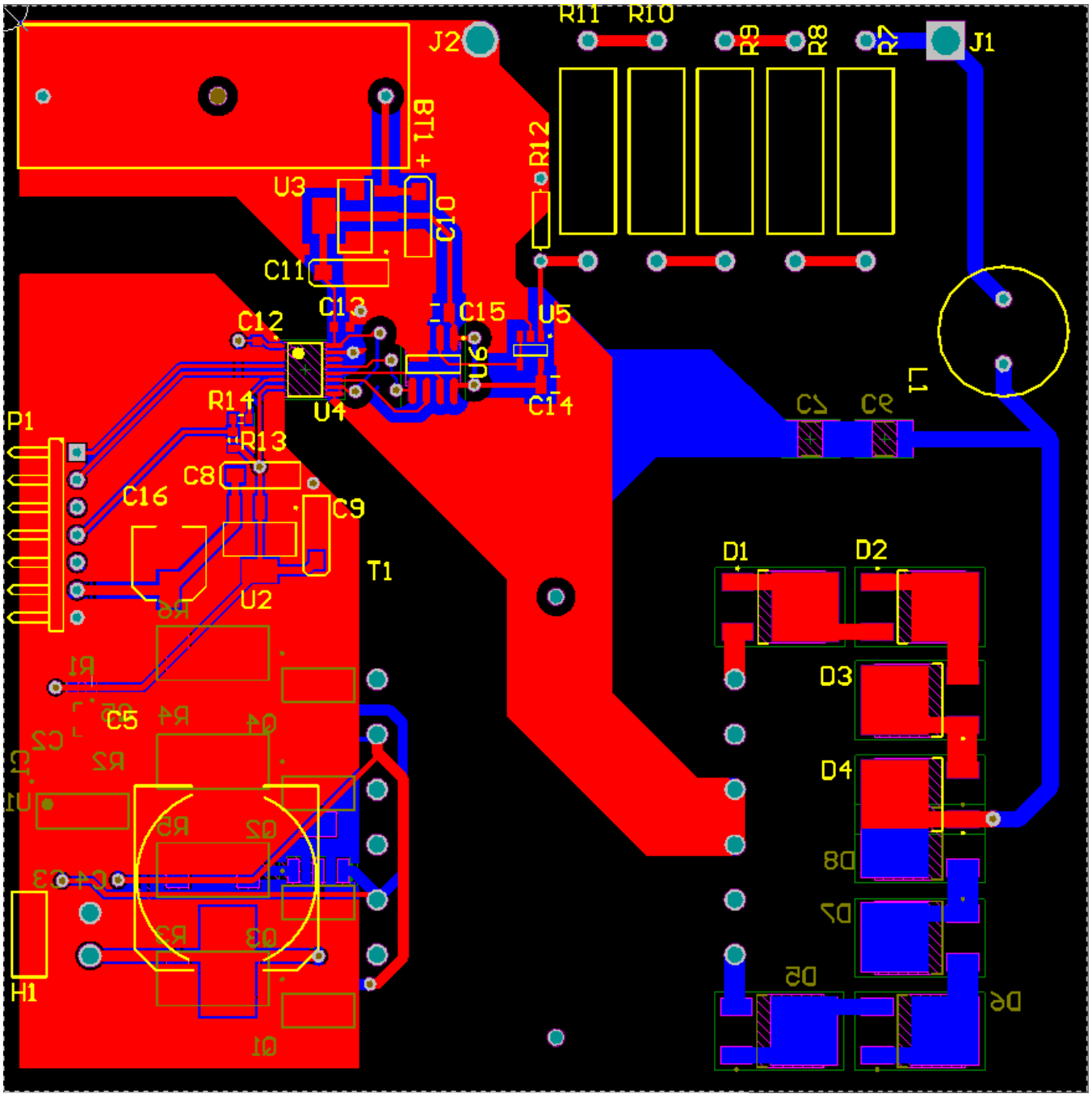

Figure 2: Full-bridge converter PCB artwork showing top layer.

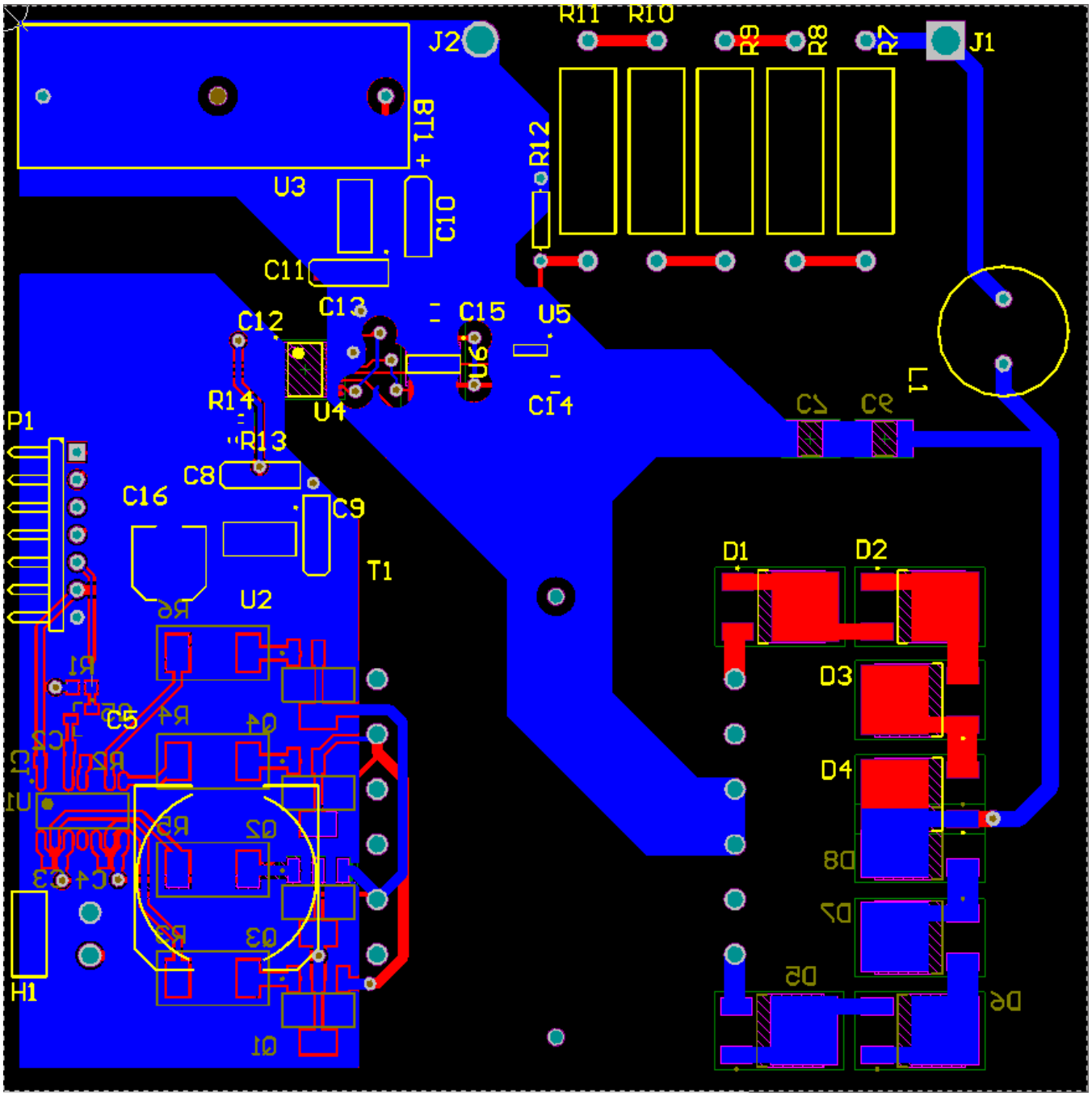

Figure 3: Full-bridge converter PCB artwork showing bottom layer.

Appendix 3

Introduction

This proposal outlines the tests planned using the Photron SA5 High-speed camera and Infinity Model K2 lens. The proposed tests have changed slightly from initial discussion as the tests are made to be more specific. There are now four tests to be conducted investigating; the effect of impedance on charge retention, the wrap around effect distance/voltage relationship, the variation of the wrap around effect within the spray cone, and the effectiveness of charged deflection plates. The tests are outlined through this report listing the testing methods and the deliverables to come from each test. The timeframe for each of the tests is also listed. The dates for the tests will be solidified on approval of this proposal as the actual timeline will depend on access to equipment and lab space as some is shared though the testing should be completed within 3 weeks including injury time to deal with any issues with test set up.

Camera and lens usage and storage

When in use the camera will be stored in its current location of the aerodynamics lab. The camera can alternatively be stored in a technician's office by arrangement with the people who may be using it. The lens will be stored in a locker secured with a padlock in room 104 unless another storage location is preferred.

During testing, the camera and lens will be mounted together on the aluminium baseplate. This assembly will be placed on the desk adjacent to the test rig. Access to the camera will not be possible while the rig is in its position for testing. This set up will eliminate the requirement for tripods and ensure the camera and lens are in a stable location. Height adjustments will be made by moving the testing rig up and down on its stand.

The testing rig is located in the back corner of room 106. This will be the permanent location of the rig for the duration of my testing. The positioning of the rig is shown in Figure 1.

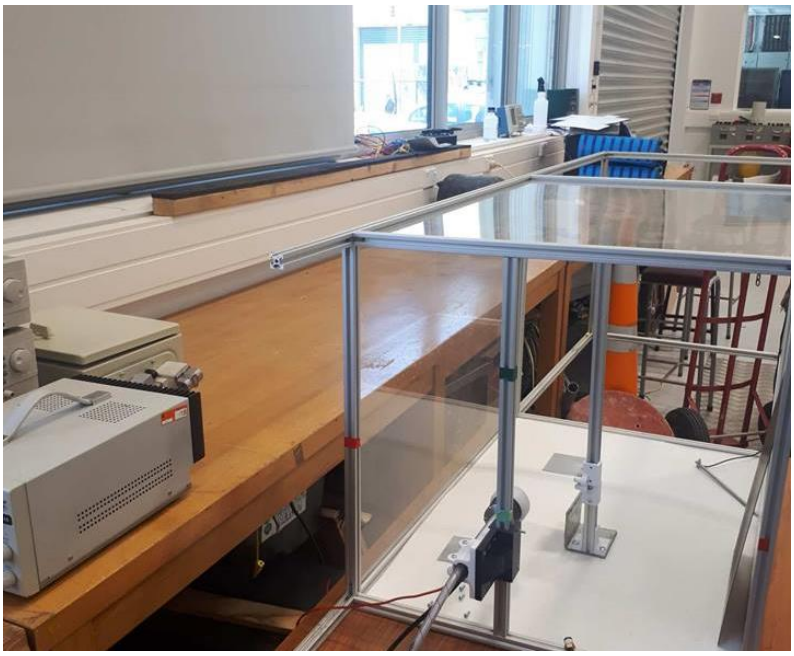

Figure 1: LOCATION OF THE TESTING RIG IN ROOM 106.

Test 1 – Effect of impedance on charge retention

The goal of this test is to measure if charge retention will occur/have an effect on the interaction between droplets and the target for a spray period of less than one second. The extreme cases will be tested first, low impedance earthed and open circuit. If there is an observable difference in droplet-target interaction, impedances within the range found on a potted grapevine (up to 2.5MΩ) will be tested in stepped values after high-speed footage can be analysed.

Test Conditions

Tap water will be sprayed at a plate fixed at 600mm from the nozzle in the centre of the spray cone for a period of one second.

The air pressure will be fixed at 70 psi.

The droplets will be illuminated with a high brightness spot light source parallel with the camera.

Nozzle voltage will be fixed at 4000V.

First the target will be earthed in a low impedance configuration. This is to be repeated five times.

The target will then be sprayed with the target isolated. This is again to be repeated five times.

The target will then be sprayed with the in a high impedance 1 MΩ earth. This is again to be repeated five times.

How it will be observed

The camera will be positioned to focus on the edge of the plate. The angular change in droplet trajectory as it interacts with the target and the distance from the plate at which these deflections occur being the goal of the high-speed imaging.

Deliverables

To measure if there is a change in spray droplet deposition between the open and closed circuit cases. If there is an observable difference in droplet-target interaction, find at which time period this occurs. In later testing measure the effect at different impedance values. This test will provide insight in whether bipolar voltage switching will be useful with plant spraying.

This testing will be completed over one day.

Test 2 – Wrap around effect distance/voltage relationship

The goal of this test is to measure the relationship between the magnitude of droplet-target interaction and the nozzle voltage.

Test Conditions

Tap water will be sprayed at a plate fixed at 600mm from the nozzle in the centre of the spray cone for a period of one second.

The air pressure will be fixed at 70 psi.

The droplets will be illuminated with a high brightness spot light source parallel with the camera.

The nozzle voltage will be stepped between 2000V and 4000V in 500V increments.

Each voltage step will be repeated three times resulting in fifteen individual tests.

How it will be observed

The camera will be positioned to focus on the edge of the plate. The angular change in droplet trajectory as it interacts with the target and the distance from the plate at which these deflections occur being the goal of the high-speed imaging.

Deliverables

To quantify the relationship between a magnitude of the droplet-target interaction and the voltage at the nozzle. This will indicate if deposition is improved on a single target with increased nozzle voltage.

This testing will be completed over one day.

Test 3 – Variation of the wrap around effect within the spray cone

The goal of this test is to investigate if there is variation of the wrap around effect within the spray cone due to variation of charge distribution within the spray cone and to measure if effect decays at increased distances from the nozzle.

Test Conditions

Tap water will be sprayed at a plate fixed at a number of positions relative to the nozzle. The spray period will be one second.

The air pressure will be fixed at 70 psi.

The droplets will be illuminated with a high brightness spot light source parallel with the camera.

The nozzle voltage will be fixed at 4000V

The plate will be moved to the following positions within the spray cone:

- Perpendicular to nozzle,
- 600-1200mm horizontal distances from nozzle in 200mm steps.
- Vertically within the spray cone. Centre and top/bottom edges of the spray cone at ± 10 degrees with the plate perpendicular to the nozzle.

Each iteration will be done three times resulting in 36 individual tests.

How it will be observed

The camera will be positioned to focus on the edge of the plate. The angular change in droplet trajectory as it interacts with the target and the distance from the plate at which these deflections occur being the goal of the high-speed imaging.

Deliverables

The relationship between the magnitude of droplet-target interaction and the position of the target within the spray cone.

This testing will be completed over a one to two day period.

Appendix 4

Introduction

This proposal outlines the tests planned using the Photron SA5 High-speed camera and a collimated laser beam. There are three tests to be conducted investigating the effect of impedance on charge retention, the wrap around effect distance/voltage relationship, and the variation of the wrap around effect within the spray cone. The tests are outlined through this report listing the testing methods and the deliverables to come from each test. The timeframe for each of the tests is also listed. The dates for the tests will be solidified on approval of this proposal as the actual timeline will depend on access to equipment and lab space as some is shared though the testing should be completed within one and a half weeks including injury time to deal with any issues with test set up.

Collimated Laser Module Configuration

The collimated laser module consists of a 5mw laser diode (Hitachi HL6312G) with the beam output into a 50mm microscope objective. This is focussed through a 10µm pinhole to remove any aberrations. This beam is then passed through a 100mm biconvex lens to collimate the beam. The 100mm biconvex lens has a 25mm diameter giving a collimated beam diameter of 25mm. The laser diode is driven by a Thorlabs LD1100 constant power driver. This is illustrated in Figure 1.

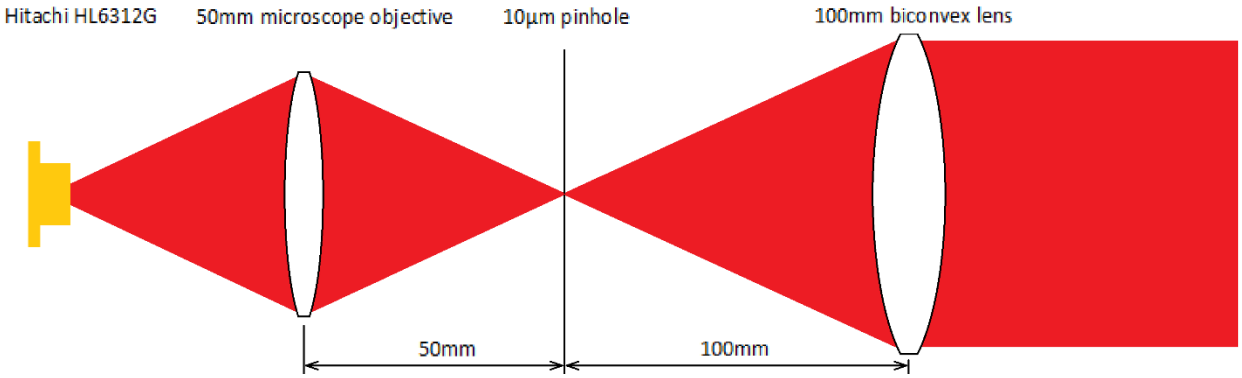

Figure 1: Representative model of collimated laser module. (Note: not to scale).

This collimated laser module will be situated to point directly at the sensor of a Photron SA5 high-speed camera. The beam will pass through a 30mm inner diameter tube of PVC between the output of the laser module and camera sensor with a break of approximately 100mm where the target being observed will be placed. This is to keep the beam as encapsulated as possible during testing and reduce the risk of damage as much as possible. The layout of the test is shown in Figure 2.

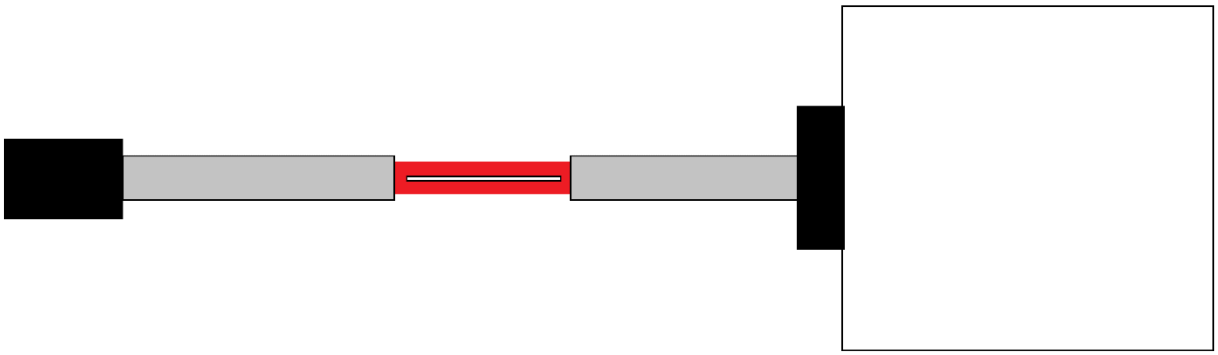

Figure 2: Illustration of imaging apparatus. Laser module on left, PVC piping in grey, beam in red with target, Photron SA5 on right.

Test 1 – Effect of impedance on charge retention

The goal of this test is to measure if charge retention will occur/have an effect on the interaction between droplets and the target for a spray period of less than one second. The extreme cases will be tested first, low impedance earthed and open circuit. If there is an observable difference in droplet-target interaction, impedances within the range found on a potted grapevine (up to 2.5MΩ) will be tested in stepped values after high-speed footage can be analysed.

Test Conditions

Tap water will be sprayed at a plate fixed at 600mm from the nozzle in the centre of the spray cone for a period of one second.

The air pressure will be fixed at 70 psi.

The droplets will be superimposed onto the camera sensor with the collimated laser module.

Nozzle voltage will be fixed at 4000V.

First the target will be earthed in a low impedance configuration. This is to be repeated five times.

The target will then be sprayed with the target isolated. This is again to be repeated five times.

The target will then be sprayed with the in a high impedance 1 MΩ earth. This is again to be repeated five times.

How it will be observed

The beam path will centre on the edge of the target plate. The angular change in droplet trajectory as it interacts with the target and if and how this changes between earthed and unearthed targets will be observed and recorded.

Deliverables

To measure if there is a change in spray droplet deposition between the open and closed circuit cases. If there is an observable difference in droplet-target interaction, find at which time period this occurs. In later testing measure the effect at different impedance values. This test will provide insight in whether bipolar voltage switching will be useful with plant spraying.

This testing will be completed over one day.

Test 2 – Wrap around effect distance/voltage relationship

The goal of this test is to measure the relationship between the magnitude of droplet-target interaction and the nozzle voltage.

Test Conditions

Tap water will be sprayed at a plate fixed at 600mm from the nozzle in the centre of the spray cone for a period of one second.

The air pressure will be fixed at 70 psi.

The droplets will be superimposed onto the camera sensor with the collimated laser module.

The nozzle voltage will be stepped between 2000V and 4000V in 500V increments.

Each voltage step will be repeated three times resulting in fifteen individual tests.

How it will be observed

The beam path will centre on the edge of the target plate. The angular change in droplet trajectory as it interacts with the target and the distance from the plate at which these deflections occur being the goal of the high-speed imaging.

Deliverables

To quantify the relationship between a magnitude of the droplet-target interaction and the voltage at the nozzle. This will indicate if deposition is improved on a single target with increased nozzle voltage.

This testing will be completed over one day.

Test 3 – Variation of the wrap around effect within the spray cone

The goal of this test is to investigate if there is variation of the wrap around effect within the spray cone due to variation of charge distribution within the spray cone and to measure if effect decays at increased distances from the nozzle.

Test Conditions

Tap water will be sprayed at a plate fixed at a number of positions relative to the nozzle. The spray period will be one second.

The air pressure will be fixed at 80 psi.

The droplets will be superimposed onto the camera sensor with collimated laser module.

The nozzle voltage will be fixed at 4000V

The plate will be moved to the following positions within the spray cone:

- Perpendicular to nozzle,
- 600-1200mm horizontal distances from nozzle in 200mm steps.
- Vertically within the spray cone. Centre and top/bottom edges of the spray cone at ± 10 degrees with the plate perpendicular to the nozzle.

Each iteration will be done three times resulting in 36 individual tests.

How it will be observed

The beam path will centre on the edge of the target plate. The angular change in droplet trajectory as it interacts with the target and the distance from the plate at which these deflections occur being the goal of the high-speed imaging.

Deliverables

The relationship between the magnitude of droplet-target interaction and the position of the target within the spray cone.

This testing will be completed over a one to two day period.